UNIVERSITÉ DU QUÉBEC

THÈSE PRÉSENTÉE À

L'UNIVERSITÉ DU QUÉBEC À TROIS-RIVIÈRES

COMME EXIGENCE PARTIELLE

DU DOCTORAT EN SCIENCES DE L'ÉNERGIE ET DES MATÉRIAUX

PAR

PENG LYU

EFFECT OF MECHANICAL DEFORMATION ON HYDROGEN STORAGE PROPERTIES OF TIFE-BASED ALLOYS

JUILLET 2018

UNIVERSITÉ DU QUÉBEC À TROIS-RIVIÈRES

Cette thèse a été dirigée par :

Jacques Huot, Ph.D.	Université du Québec à Trois-Rivières
Directeur de recherche, grade	Institution à laquelle se rattache l'évaluateur

Jury d'évaluation de la thèse :

Jacques Huot, Ph.D.	Université du Québec à Trois-Rivières
Prénom et nom, grade	Institution à laquelle se rattache l'évaluateur
Jacques Goyette, Ph.D.	Université du Québec à Trois-Rivières
Prénom et nom, grade	Institution à laquelle se rattache l'évaluateur
Jean Hamelin, Ph.D.	Université du Québec à Trois-Rivières
Prénom et nom, grade	Institution à laquelle se rattache l'évaluateur
Jinsheng Xiao, Ph.D.	Wuhan University of Technology, China
Prénom et nom, grade	Institution à laquelle se rattache l'évaluateur
Fusheng Yang, Ph.D.	Xi'an Jiaotong University,China
Prénom et nom, grade	Institution à laquelle se rattache l'évaluateur

Thèse soutenue le 12 juillet 2018

RÉSUMÉ

Cette thèse présente les propriétés de microstructure et de stockage d'hydrogène de l'alliage TiFe dopé avec des éléments de transition et/ou traité par déformation mécanique. Dans un premier temps, l'effet de différents additifs (Zr, Zr+2Mn, Zr+2V) sur les propriétés de microstructure et d'hydrogénation de l'alliage TiFe a été étudié. Pour l'additif Zr, trois compositions très similaires ont été investiguées: $Ti_{0.95}FeZr_{0.05}$, $TiFe_{0.95}Zr_{0.05}$, et $TiFeZr_{0.05}$. On peut constater que tous ces alliages sont constitués d'une phase de TiFe avec une petite quantité de zirconium et d'une phase secondaire riche en zirconium. En même temps, on peut voir que la substitution partielle du zirconium par le fer, le titane ou les deux améliore la première cinétique d'hydrogénation du TiFe. La première hydrogénation de l'alliage $Ti_{0.95}FeZr_{0.05}$ se déroule plus rapidement que pour les deux autres alliages. Ceci est probablement dû à une distribution plus fine de la phase secondaire. Les isothermes pression/composition des alliages $TiFeZr_{0.05}$ et $Ti_{0.95}FeZr_{0.05}$ sont similaires alors que l'alliage $TiFe_{0.95}Zr_{0.05}$ présente la plus grande capacité. Ces résultats démontrent qu'une très légère variation de composition a un effet important sur la microstructure et les comportements de stockage de l'hydrogène.

Pour l'additif (Zr+2Mn), chaque alliage était constitué de deux phases: une phase de TiFe avec une très faible quantité de zirconium et de manganèse, et une seconde phase avec une proportion plus élevée de zirconium et de manganèse. On peut constater que la première cinétique d'hydrogénation augmente avec la quantité de (Zr+2Mn). Ceci est probablement dû à la présence de la phase secondaire riche en zirconium qui agit comme une passerelle pour que l'hydrogène pénètre dans la phase principale de TiFe. Les isothermes pression/composition montrent également que l'augmentation de la quantité de (Zr+2Mn) diminue la pression du plateau d'absorption. Pour une quantité de (Zr+2Mn) de 12 % en poids, l'exposition à l'air a eu un impact minimal sur le comportement d'absorption de l'hydrogène. De plus, le

laminage à froid a un effet minimal sur la première cinétique d'hydrogénation du TiFe dopé avec un alliage à 4 % en poids (Zr+2Mn). En ce qui concerne l'additif (Zr+2V), chaque alliage était constitué de deux phases: une phase de TiFe avec une très faible quantité de zirconium et de vanadium, et une phase secondaire présentant une proportion plus élevée de zirconium et de vanadium. On a constaté que la première cinétique d'hydrogénation augmente avec la proportion de (Zr+2V). Cependant, la capacité réversible diminue avec la proportion croissante (Zr+2V). Après l'hydrogénation de l'alliage TiFe+12 % en poids (Zr+2V), deux types de phases hydrures coexistent: une structure orthorhombique avec un groupe spatial: Cmmm et une structure monoclinique avec un groupe spatial: P2/m. Après la déshydrogénation, la phase d'hydrure avec la phase P2/m et la phase de TiFe étaient présentes.

L'effet de la déformation mécanique (broyage à billes, laminage à froid et forgeage) sur la microstructure et les premières propriétés d'hydrogénation du TiFe dopé avec 4 % en poids de Zr ou 4 % en poids (Zr+2Mn) ont été étudiés. Tout d'abord, le dopage du TiFe avec 4 % en poids de Zr par broyage à boulets a réduit significativement la taille des particules et des cristallites, mais la plus grande partie de la réduction s'est produite pendant les 15 premières minutes de broyage. Le broyage à boulets a amélioré la cinétique initiale par rapport à l'échantillon moulé, mais la capacité a été réduite. La cinétique accrue était due à la réduction de la taille des cristallites avec le temps de broyage. Deuxièmement, le dopage de TiFe avec 4 % en poids de Zr par laminage à froid et forgeage a également réduit la taille des particules et des cristallites. Un échantillon laminé à froid avec un échantillon à 5 passages a montré la cinétique d'hydrogénation initiale la plus rapide mais la capacité totale a été réduite. La capacité maximale a également été réduite par forgeage. Enfin, l'utilisation de laminage à froid et de forgeage pour doper TiFe avec 4 % en poids (Zr+2Mn) a été étudiée. Le laminage à froid a réduit la taille des cristallites mais aucune réduction de la taille des cristallites n'a été mesurée dans le cas du forgeage. Un échantillon laminé à froid avec un échantillon à 1 passage montre la capacité la plus élevée et un échantillon laminé à froid avec un échantillon à 5 passages présente la cinétique

d'hydrogénation initiale la plus rapide. D'autre part, l'échantillon forgé n'a pas absorbé d'hydrogène.

ABSTRACT

This thesis presents the investigation on the microstructure and hydrogen storage properties of TiFe alloy doped with transition elements and/or processed by mechanical deformation. At first, the effect of different additives (Zr, Zr+2Mn, Zr+2V) on the microstructure and hydrogenation properties of TiFe alloy was studied. For the additive Zr, three very closely related compositions were studied: $Ti_{0.95}FeZr_{0.05}$, $TiFe_{0.95}Zr_{0.05}$, and $TiFeZr_{0.05}$. It was found that all these alloys are made of a TiFe phase with small amount of zirconium and a secondary phase which is zirconium rich. Partial substitution of zirconium for iron, titanium or both can improve the first hydrogenation kinetics of TiFe. First hydrogenation of $Ti_{0.95}FeZr_{0.05}$ alloy proceed faster than for the other two alloys. This is probably due to a finer distribution of the bright secondary phase. Pressure-composition isotherms of $TiFeZr_{0.05}$ and $Ti_{0.95}FeZr_{0.05}$ alloys were similar while the alloy $TiFe_{0.95}Zr_{0.05}$ showed the highest capacity. These results demonstrated that a very slight variation of composition could have an important effect of microstructure and hydrogen storage behaviours.

In the case of the additive (Zr+2Mn), each alloy was made of two phases: a TiFe phase with very small amount of zirconium and manganese, and a second phase which had a higher proportion of zirconium and manganese. It was found that the first hydrogenation kinetics increase with the amount of (Zr+2Mn). This is most likely due to the presence of zirconium-rich secondary phase that acts as a gateway for hydrogen to enter the main TiFe phase. Pressure-composition isotherms also showed that increasing the amount of (Zr+2Mn) decreased the absorption plateau pressure. Moreover, for the amount of (Zr+2Mn) of 12 wt.%, air exposure had a minimal impact on hydrogen absorption behaviour. In addition cold rolling has minimal effect on the first hydrogenation kinetics of TiFe doped with 4 wt.% (Zr+2Mn) alloy.

For the additive (Zr+2V), each alloy was made of two phases: a TiFe phase with very small amount of zirconium and vanadium, and a secondary phase which has a higher proportion of zirconium and vanadium. The first hydrogenation kinetics increased with the proportion of (Zr+2V) and the mechanism of first hydrogenation kinetics of

three alloys was in accordance with GB3D model. However, the reversible capacity decreased with increasing (Zr+2V) proportion. After the hydrogenation of the TiFe+12 wt.% (Zr+2V) alloy, two kinds of hydride phases were found to coexist: one orthorhombic structure with space group: Cmmm and one monoclinic structure with space group: P2/m. After dehydrogenation the hydride phase with space group P2/m and TiFe phase were present.

The effect of mechanical deformation (ball milling, cold rolling and forging) on the microstructure and first hydrogenation properties of TiFe doped with 4 wt.% Zr or 4 wt.% (Zr+2Mn) alloy was also investigated. First, doping TiFe with 4 wt.% of Zr by ball milling significantly reduced the particle and crystallite sizes but most of the reduction occurred during the first 15 minutes of milling. Ball milling improved the initial kinetics compared with as-cast sample but the capacity was reduced. The increased kinetics was due to the reduction of crystallites size with milling time. Secondly, doping TiFe with 4 wt.% Zr using cold rolling and forging also reduced the particle and crystallite sizes. Cold-rolled sample with 5 passes sample showed the fastest initial hydrogenation kinetics but the total capacity was reduced. The maximum capacity was also lowered by forging. Finally, using cold rolling and forging to dope TiFe with 4 wt.% (Zr+2Mn) was studied. Cold rolling reduced the crystallite size but no crystallite size reduction was measured in the case of forging. Cold-rolled sample with 1 pass shows the highest capacity and cold-rolled sample with 5 passes sample presented the fastest initial hydrogenation kinetics. On the other hand, the forged sample didn't absorb any hydrogen.

FOREWORD

TiFe alloy is a kind of potential hydrogen storage material. But due to very high temperature and hydrogen pressure for its first hydrogenation, TiFe-based hydrogen storage materials are limited for practical applications. Recently researchers found that doping with transition elements and mechanical deformation can be used to improve the first hydrogenation performance of hydrogen storage materials. In that context, my Ph.D. project is to find a combination of alloy composition and mechanical deformation treatment to produce a low-cost TiFe-based alloy for practical applications. Besides, the objective is also to understand the fundamental mechanism of element substitution and mechanical deformation on hydrogen storage properties of TiFe alloy.

ACKNOWLEDGEMENT

At first, I would like to express my deepest gratitude to my Professor Jacques Huot, for his guidance and 100 percent patience. I learnt a lot of precious spirit and attitude for research from him. I also want to express my sincere gratitude to Professor Jinsheng Xiao, for his valuable suggestions and encouragement during my PhD.

I would like to thank Mrs. Can Tao, who helped me a lot when I started my PhD work in UQTR. I would like to thank Dr. Vinay Dixit, for her nice discussion and beautiful smile. I would like to thank Dr. Salma Sleiman, for her delicious food and great zeal. Many thanks to Dr. Abhishek Patel, I will always remember those days that we studied together. I also thank to Dr. Vola Raza for her insightful suggestions and unparalleled enthusiasm. I also thank to Dr. Jingjing Liu for her constructive suggestions and discussion on my thesis. I also thank Dr. Liang Tong, Dr. Marc-Antoine Pagé, Dr. Amol Kamble, Dr. Zhihai Zhang and Professor Feng Ye, who helped me a lot in my life. I wish to thank Mrs. Agnes. Lejeune for SEM analysis, Canadian light source for synchrotron. I am also very thankful to Fonds de recherche du Quebec-Nature et Technologies (FRQNT) for a PBEEE fellowship.

Finally, I want to express my sincere thanks to my parents and wife who had always supported me and encouraged me to finish my PhD.

TABLE OF CONTENTS

LIST OF FIGURES

LIST OF TABLES

SECTION A

The important thing in life is to have a great aim, and the determination to attain it. — Johann Wolfgang von Goethe

1. Introduction

1.1. Context

1.1.1. Hydrogen energy

Because of its high energy density, small environmental impact, light weight and variety of means of production, hydrogen is considered to be a good energy carrier for the renewable energies. First of all, the potential sources of hydrogen are extensive and hydrogen can be directly decomposed from water. Hydrogen can be produced using green energy sources, such as nuclear, solar, hydro and wind energies. Second, the gravimetric energy density of hydrogen is about 3 times of gasoline, 3.9 times of alcohol and 4.5 times of coke. What's more, the product of combustion of hydrogen is pure water. Fig 1.1 shows a chart of hydrogen from the production to application. It is clear that the hydrogen application is also very extensive. It can be easily used for power generation, fuel cell electric vehicles, industrial processes and so on [1-3].

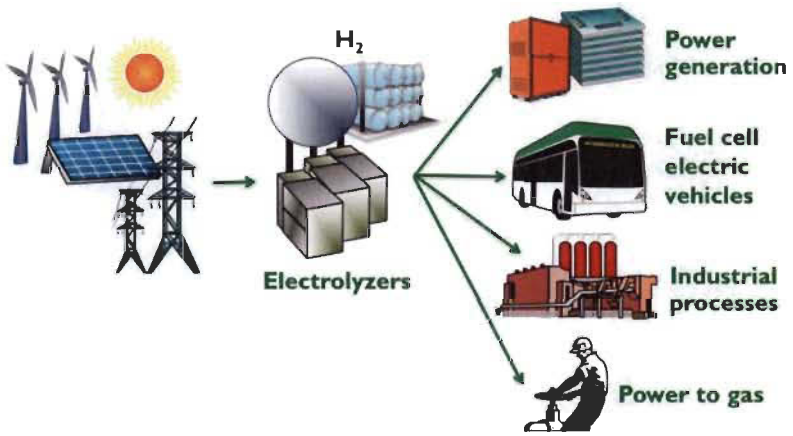

Fig 1.1–Flow chart of hydrogen from production to application [4].

1.1.2. Hydrogen storage

In order to use hydrogen, some important key problems such as hydrogen production, hydrogen purification, hydrogen storage, hydrogen transport and hydrogen utilization need to be solved. Among them, how to store hydrogen safely and efficiently is an important research topic. Presently there are three main ways to store hydrogen: liquid,

solid and compressed gases [5, 6]. The advantages and disadvantages of three different storage means are shown in Table 1.1.

Table 1.1-Three ways for storing the hydrogen [5, 6].

Methods	Advantages	Disadvantages
Liquid	High storage capacity 0.070 kg/L	High energy consumption and low temperature (-252.8 °C)
Compressed gas	Simple and practical 0.030 kg/L	High pressure (350-700 bar) tank and bigger volume and weight of tank
Solid	Safe and high storage capacity	High cost and complex synthesis

Considering operation temperature and pressure, safety and other factors, metal hydrides are considered to be excellent candidates for mobile and stationary hydrogen storage applications. The main advantages of storing hydrogen in a metal hydride are the high hydrogen volumetric densities (usually higher than in liquid hydrogen) and the possibility to absorb and desorb hydrogen over a small range of hydrogen pressure.

Table 1.2 presents the theoretical hydrogen storage capacities and hydriding substances as hydrogen storage media. From this table it can be seen that MgH_2 shows the best gravimetric storage capacity (about 0.07 kg of H_2 / kg of metal). However the hydrogenation kinetics of MgH_2 is too slow and the decomposition temperature is too high (around 330 °C). Therefore searching new hydrogen storage materials and understanding the hydrogenation mechanism are still a scientific challenge.

Table 1.2-Theoretical capacities and hydriding substances as storage media [7].

Medium	Hydrogen content, kg/kg	Hydrogen storage capacity, kg/L of vol.	Energydensity, kJ/kg	Energy density, kJ/L of vol.
MgH_2	0.070	0.101	9,933	14,330
Mg_2NiH_4	0.0316	0.081	4,484	11,494
VH_2	0.0207		3,831	
$FeTiH_{1.95}$	0.0175	0.096	2,483	13,620
$TiFe_{0.7}Mn_{0.2}H_{1.9}$	0.0172	0.090	2,440	12,770
$LaNi_5H_{7.0}$	0.0137	0.089	1,944	12,630
$MmNi_5H_{6.5}$	0.0135	0.090	1,915	12,770
Liquid H_2	1.00	0.071	141,900	10,075
Gaseous H_2(100bar)	1.00	0.0083	141,900	1,170
Gaseous H_2(200bar)	1.00	0.0166	141,900	2,340

1.1.3. Metal hydrides

In metal hydrides, there is a bond between hydrogen and metallic atoms. In these compounds, hydrogen occupies interstitial sites in the unit cell and forms a metallic bond with the metal. Metal hydrides can show some metallic characteristic properties such as high thermal and electrical conductivity, hardness and luster [7].

1.1.3.1. AB_5 intermetallic compounds

For AB_5 intermetallic compounds, many different elemental species can be substituted (at least partially) into the A and B lattice sites. Usually A is a hydride-forming element and B is a non-hydride forming element [7]. $LaNi_5$ is the representative of AB_5 type hydrogen storage alloys as shown in Fig 1.2. This alloy was found in Phillips laboratory in 1969 and has $CaCu_5$ type crystal structure and hexagonal lattice. It is well known that the first hydrogenation of AB_5 type hydrogen storage alloy is fast at room temperature and under low hydrogen pressure with about 1.5 wt.% theoretical hydrogen storage capacity. Presently, this kind of hydrogen storage alloy is mainly used for Ni-MH battery. In order to meet the requirements of different applications, researchers have developed many $LaNi_5$-based hydrogen storage alloys by replacing La or Ni with different elements.

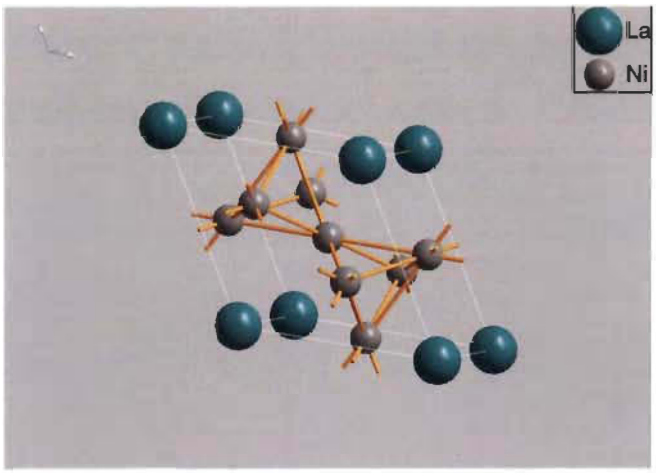

Fig 1.2–Crystal structure of the $LaNi_5$ alloy

1.1.3.2. AB_2 intermetallic compounds

For AB_2 compounds, A-elements can be one or more of titanium, zirconium, hafnium and rare earth elements. Generally the B-elements can be one or more of vanadium, chromium, manganese and iron. This means that there are many different possible substitutions for elements A and B [7]. The common representative AB_2 alloy $TiCr_2$ is shown in Fig 1.3. This kind of hydrogen storage alloy shows good hydrogenation

kinetics. However, they show very poor chemical properties in alkaline solution, so it is not suitable for electrode materials.

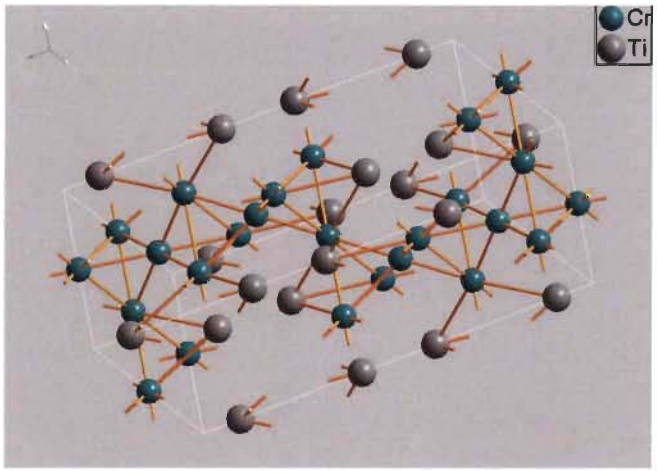

Fig 1.3–Crystal structure of the $TiCr_2$ alloy

1.1.3.3. A_2B intermetallic compounds

For A_2B compounds, element A can be Mg, Hf, Ti and Zr. Element B can be Cu, Ca, La, Al, Ni and so on [7]. The representative A_2B typed alloy is Mg_2Ni as shown in Fig 1.4. In 1968 Reilly et. al found that Mg_2Ni alloy can absorb 3.6 wt.% hydrogen at around 250 °C [8]. It was found that the addition of the 3d elements could improve the hydrogen storage performance of the Mg_2Ni alloy and decrease the temperature and pressure of the first hydrogenation. For example, 3d elements can be used to partly substitute for Ni. Actually different preparation methods (ball milling, melt spinning and spark plasma sintering) could be used to prepare Mg_2Ni alloy. For example, ball milling is a good way to improve the hydrogenation properties of Mg_2Ni alloy due to the formation of amorphous and nanocrystalline microstructures during the milling process [9, 10].

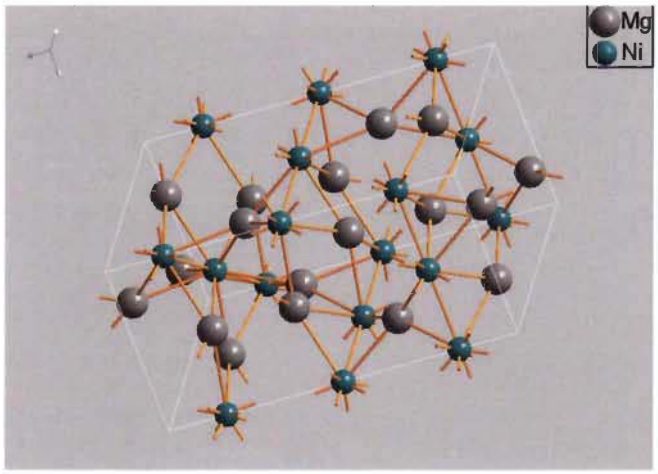

Fig 1.4–Crystal structure of the Mg_2Ni alloy

1.1.3.4. AB intermetallic compounds

Compared to AB_5 and AB_2 compounds, AB intermetallic alloys have good volumetric and gravimetric reversible hydrogen storage capacities. Fig 1.5 shows a typical AB type hydrogen storage alloy TiFe. In 1974 Reilly et. al first reported that TiFe hydrogen storage alloy can absorb hydrogen at room temperature and under low hydrogen pressure [11]. This makes TiFe alloy a potential material for solid state hydrogen storage. However there are two main problems which restrict the practical application of TiFe alloy. One problem is its poor first hydrogenation kinetics which needs high temperature and pressure. In fact Reilly et. al also reported that the first hydrogenation of TiFe alloy could only be achieved through exposure to high temperature (673K) and high pressure (6~7 Mpa) [12]. The other problem is the air sensitivity (such as O_2, CO, H_2O). That is to say exposure to air will seriously affect the hydrogenation rate and reversible capacity of TiFe alloy.

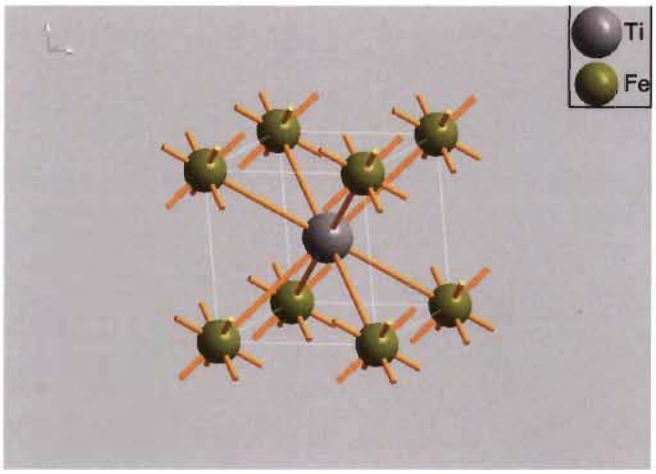

Fig 1.5–Crystal structure of the TiFe alloy

1.1.4. Hydriding process

1.1.4.1. Absorption mechanism

It is generally believed that there are seven steps in the hydrogenation process. The hydrogenation process mainly includes hydrogen molecular migration (step 1), interfacial diffusion (step 2) and physical adsorption (step 3), dissociation of hydrogen molecules (step 4) and chemisorption (step 5), chemical reaction (step 6, Partly hydrogenated and multifarious hydride phase) and hydride formation (step 7, Fully hydrogenated), as shown in Fig 1.6 [13-15].

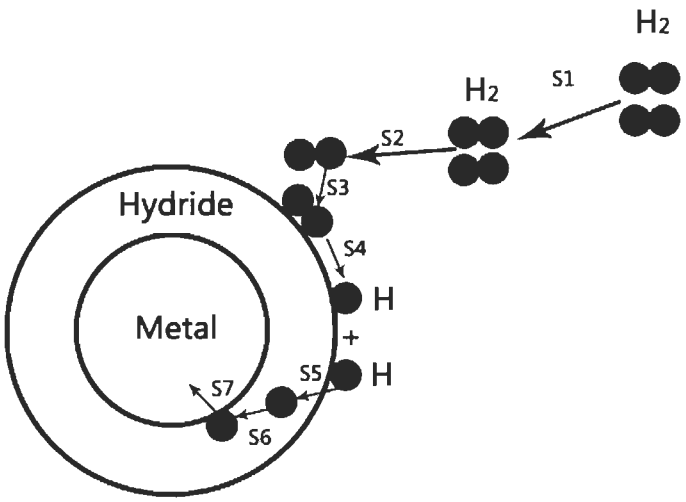

Fig 1.6–Seven steps of the hydrogenation process

The dehydrogenation process is just opposite. Metal hydrides decompose at a certain temperature and ambient pressure. Hydrogen atoms diffuse to the surface of the alloy and recombine into hydrogen molecules.

1.1.4.2. Kinetic models

Usually, the rate limiting steps of hydrogen absorption/desorption are one of those listed in Table 1.3 (Nucleation-growth-impingement model (JMA) [16-18], Contracting volume model (CV) [19-21] and Ginstling-Brounshtein model (GB) [22, 23]). In these equations, α is the reaction fraction ($\alpha=\%H_{abs}/\%H_{max}$), t is reaction time, and k is a constant. In order to find the correct kinetic model, the left side of these equations is plotted as a function of time. For this type of plot, the correct rate limiting step will be a linear curve [24].

Table 1.3-Rate limiting step model equations [24, 25].

Model name	Model equation where α is $\%H_{abs}/\%H_{max}$	Model description
Chemisorption	$\alpha=kt$	Surface controlled
Nucleation-growth-impingement model (JMA2D)	$[-\ln(1-\alpha)]^{1/2}=kt$	2D growth of existing nuclei with constant interface velocity
Nucleation-growth-impingement model (JMA3D)	$[-\ln(1-\alpha)]^{1/3}=kt$	3D growth of existing nuclei with constant interface velocity
Contracting volume model (CV2D)	$1-(1-\alpha)^{1/2}=kt$	2D growth of with constant interface velocity
Contracting volume model (CV3D)	$1-(1-\alpha)^{1/3}=kt$	3D growth of with constant interface velocity
Ginstling-Brounshtein model (GB2D)	$(1-\alpha)\ln(1-\alpha)+\alpha=kt$	2D growth, diffusion controlled with decreasing interface velocity
Ginstling-Brounshtein model (GB3D)	$1-(2\alpha/3)-(1-\alpha)^{2/3}=kt$	3D growth, diffusion controlled with decreasing interface velocity

1.1.4.3. Thermodynamics

In general, the hydrogenation and dehydrogenation process can be expressed by this following equation.

$$\frac{2}{y-x}MHx + H_2 \xleftrightarrow{P,T} \frac{2}{y-x}MHy + Q \quad (1\text{-}1)$$

In this equation, M is the hydrogen storage alloy, MH_x is the metal hydride, Q is the reaction heat, x is the hydrogen equilibrium concentration in the solid solution, y is the hydrogen concentration in the hydride (y>x). A schematic pressure-composition-temperature (PCT) curve is shown in Fig 1.7. From point A to B in PCT curve, hydrogen atoms gradually dissolve into the metal and form hydrogen-metal solid solution (α phase) with increasing the hydrogen pressure. At point B, the hydride phase (β phase) nucleates. From point B to C, α and β phases coexist with increasing proportion of β phase as hydrogen concentration increases. According to Gibbs phase rule F=C-P+2 (F is the number of degrees of freedom, C is the number of components and P is the number of phases in thermodynamic equilibrium with each other), C only includes the metal and hydrogen. P includes α phase, β phase and hydrogen. So F=2-3+2=1. When the composition (C) changes the equilibrium pressure doesn't change. At point C, α phase totally transformed to the β phase and the degree of freedom is 2. After point C, hydrogen atoms dissolve into the metal hydride with increasing hydrogen pressure.

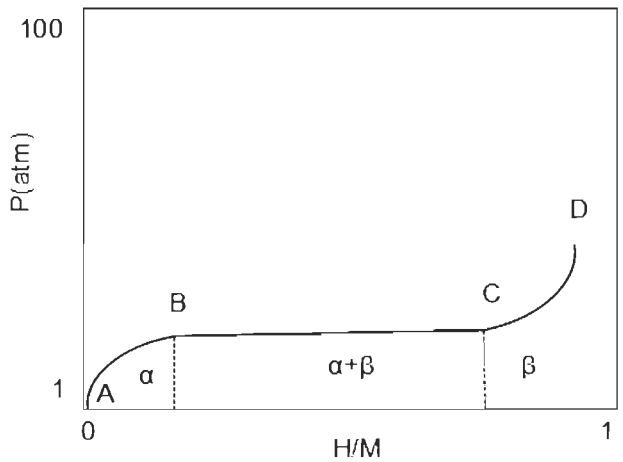

Fig 1.7–Schematic representation of PCT curves of hydrogen-absorbing alloys [26].

The Van't Hoff equation shows the relationship of the equilibrium constant K_{eq}, T, ideal gas constant R and the standard enthalpy change ΔH^{Θ}. A standard Van't Hoff equation can be written as equation (1-2):

$$\frac{d \ln K_{eq}}{dT} = \frac{\Delta H^{\Theta}}{RT^2} \text{ (1-2)}$$

According to the definition of Gibbs free energy, we can obtain equation (1-3 and 1-4). ΔG^{Θ} is the standard Gibbs free energy change, ΔH^{Θ} is the standard enthalpy change, ΔS^{Θ} is the standard entropy change and K_{eq} is the equilibrium constant respectively. T is the thermodynamic temperature, P_{eq} is the equilibrium hydrogen pressure at temperature T, P_0 is the standard atmospheric pressure (1 bar) and R is the gas constant (8.3145 J / (K mol)).

$$\Delta G^{\Theta} = \Delta H^{\Theta} - T\Delta S^{\Theta} \text{ (1-3)}$$

$$\Delta G^{\Theta} = -RT \ln K_{eq} = RT \ln \frac{P_{eq}}{P_0} \text{ (1-4)}$$

Using equation (1-3 and 1-4), we obtain equation (1-5). It can be found that ln (P_{eq} / P_0) and 1 / T are a strictly linear relationship in a certain temperature range.

$$\ln \frac{P_{eq}}{P_0} = \frac{\Delta H^{\Theta}}{RT} - \frac{\Delta S^{\Theta}}{R} \text{ (1-5)}$$

Fig 1.8 shows the relationship between PCT and Van't Hoff curves of a metal hydride. Using equation (1-5), ln (P_{eq} / P_0) and 1 / T relationship diagram can be plotted as shown in Fig 1.8 (b). Then we can calculate ΔH^{Θ} and ΔS^{Θ} using the slope and intercept of the straight line [27, 28].

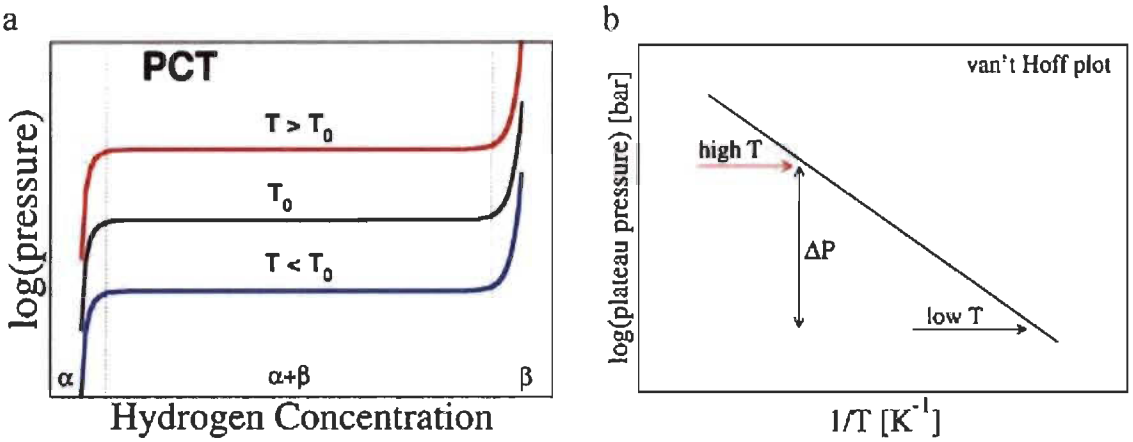

Fig 1.8–(a) Pressure-composition isotherm (PCT) covering the two-phase region of a metal hydride. (b) The Van't Hoff plot corresponding to the equilibrium pressure at different temperatures [29].

1.2. Doping and mechanical deformation of TiFe alloy

TiFe alloy is one of the first metal hydrides that have been considered for hydrogen storage and it is still a promising candidate for solid state hydrogen storage. However, the practical applications are limited due to the slow first hydrogenation process [30-32]. Therefore, there is a real need to find a way to improve the conditions of first hydrogenation of TiFe alloys. Generally, one of the ways to improve the first hydrogenation of TiFe alloy is to add some elements like transition metals and rare-earth metals [30, 33-37]. Another way is by preparing an ultra-fine microstructure. Different methods have been applied to produce such microstructure. They include melt spinning [38], ball milling [39-44], cold rolling [45] and high pressure torsion [46, 47].

In an early investigation, Yang et. al found that adding a small amount of manganese to TiFe alloy can improve the activation kinetics [30]. A few years later, Lee et. al reported that substituting iron by chromium or manganese can lead to a higher first hydrogenation rate, lower plateau pressure and higher maximum absorption capacity [35, 36]. This indicates that chromium and manganese play an important role on changing the first hydrogenation of TiFe alloy. Later, Nishimiya et. al found that zirconium substitution for titanium in TiFe alloy can lower the equilibrium pressure and narrow the width of the plateau at 293 and 313 K [48]. In addition, increasing the

zirconium content can increase the hydrogen capacity. Kumar et. al found that adding 3.1 mass % vanadium into TiFe alloy improves hydrogen absorption kinetics and the hydrogen storage capacity of TiFe is slightly decreased because of lattices expansion and the strong interaction between hydrogen and vanadium [37]. Recently, Jain et al observed that adding 4 wt.% zirconium can shorten the incubation time of the first hydrogenation without changing the reversible storage capacity. Addition of Zr_7Ni_{10} to TiFe also resulted in remarkable improvement in activation behaviour. This result indicates that Zr-based alloy may be good additives for TiFe alloy [49]. All of these studies show that some transition metals have a positive effect on the hydrogen storage properties of TiFe alloy.

Concerning the effect of mechanical deformations, Zadorozhnyy et. al reported that nanocrystalline equiatomic TiFe intermetallic compound synthesized by mechanical alloying has a hydrogen capacity of about 1.4 wt.% at room temperature [41]. Hoda et al found that the first hydrogenation of ball milled TiFe is improved and not sensitive to the air [50]. This study shows clearly that there is a strong relationship between the microstructure of TiFe and its activation for hydrogen absorption. These results show that severe plastic deformation and ball milling could be good ways to improve the hydrogenation properties of TiFe and TiFe-based alloys.

1.3. Research goals

The goal of my PhD was to investigate the hydrogen storage behaviour of TiFe alloy doped with transition elements and/or processed by mechanical deformation. The ultimate goal was to find a combination of alloy composition and mechanical deformation treatment that will produce a low-cost hydride suitable for practical applications. The objective was also to understand the fundamental mechanism of element substitution and mechanical deformation on hydrogen storage properties of TiFe alloy.

1.4. Thesis structure

In this thesis, the experimental details are presented in chapter 2. Chapter 3 covers the effect of different additives on the microstructure and hydrogenation properties of TiFe alloy. More specifically, in section 3.1 the investigation on the addition of zirconium is exposed. Sections 3.2 and 3.3 are respectively on the effect of adding (Zr+2Mn) and (Zr+2V).

The effect of mechanical deformation on the first hydrogenation behaviors of TiFe alloy with 4 wt.% Zr and (Zr+2Mn) as additive is discussed in chapter 4. This investigation helps us to comprehend the relationship between defects and nanocrystallinity with hydrogenation kinetics.

In chapter 5 the conclusion and future work are presented.

2. Experimental details

2.1. Synthesis of materials

All pure elements Fe (99.9%), Ti (99.9%), Zr (99.5%), V (99.9%) and Mn (99.9%) were purchased from Alfa Aesar and used without further purification. The alloys were prepared by arc melting in Ar atmosphere. Each pellet was melted and turned over three times in order to insure homogeneity. Milling was performed on as-cast alloys using hardened stainless steel and balls. Loading of the crucible was done in an argon-filled glovebox. Milling was performed for 15, 30 and 60 minutes using a SPEX 8000M apparatus. The ratio of the mass of balls to mass of powder was 10/1 and the milling vibration speed was 1725 rpm. Cold rolling was done in air for different numbers of rolling passes using a Durston DRM 100 rolling mill. Forging was also done in air for five times using a homemade apparatus.

2.1.1. Arc melting

In this research, all alloys were synthesized using the arc melting machine shown in Fig 2.1. This arc melting machine is made of an electric arc welder, chamber, vacuum system, inert gas system and water system.

Fig 2.1–Photo of arc melting machine.

2.1.2. Ball milling

Ball milling is a widely used as a laboratory method for preparing hydrogen storage materials. During the ball milling process the particles are flattened by the compressive forces which come from the collision of the balls and the particle size is reduced. At the same time, fracturing and cold welding also play an important role in the milling process [51]. In addition the milling process also can increase the specific surface area of materials and create a lot of defects which can improve the absorption and desorption kinetics of materials. In this research the powder mixture was placed inside a crucible with hardened steel balls. Fig 2.2 shows the ball milling machine used in this research.

Fig 2.2–Spex 8000 ball milling machine.

2.1.3. Cold rolling

Rolling techniques could be classified in two types: hot rolling (HR) and cold rolling (CR). In hot rolling the rolling process is done at a temperature higher than the recrystallization temperature. In cold rolling (CR) the process is carried out at a temperature below the recrystallization temperature [52]. In this research, only cold rolling was investigated.

In a cold rolling process, samples are introduced between two rollers where they are compressed as shown in Fig 2.3. In this research, a whole pellet was crushed into some small pieces using a mortar in order to reduce the size of particles sufficiently to be processed by cold rolling. Then these particles were put between two stainless steel plates and introduced in the rolling machine. After rolling, a plate or sheet of the sample was formed. In order to make more rolling passes (1, 5, 10 and 15) the above operation was repeated.

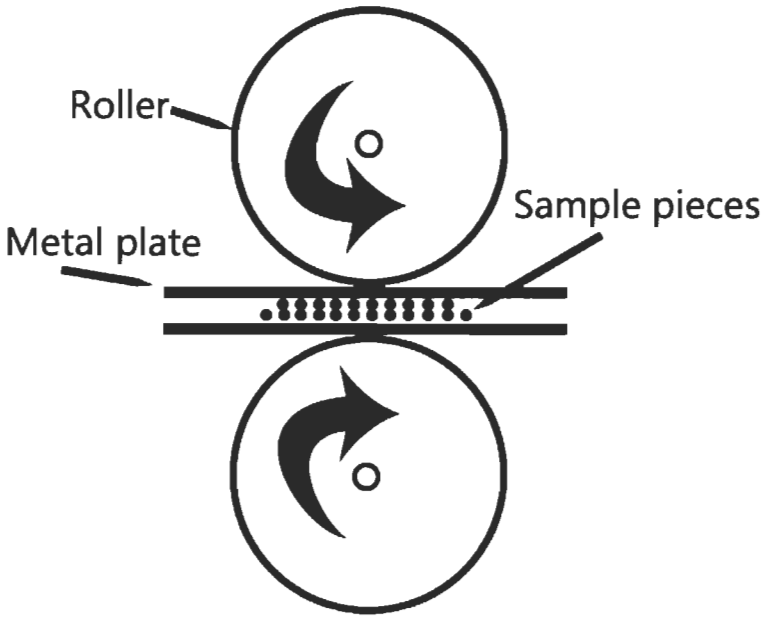

Fig 2.3–Schematic of cold rolling process.

2.1.4. Forging

In forging, a mass and a forging die are necessary. Fig 2.4 shows diagram schematic of a whole forging system that includes rope, pulley, hammer, piston, forging die and steel protection. During the forging process a big hammer is raised above the die and released directly on the piston of the die. The amount of energy depends only on the weight and height of the hammer and the forging time. By adjusting the height of the hammer and the number of forging passes, defects can be created and the crystallite size can be reduced. In this research, the number of forging passes was 5 times and the height of the hammer (23 kg) was 1 m.

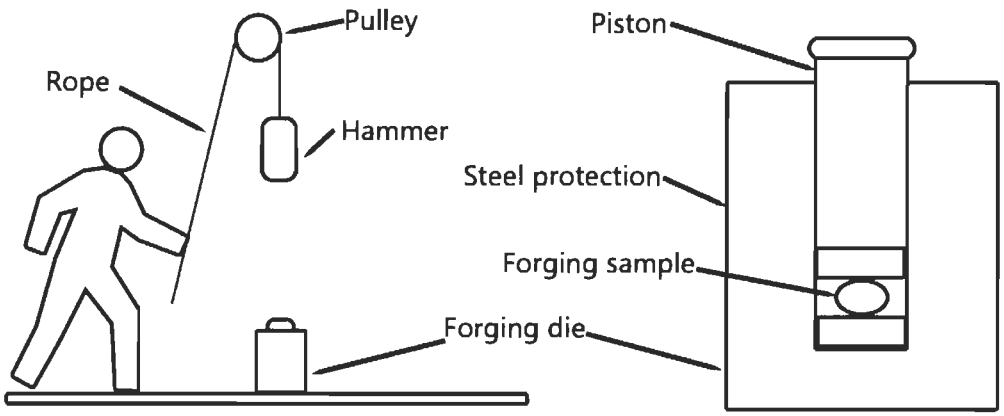

Fig 2.4–Schematic of homemade forging system.

2.2. Characterization of materials

The crystal structure of the samples was determined by X-ray diffraction (XRD; Bruker D8 Focus; Cu Kα radiation). Lattice parameters were evaluated from Rietveld method using TOPAS [53, 54] or GSAS [55-57] software. The hydrogen storage properties were measured by using a home-made Sieverts-type apparatus. Microstructure and chemical analysis were performed using a JEOL JSM-5500 scanning electron microscopy (SEM) equipped with an EDX (Energy Dispersive X-Ray) apparatus from Oxford Instruments. The percentage area of different phases in SEM micrographs was analyzed by image J software [58, 59].

2.2.1. Sieverts-type apparatus

In this research, the hydrogen absorption and desorption measurements were carried out on a homemade apparatus that is based on Sieverts method. Fig 2.5 shows a basic schematic diagram of Sieverts-type apparatus that is made of hydrogen cylinder, valve (A, B and C), pressure gage, vacuum pump and two calibrated volumes (V_1 and V_2) [60]. During the measurement the temperature is stable, so according to the ideal gas equation (*PV=nRT*) the following equation can be written:

$$\Delta n = \frac{P_1 V_1}{Z_{1,T} RT} - \frac{P_2 (V_1 + V_2)}{Z_{2,T} RT} \qquad (2\text{-}1)$$

In this equation $Z_{1,T}$ and $Z_{2,T}$ are compressibility coefficients under P_1 and T and P_2 and T. n is mole number of absorbed hydrogen. R is universal gas constant. T is the temperature.

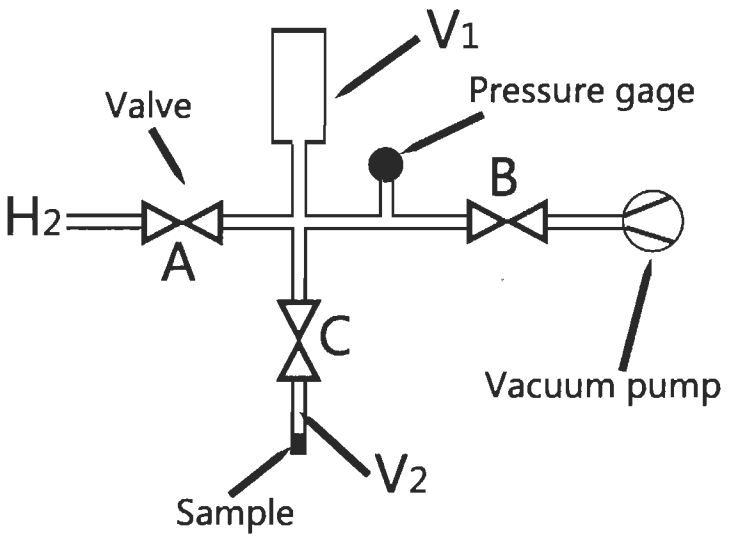

Fig 2.5–Basic schematic diagram of Sieverts-type apparatus [60].

2.2.2. X-ray diffraction

X-ray diffraction (XRD) is a common technique to identify the crystal structure of materials. X-ray diffraction is based on constructive interference of monochromatic X-rays and a crystalline sample. Equation (2-2) is the Bragg equation that relates the wavelength of electromagnetic radiation and the diffraction angle to the lattice parameters in a crystalline sample [61].

$$2d\ sin\ \theta = n\lambda \tag{2-2}$$

Fig 2.6 shows the schematic diagram of Bragg diffraction. When Bragg's Law is satisfied, the constructive interference of monochromatic X-rays and a crystalline sample happens. Then the scanning detector will pick up a Bragg reflection at this angle. The inter-layer spacings of atoms (d) can be calculated according to the positions of these reflections [62].

Each substance has its own specific crystal structure and lattice parameters. Analysis of the diffraction pattern helps us to identify the phase using important information obtained from the diffraction pattern, for example the crystallinity, lattice parameters, crystallite size, microstrain and so on [63].

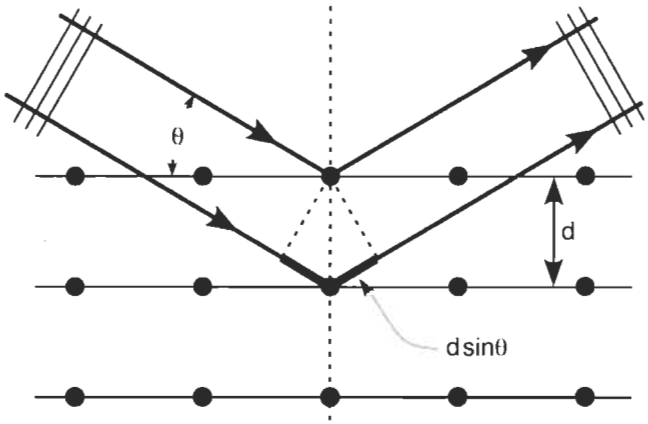

Fig 2.6–Schematic diagram of Bragg diffraction [64].

2.2.3. Synchrotron

A synchrotron is a particular type of accelerator, descended from the cyclotron, in which the accelerating charged particle beam travels around a closed-loop path. The magnetic field which bends the particle beam into its closed path increases with time during the accelerating process, being synchronized to the increasing kinetic energy of the particles [65].

Fig 2.7 shows a typical synchrotron machine. A Synchrotron consists of the electron gun (1), linear accelerator (2), booster ring (3), storage ring (4), bending magnets (not shown in Fig 2.7), beam lines (5) and the end stations (6). In this research I used the synchrotron radiation for diffraction from Canadian Light Source (CLS).

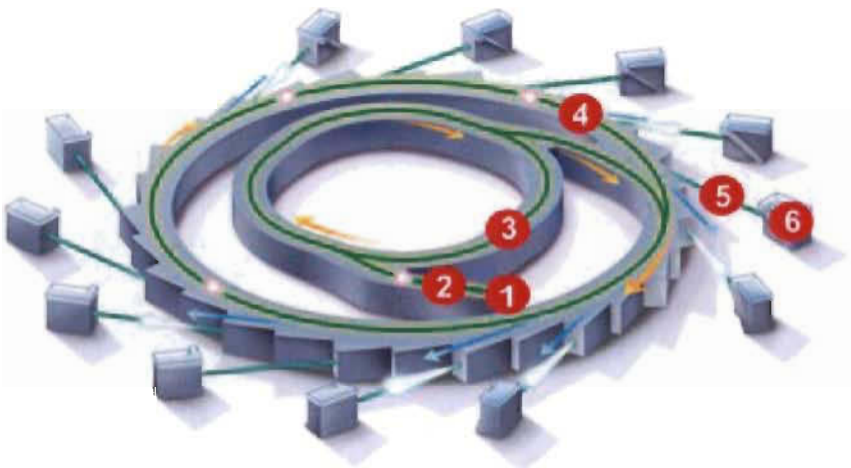

Fig 2.7–Schematic diagram of synchrotron system [66].

A typical diffraction image obtained from synchrotron is shown in Fig 2.8. It can be seen clearly that there are some annulus which imply LaB_6 phase.

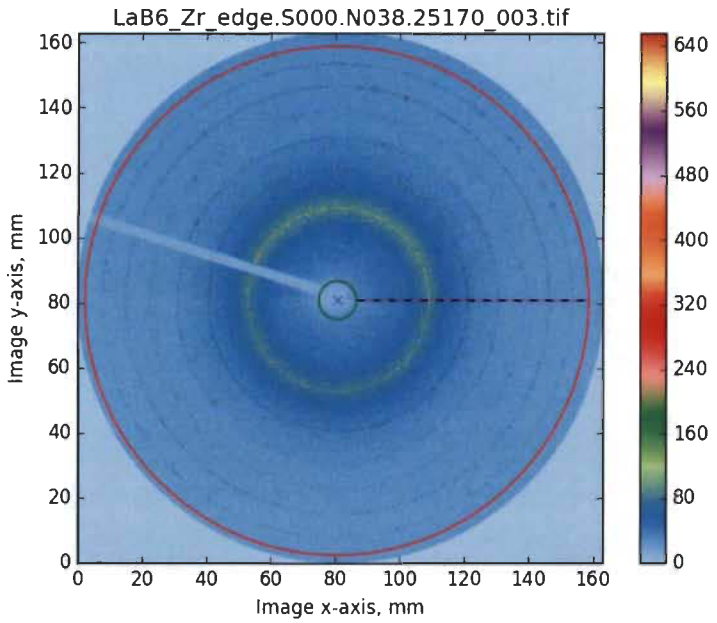

Fig 2.8–Original image of LaB_6 from synchrotron.

In order to know the detailed phase content, lattice parameters and crystal structure, GSAS- II software was used to convert the original image into common curves. Fig 2.9 shows the synchrotron pattern of LaB_6 using GSAS- II software.

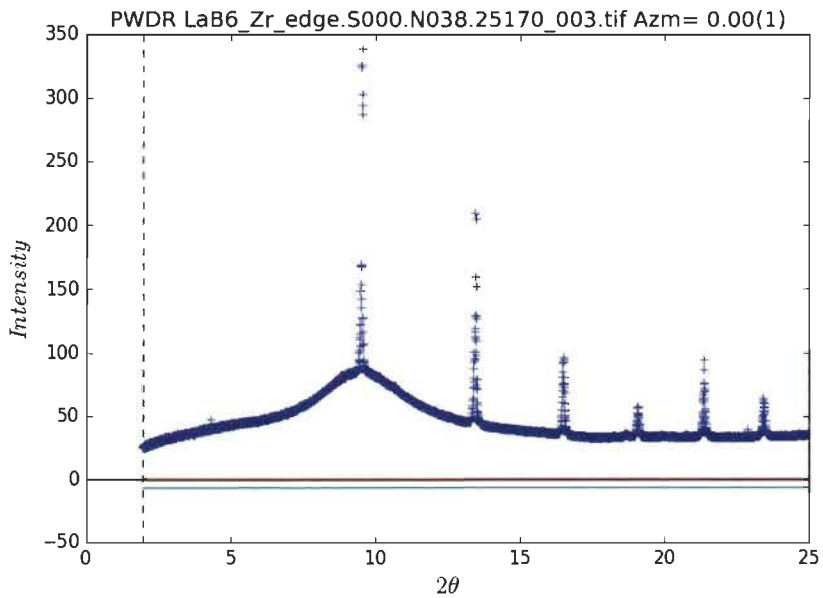

Fig 2.9–Synchrotron pattern of LaB_6 using GSAS- II software.

2.2.4. Scanning electron microscopy

A scanning electron microscope (SEM) can produce images of a sample by scanning the surface with a focused beam of electrons. The electrons interact with atoms in the sample, producing various signals that contain information about the sample's surface topography and composition [67].

A SEM apparatus consists of three parts: vacuum chamber, electron beam and imaging system. Fig 2.10 shows a typical schematic of a whole SEM apparatus. Based on the interaction between electron and matter, SEM uses a beam of high energy electrons generated by an electron gun to focus on the surface of material using magnetic lenses. When the surface of the material is bombarded with high energy electron beam, the excited region will produce various kinds of electrons (such as secondary electrons, auger electrons, backscattered electrons and transmitted electrons). Secondary electrons are used to study the morphology and topography of samples and backscattered electrons are sensitive to contrasts in multiphase samples [68].

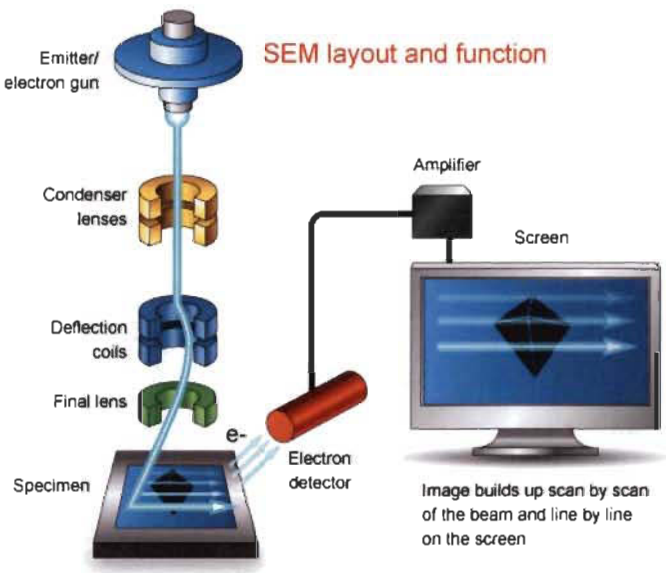

Fig 2.10–Schematic of a whole scanning electron microscope system [69].

3. Effect of different additives on the microstructure and hydrogenation properties of TiFe alloy

3.1. Hydrogen storage properties of $Ti_{0.95}FeZr_{0.05}$, $TiFe_{0.95}Zr_{0.05}$ and $TiFeZr_{0.05}$ alloys

In a previous work, it is found that adding 4 wt.% zirconium to TiFe alloy can improve the first hydrogenation kinetics [70]. This investigation showed that a small amount of zirconium (about 1 atomic %) is in solid solution in the main TiFe phase while the abundance of zirconium is much higher in the secondary phase. This raised the question of the localization of zirconium in the TiFe matrix. Does zirconium substitute on the titanium or the iron site or goes in some interstitial site? To answer this question the microstructure and hydrogen storage properties of three closely related compositions: $Ti_{0.95}FeZr_{0.05}$, $TiFe_{0.95}Zr_{0.05}$ and $TiFeZr_{0.05}$ have been investigated.

3.1.1. Results and discussion

3.1.1.1. Morphology

Fig 3.1.1 shows backscattered electron micrographs of $Ti_{0.95}FeZr_{0.05}$, $TiFe_{0.95}Zr_{0.05}$ and $TiFeZr_{0.05}$ alloys prepared by arc melting. Surprisingly, even if the compositions are very similar, they have totally different microstructure.

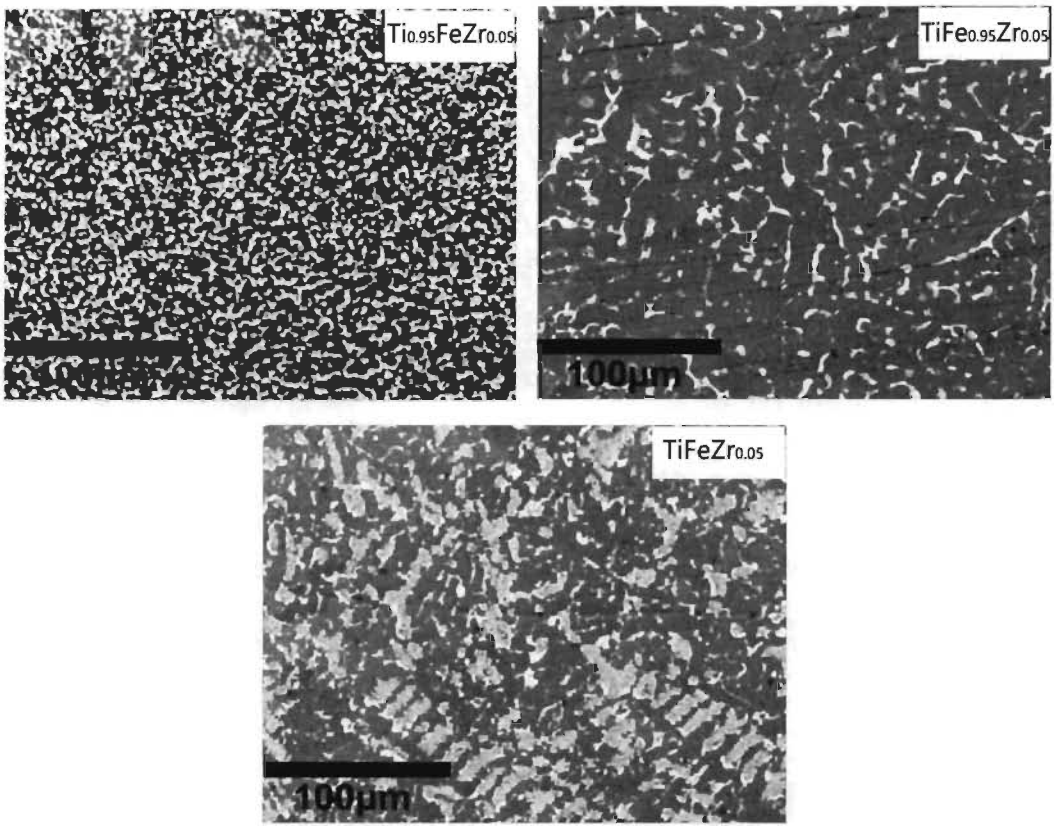

Fig 3.1.1–Backscattered electron micrographs of $Ti_{0.95}FeZr_{0.05}$, $TiFe_{0.95}Zr_{0.05}$ and $TiFeZr_{0.05}$ alloys prepared by arc melting.

Using image J software, the bright and dark phase areas were computed and the numerical values are reported in Table 3.1.1. It is found that the bright phase surface area is much lower in the $TiFe_{0.95}Zr_{0.05}$ sample than the other two compositions.

Table 3.1.1-Percentage of bright and dark areas for $Ti_{0.95}FeZr_{0.05}$, $TiFe_{0.95}Zr_{0.05}$ and $TiFeZr_{0.05}$ micrographs shown in Fig 3.3.1.

Phase	$Ti_{0.95}FeZr_{0.05}$	$TiFe_{0.95}Zr_{0.05}$	$TiFeZr_{0.05}$
Bright (%)	37	11	31
Dark (%)	63	89	69

In order to know the chemical composition of the bright and dark phases, EDX measurement was performed on each alloy. First, the bulk atomic abundance was measured and compared to the nominal composition. The numerical values are

reported in Table 3.1.2. It is clear that the atomic % of all elements are very close to the nominal composition.

Table 3.1.2-Bulk atomic abundance and nominal bulk atomic abundance as measured by EDX of $Ti_{0.95}FeZr_{0.05}$, $TiFe_{0.95}Zr_{0.05}$ and $TiFeZr_{0.05}$ alloys.

Sample		Ti(at.%)	Fe(at.%)	Zr(at.%)
$Ti_{0.95}FeZr_{0.05}$	Nominal composition	47.5	50.0	2.5
	Measurement	47.0	50.3	2.7
$TiFe_{0.95}Zr_{0.05}$	Nominal composition	50.0	47.5	2.5
	Measurement	51.3	45.8	2.9
$TiFeZr_{0.05}$	Nominal composition	48.8	48.8	2.4
	Measurement	47.3	49.7	3.1

Second, the atomic composition of the dark and bright phases of each alloy was measured. The microstructure and element mapping of $Ti_{0.95}FeZr_{0.05}$ alloy are shown in Fig 3.1.2. It is clear that zirconium is concentrated in the secondary phase and iron and titanium are evenly distributed.

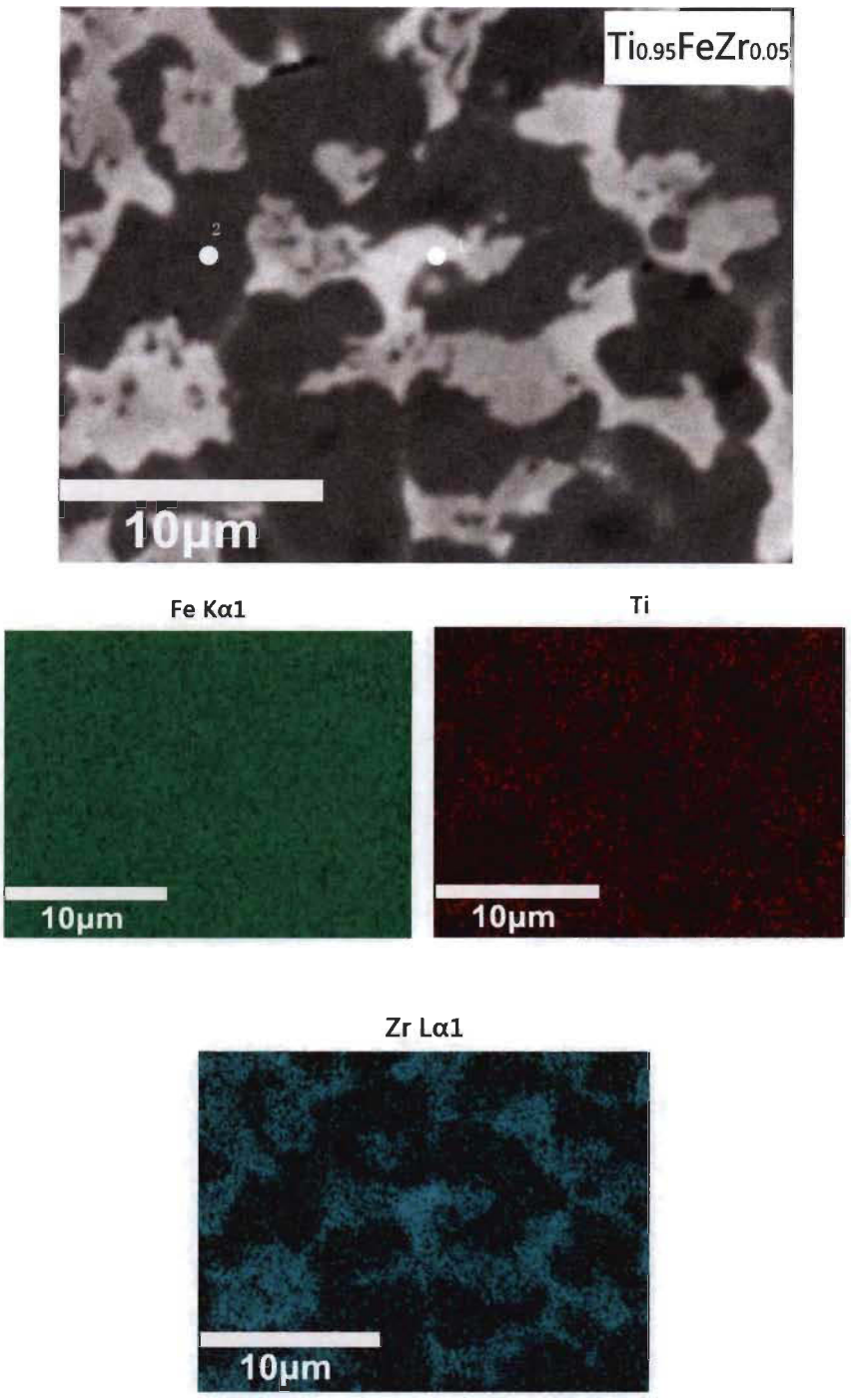

Fig 3.1.2–Backscattered electron micrograph of $Ti_{0.95}FeZr_{0.05}$ alloy prepared by arc melting with elements mapping.

The elemental distribution of $TiFe_{0.95}Zr_{0.05}$ alloy is presented in Fig 3.1.3. As for the preceding composition, zirconium is mainly located in the bright phase. However, iron is slightly depleted in the bright phase. That is confirmed by the quantitative analysis reported in Table 3.1.2.

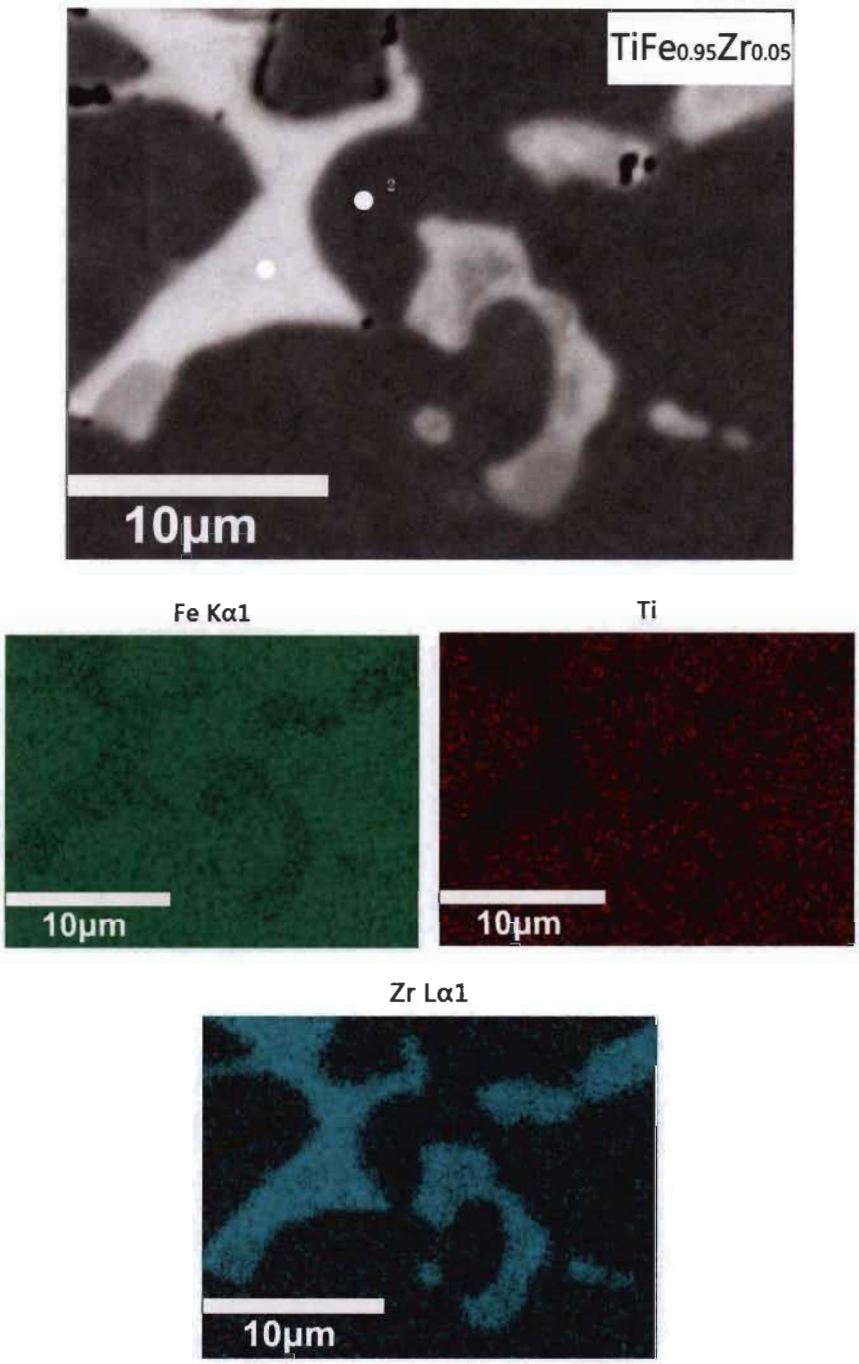

Fig 3.1.3–Backscattered electron micrograph of $TiFe_{0.95}Zr_{0.05}$ alloy prepared by arc melting with elements mapping.

Fig 3.1.4 shows the micrograph and element mapping of $TiFeZr_{0.05}$. Even if the morphology is different, the elemental distribution seems similar to the $Ti_{0.95}FeZr_{0.05}$ alloy.

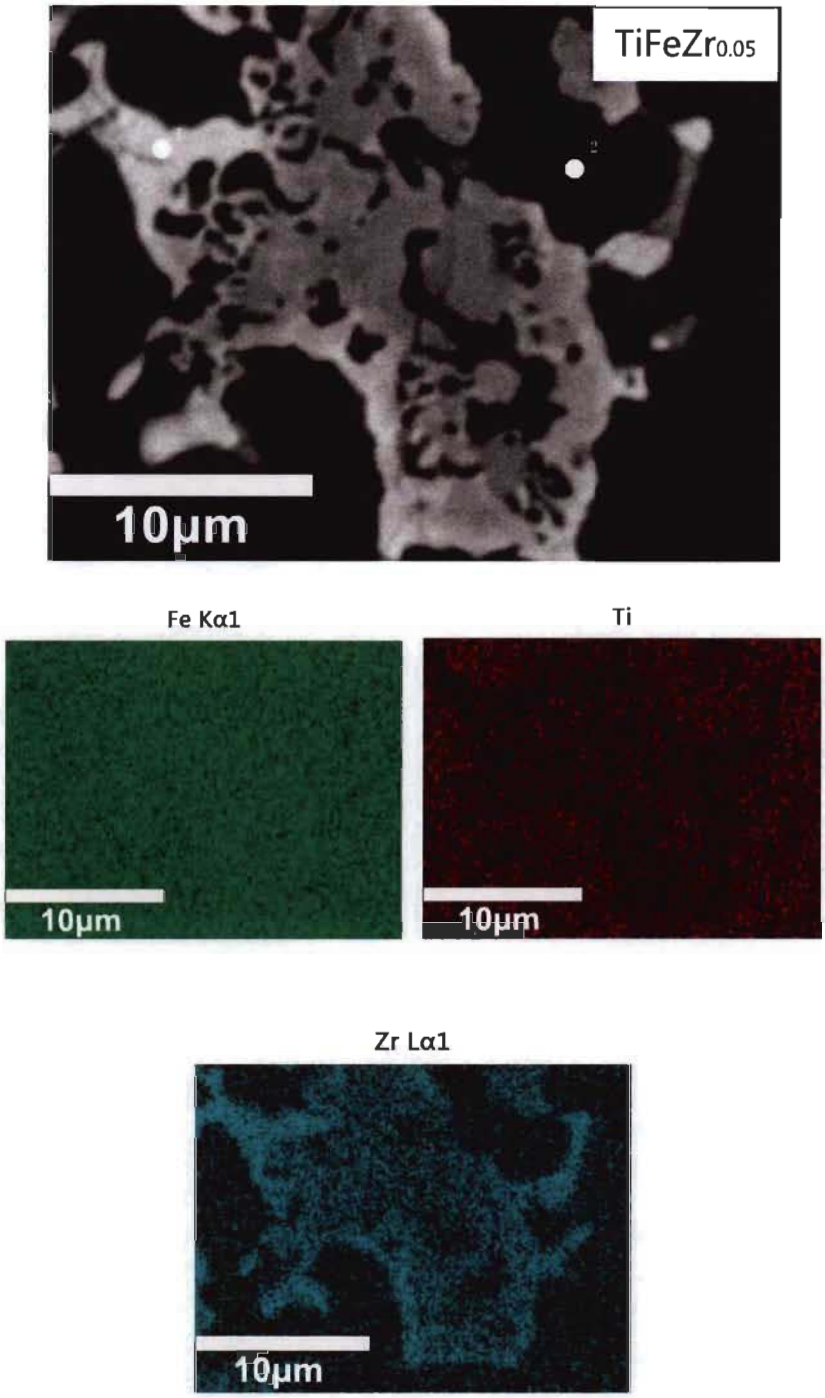

Fig 3.1.4–Backscattered electron micrograph of $TiFeZr_{0.05}$ alloy prepared by arc melting with elements mapping.

Table 3.1.3-EDX analysis showing the dark phase element composition of $Ti_{0.95}FeZr_{0.05}$, $TiFe_{0.95}Zr_{0.05}$ and $TiFeZr_{0.05}$ alloys.

Element (Atomic%)	$Ti_{0.95}FeZr_{0.05}$	$TiFe_{0.95}Zr_{0.05}$	$TiFeZr_{0.05}$
Fe	48.8	47.9	48.1
Ti	50.8	51.5	51.3
Zr	0.5	0.6	0.7

Table 3.1.4-EDX analysis showing the bright phase element composition of $Ti_{0.95}FeZr_{0.05}$, $TiFe_{0.95}Zr_{0.05}$ and $TiFeZr_{0.05}$ alloys.

Element (Atomic%)	$Ti_{0.95}FeZr_{0.05}$	$TiFe_{0.95}Zr_{0.05}$	$TiFeZr_{0.05}$
Fe	47.8	36.3	47.4
Ti	37.6	44.3	38.5
Zr	14.6	19.4	14.0

For each alloy, a quantitative analysis of the dark phase and bright phase was performed and reported in Table 3.1.3 and Table 3.1.4, respectively. From Table 3.1.3, it is clear that the dark phase of the three alloys has identical elements abundances. In particular, it should be noted that zirconium abundance is less than 1 atomic %.

Table 3.1.4 indicates that zirconium is predominantly confined into the bright phase but actually, the bright phase is mainly composed of titanium and iron. A closer inspection reveals that the bright phase of $Ti_{0.95}FeZr_{0.05}$ and $TiFeZr_{0.05}$ alloys have almost the same composition. In fact, by comparing Table 3.1.1 and Table 3.1.4 it is clear that those two alloys also have similar bright phase areas. In the case of $TiFe_{0.95}Zr_{0.05}$, the bright phase has a higher percentage of zirconium than the other two compositions but also a smaller area of bright phase. This agrees very well with the fact that zirconium is essentially found only in the bright phase. As all these compositions have the same amount of zirconium, if the concentration of zirconium is

higher, then the area of the bright phase should be smaller. This is confirmed by Tables 3.1.1 and 3.1.4.

3.1.1.2. Structural characterization

The XRD patterns of $Ti_{0.95}FeZr_{0.05}$, $TiFe_{0.95}Zr_{0.05}$ and $TiFeZr_{0.05}$ alloys in as-cast state are presented in Fig 3.1.5. It can be clearly seen that all alloys prepared are made of TiFe phase. However, the secondary phase seen in the SEM micrographs could not be seen on the X-ray patterns. As the XRD was from a copper target the fluorescence from iron is strong and produces an important background which makes the detection of a secondary phase more difficult. Fluorescence is also the reason for the sloping background of all these patterns.

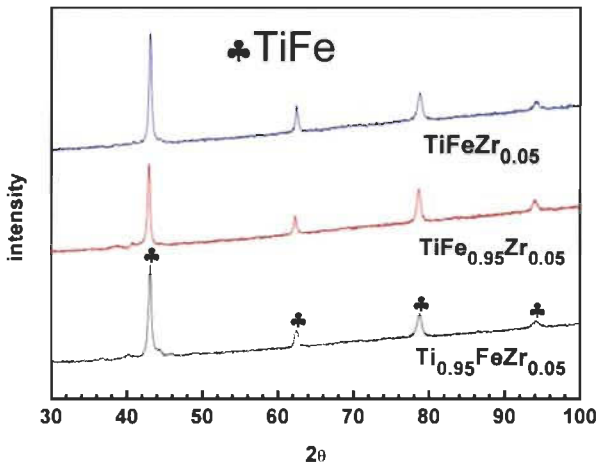

Fig 3.1.5–XRD of $Ti_{0.95}FeZr_{0.05}$, $TiFe_{0.95}Zr_{0.05}$ and $TiFeZr_{0.05}$ alloys in as-cast state.

Table 3.1.5 shows the lattice parameters of TiFe phase in as-cast alloys as determined from Rietveld analysis. The lattice parameters of $Ti_{0.95}FeZr_{0.05}$ and $TiFeZr_{0.05}$ are closer to each other than to $TiFe_{0.95}Zr_{0.05}$ but globally they differ by only 0.1%.

Table 3.1.5-Lattice parameter *a* (in Å) of TiFe phase in as cast alloys as determined from Rietveld analysis. The number in parenthesis is error.

Alloy	$Ti_{0.95}FeZr_{0.05}$	$TiFe_{0.95}Zr_{0.05}$	$TiFeZr_{0.05}$
a	2.9845(7)	2.9804(9)	2.9830(6)

3.1.1.3. First hydrogenation

Fig 3.1.6 shows the first hydrogenation kinetics of all the compositions as measured at room temperature under 2 MPa of hydrogen. It can be seen that $Ti_{0.95}FeZr_{0.05}$ alloy readily absorbs hydrogen without incubation time. Compositions $TiFe_{0.95}Zr_{0.05}$ and $TiFeZr_{0.05}$ have identical first hydrogenation curves while $Ti_{0.95}FeZr_{0.05}$ has a faster first hydrogenation kinetics than the two other alloys. This is somewhat surprising, considering the facts that $Ti_{0.95}FeZr_{0.05}$ and $TiFeZr_{0.05}$ have very similar secondary phase composition and abundance, but they still have different first hydrogenation kinetics. The answer to this may be given by Fig 3.1.1. This figure clearly shows that the bright phase distribution is much finer in $Ti_{0.95}FeZr_{0.05}$ alloy than the other two alloys. In addition, it also clearly shows that the fraction of interphase boundaries is higher in $Ti_{0.95}FeZr_{0.05}$ than that in $TiFeZr_{0.05}$. Under the hypothesis that the bright phase and interphase boundaries act as a gateway for hydrogen then, it is reasonable that the first hydrogenation kinetics will be faster for $Ti_{0.95}FeZr_{0.05}$ alloy than the other two.

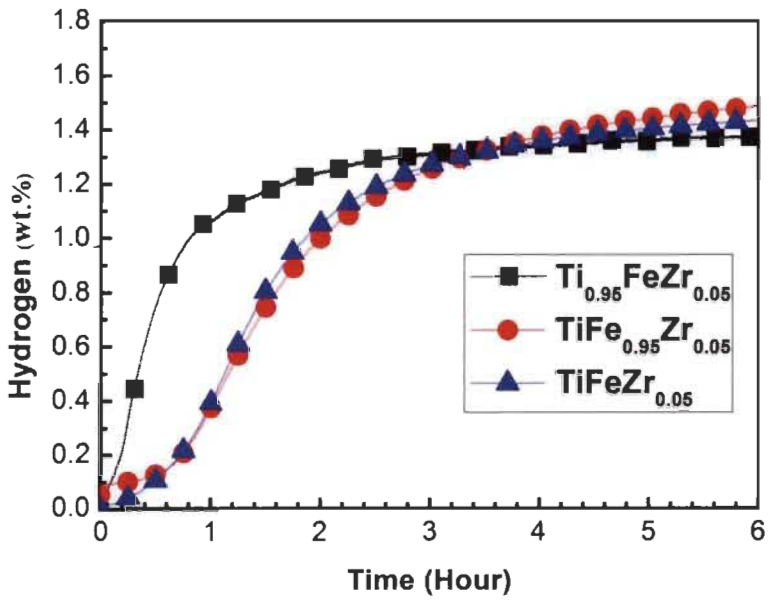

Fig 3.1.6–First hydrogenation behaviour of $Ti_{0.95}FeZr_{0.05}$, $TiFe_{0.95}Zr_{0.05}$ and $TiFeZr_{0.05}$ alloys at room temperature under 2 MPa hydrogen pressure.

3.1.1.4. Pressure-composition isotherms

After the first hydrogenation cycle, the pressure-composition isotherms were measured at room temperature. The results are shown in Fig 3.1.7. The compositions $TiFeZr_{0.05}$ and $Ti_{0.95}FeZr_{0.05}$ present essentially the same curve, the only small difference is that the alloy $TiFeZr_{0.05}$ has a slightly larger capacity. The alloy $TiFe_{0.95}Zr_{0.05}$ has a higher capacity than the two other alloys and its hydrides are more stable as indicated by the lower plateau pressures. Moreover, this higher capacity is mainly due to the lower plateau pressure (monohydride) while the dihydride capacity is the same for the three alloys.

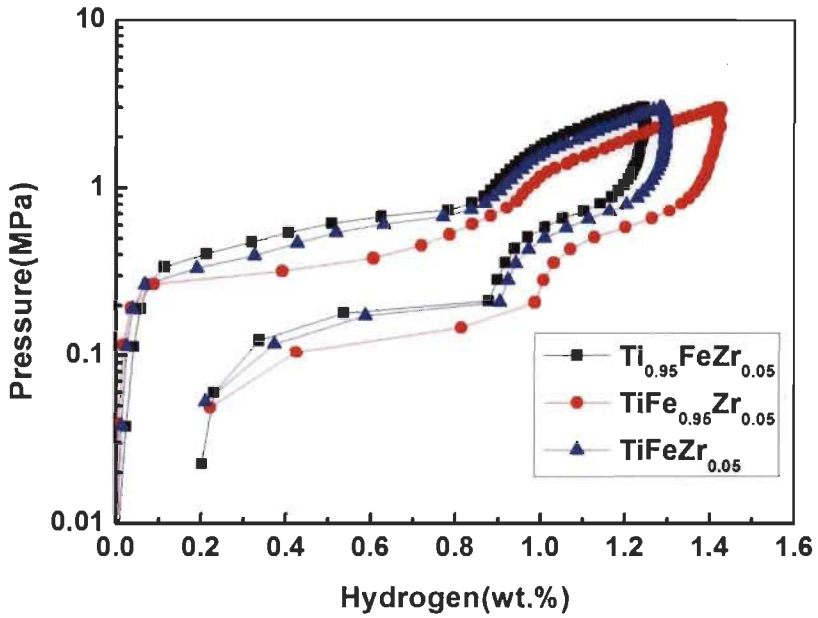

Fig 3.1.7–PCT of $Ti_{0.95}FeZr_{0.05}$, $TiFe_{0.95}Zr_{0.05}$ and $TiFeZr_{0.05}$ alloys at room temperature.

3.1.2. Conclusion

The microstructure, crystal structure, and hydrogenation characteristics of $Ti_{0.95}FeZr_{0.05}$, $TiFe_{0.95}Zr_{0.05}$ and $TiFeZr_{0.05}$ alloys have been investigated. The following observations have been made. For all alloys zirconium is mainly located in the bright phase.

(1) $Ti_{0.95}FeZr_{0.05}$ alloy has faster first hydrogenation kinetics than the two other alloys due to the very fine distribution of the bright secondary phase.

(2) $TiFeZr_{0.05}$ and $Ti_{0.95}FeZr_{0.05}$ alloys show a similar curve of pressure-composition isotherm, but the former has a slightly bigger capacity. In addition, $TiFe_{0.95}Zr_{0.05}$ alloy shows the highest hydrogen capacity.

(3) These results show that a very slight variation of composition could have an important effect of microstructure of the alloy and its hydrogen storage behaviors.

3.2. Microstructure and hydrogenation properties of TiFe doped with (Zr+2Mn) as additive

From previous investigations, it was clear that the first hydrogenation of TiFe alloy could be improved by adding Zr_7Ni_{10} [49], Zr [70, 71] and Mn [72]. The good effect of Zr and Mn leads to the investigation of (Zr+2Mn) as an additive to TiFe alloy. In this chapter the effects of different (Zr+2Mn) content on the microstructure, hydrogen storage properties and air resistance of TiFe alloy are reported.

3.2.1. Results and discussion

3.2.1.1. Morphology

Fig 3.2.1 shows secondary electron micrographs of TiFe+x wt.% (Zr+2Mn) (x=2, 4, 8, 12) alloys prepared by arc melting. It is clear that these samples exhibit different microstructures which include bright and dark phases. Using image J software, the proportion of bright and dark phase surface was estimated and is reported in Table 3.2.1. From Table 3.2.1 and Fig 3.2.1 it can be seen that the bright phase area increases with x, reaching almost 50% at x=12 wt% (Zr+2Mn).

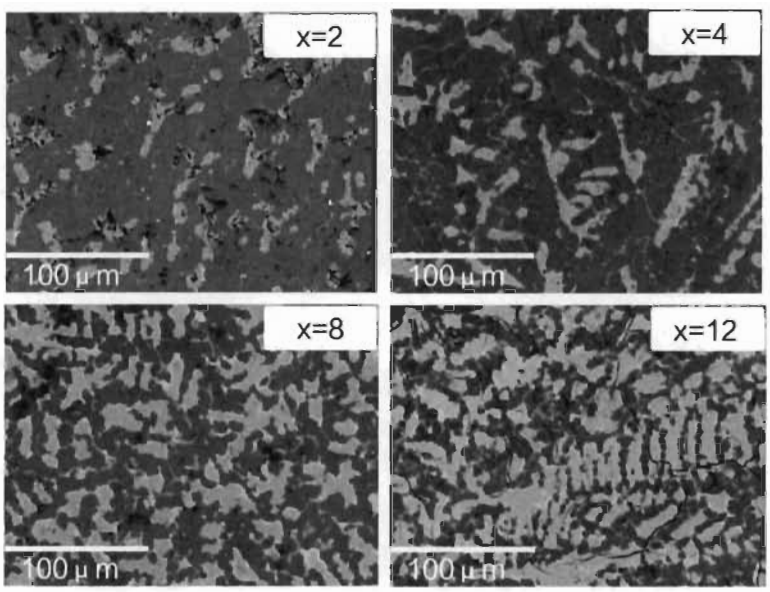

Fig 3.2.1–Backscattered electron micrographs of arc melted TiFe+x wt.% (Zr+2Mn) (x=2, 4, 8, 12) alloys.

Table 3.2.1-Percentage of bright and dark phases area in as-cast TiFe+x wt.% (Zr+2Mn) (x=2, 4, 8, 12) alloy as shown in Fig 3.2.1.

Phase	x=2	x=4	x=8	x=12
Bright (%)	18	21	38	48
Dark (%)	82	79	62	52

The microstructure of x=2, 4, 8 and 12 are shown in Fig 3.2.1. It is clear from Fig 3.2.1 that all alloys are formed of at least two different phases. Using EDX, the bulk atomic abundance was measured and compared to the nominal composition. The results shown in Table 3.2.2 prove that the atomic abundances of all elements are very close to the nominal compositions.

Table 3.2.2-Nominal and measured bulk atomic abundance of TiFe+x wt.% (Zr+2Mn) (x=2, 4, 8, 12) alloys.

	Sample	Ti(Atomic%)	Fe(Atomic%)	Zr(Atomic%)	Mn(Atomic%)
x=2	Nominal composition	49.2	49.2	0.5	1.0
	Measured	48.7	49.6	0.6	1.1
x=4	Nominal composition	48.5	48.5	1.0	2.0
	Measured	48.8	47.8	1.2	2.1
x=8	Nominal composition	47.0	46.6	2.0	4.0
	Measured	47.3	49.7	2.4	3.8
x=12	Nominal composition	45.8	45.8	2.8	5.6
	Measured	45.9	45.4	3.3	5.4

The chemical composition of individual phase was thereafter investigated for each value of x. For each composition, an elemental mapping was performed as well as a point analysis. For all compositions, point 1 identifies the bright phase and point 2 the

dark phase. The quantitative analysis of points 1 and 2 are reported in Table 3.2.3 and Table 3.2.4 respectively.

The microstructure and element mapping of x=2 are shown in Fig 3.2.2. It shows that iron and titanium are well distributed in both phases. Manganese is also evenly spread while zirconium is clearly more abundant in the bright phase. This was confirmed by the quantitative analysis of points 1 and 2 reported in Table 3.2.3 and 3.2.4. It can be seen that the dark phase (point 2) has a composition very close to TiFe with only a small amount of manganese and effectively no zirconium. Bright phase composition (point 1) indicates that almost all zirconium are located in the bright phase. However, the bright phase is still mainly composed of iron and titanium.

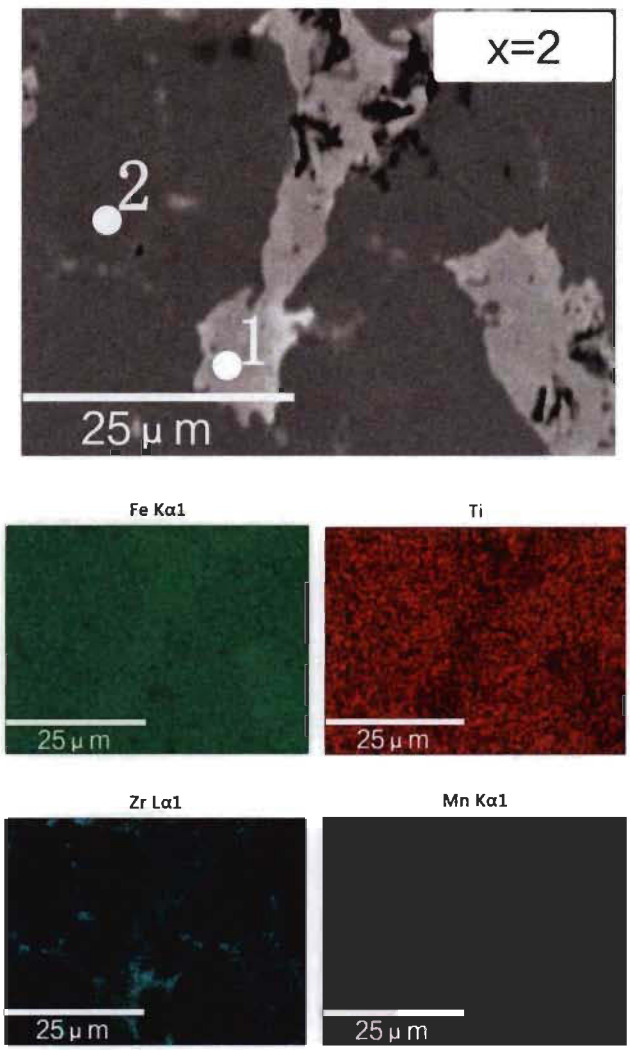

Fig 3.2.2–Backscattered electron micrograph of arc melted TiFe+2 wt.% (Zr+2Mn) alloy with EDX mapping and chemical composition at different sites.

Fig 3.2.3 shows the micrograph and element mapping for x=4. As for the previous composition, it is found that manganese, iron and titanium seem to be evenly distributed. However, the point analysis reported in Table 3.2.3 and 3.2.4 shows that, compared to x=2, the dark phase has a slight reduction of iron content accompanied by a small increase of manganese. In the case of the bright phase, iron composition decreases but the main fact is that manganese and zirconium contents increased by about 1.7 wt.% for each element.

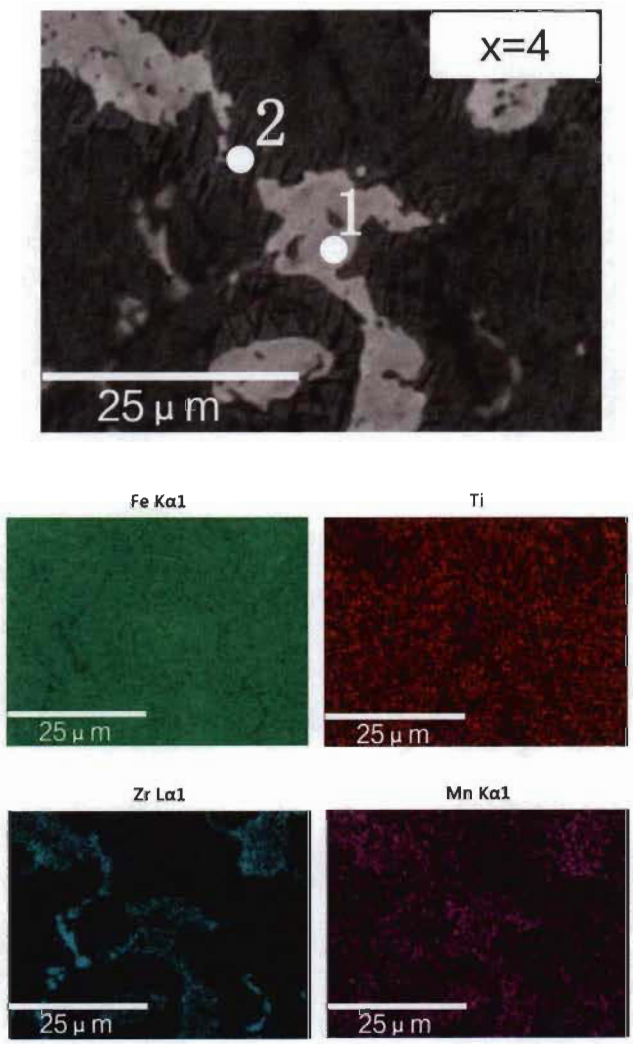

Fig 3.2.3–Backscattered electron micrograph of arc melted TiFe+4 wt.% (Zr+2Mn) alloy with EDX mapping and chemical composition at different sites

Fig 3.2.4 presents the micrograph and element mapping for x=8. The situation is similar to the previous two cases but here the mapping suggests that the zirconium content in the secondary phase is higher. This is confirmed by the point analysis

results presented in Tables 3.2.3 and 3.2.4. On the other hand, in the TiFe phase the iron content slightly decreased and the manganese content increased while the titanium and zirconium contents almost did not change.

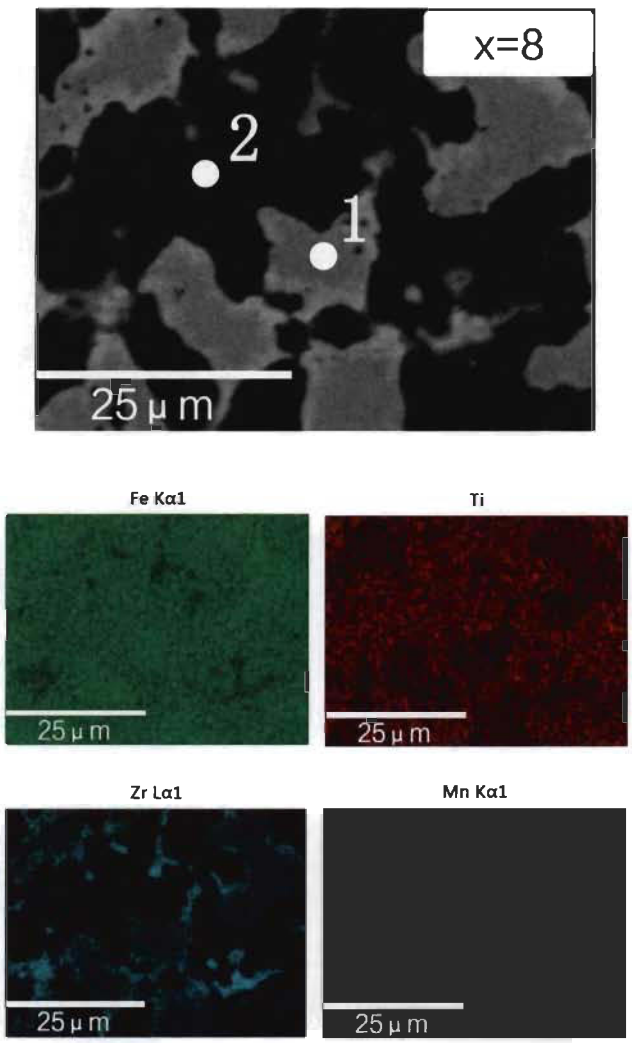

Fig 3.2.4–Backscattered electron micrograph of arc melted TiFe+8 wt.% (Zr+2Mn) alloy with EDX mapping and chemical composition at different sites

Fig 3.2.5 shows the micrograph and element mapping for x=12. It is clear that the bright phase occupies a much larger area than in the previous compositions. Also, it should be noticed that the zirconium abundance seems to be higher on the edge of the bright areas. In the dark phase, the proportion of titanium and zirconium did not change compared to x=8 but the amount of manganese increased and the amount of iron decreased in the same proportions.

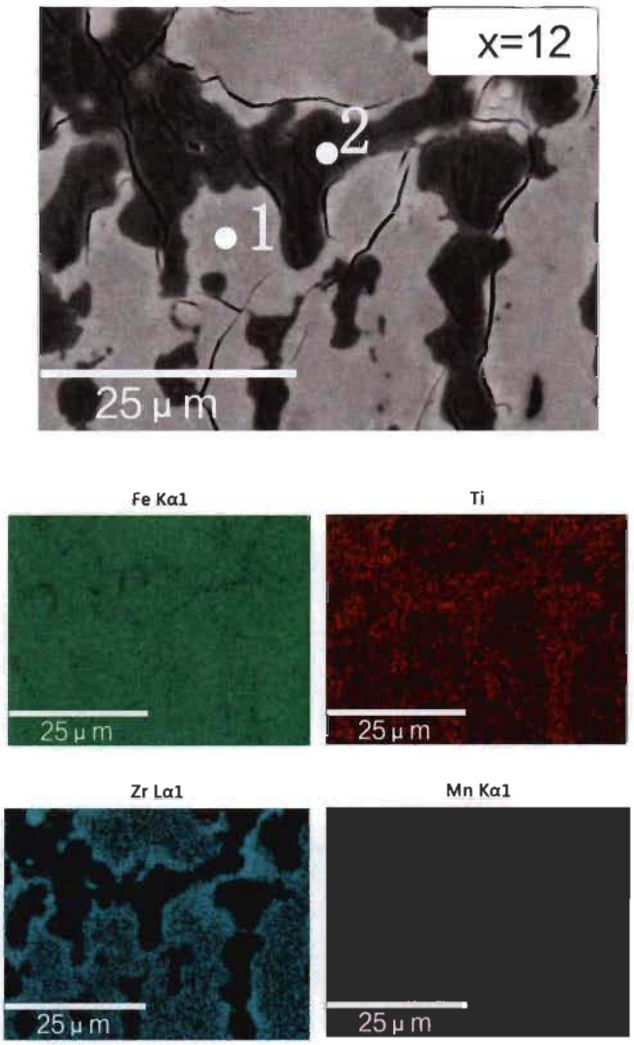

Fig 3.2.5–Backscattered electron micrograph of arc melted TiFe+12 wt.% (Zr+2Mn) alloy with EDX mapping and chemical composition at different sites

Table 3.2.3-EDX of bright phase (point 1) of TiFe+x wt.% (Zr+2Mn) (x=2, 4, 8, 12) alloys.

Element (Atomic%)	x=2	x=4	x=8	x=12
Fe	57.0±0.2	54.5±0.3	53.9±0.3	51.4±0.3
Ti	40.6±0.3	39.7±0.3	39.0±0.2	38.1±0.3
Mn	1.7±0.1	3.3±0.1	4.5±0.2	6.7±0.2
Zr	0.7±0.1	2.4±0.1	2.6±0.1	3.8±0.1

Table 3.2.4-EDX of dark phase (point 2) of TiFe+x wt.% (Zr+2Mn) (x=2, 4, 8, 12) alloys.

Element (Atomic%)	x=2	x=4	x=8	x=12
Fe	49.2±0.2	47.7±0.3	46.9±0.2	45.9±0.3
Ti	50.1±0.3	50.5±0.3	50.5±0.3	50.3±0.3
Mn	0.7±0.1	1.5±0.1	2.3±0.1	3.4±0.2
Zr	0.0	0.3±0.1	0.3±0.1	0.5±0.1

From Tables 3.2.3 and 3.2.4, general conclusions on the evolution of chemical compositions in the dark and bright phase can be drawn. In the case of the dark phase it has an almost perfect TiFe composition for x=2 with only a small amount of manganese substituting with iron. When x increases, the titanium proportion stays the same and manganese substitute in greater proportion with iron. Zirconium is present in only small concentration and does not increase with x. The behavior is different for the secondary phase. When x increases the proportion of titanium and iron decrease but the rate of change is more important for iron than for titanium. Zirconium and manganese proportions both increase with x but the rate is larger for manganese. In fact, the proportion of iron plus zirconium and titanium plus manganese are stable when x increases, suggesting that in the bright phase zirconium substitute with iron and manganese substitute with titanium. This means that different substitutions schemes are present in the bright and dark phases.

3.2.1.2. Crystal structural characterization

The XRD patterns of the TiFe+x wt.% (Zr+2Mn) (x=2, 4, 8, 12) alloys in as-cast state are presented in Fig 3.2.6. It can clearly be seen that all alloys prepared show TiFe phase, but there are small peaks at around 37°, 40°, 44° that most probably are associated with the secondary phases seen in the SEM micrographs. By inspection, we noticed that these peaks match a crystal structure of $MgZn_2$ type. But the relatively

small amount of secondary phase and the broadness of the peaks make a definitive identification impossible.

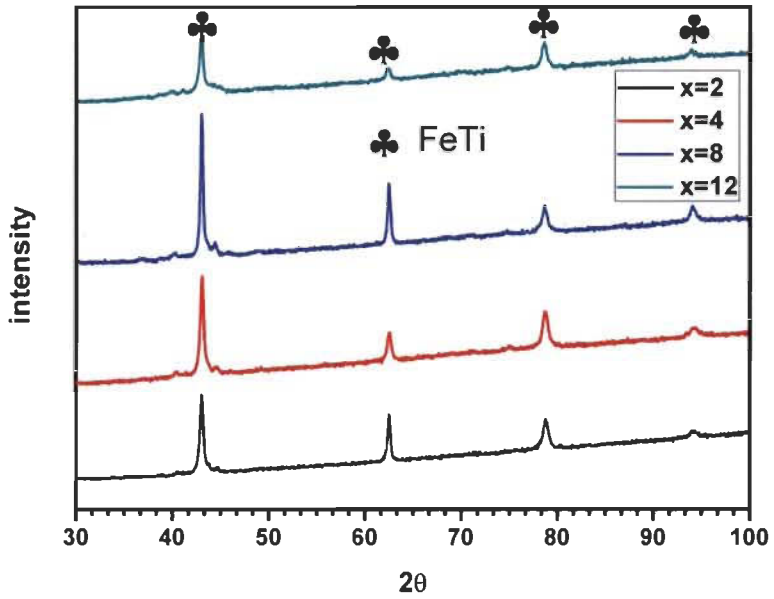

Fig 3.2.6–Powder diffraction patterns of as-cast TiFe+x wt.% (Zr+2Mn) (x=2, 4, 8, 12) alloys.

Table 3.2.5 shows the lattice parameters *a* (in Å) of TiFe phase in as-cast TiFe+x wt.% (Zr+2Mn) (x=2, 4, 8, 12) alloys as determined by Rietveld's analysis. It can be seen that the lattice parameter of TiFe phase increases with x except x=8.

Table 3.2.5-Lattice parameters *a* (in Å) of TiFe phase in as cast TiFe+x wt.% (Zr+2Mn) (x=2, 4, 8, 12) alloys as determined by Rietveld analysis. The number in parenthesis is error.

Phase	x=2	x=4	x=8	x=12
a	2.9796(3)	2.9798(3)	2.9796(3)	2.9856(7)

3.2.1.3. First hydrogenation

Fig 3.2.7 shows the first hydrogenation of TiFe+x wt.% (Zr+2Mn) (x=2, 4, 8, 12) alloys performed under an initial hydrogen pressure of 3 MPa and at room temperature. It can be seen that x=2 didn't absorb the hydrogen even after 12 h. The incubation time for x=4 is about 4.5 h. For x=8 and 12, the alloys show no incubation

time and directly absorb hydrogen. The reaction kinetics of the first hydrogenation increases with x. As the composition of TiFe phase does not drastically change when x increases we could safely conclude that activation kinetics is due to the secondary phase. Fig 3.2.1 clearly shows that the bright phase is more abundant and better distributed in the x=12 alloy than the other three alloys. This indicates that the microstructure plays an important role in the first hydrogenation.

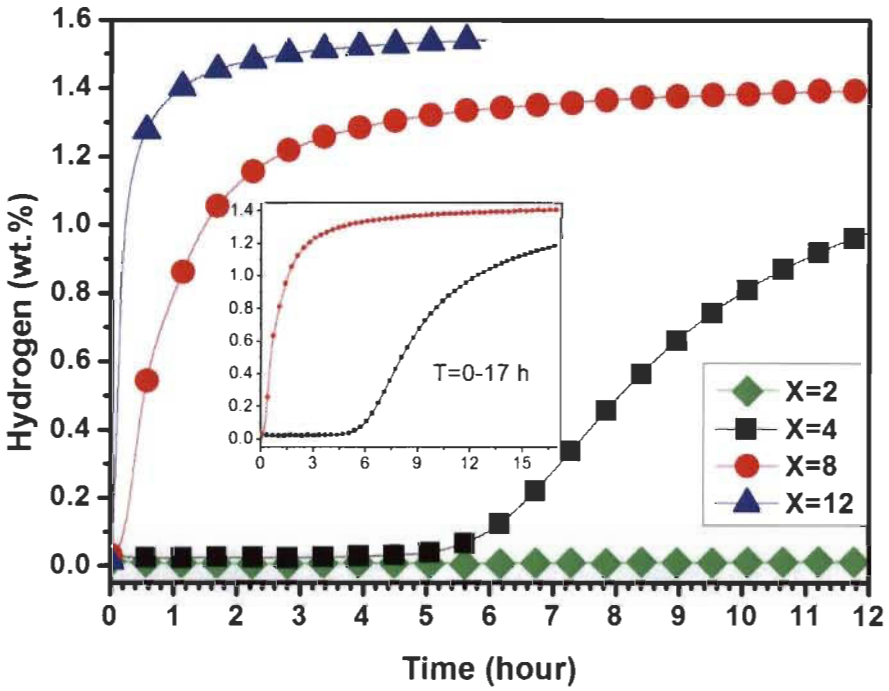

Fig 3.2.7–First hydrogenation of TiFe+x wt.% (Zr+2Mn) (x=2, 4, 8, 12) alloys at room temperature under 3 MPa hydrogen pressure.

3.2.1.4. Pressure-composition isotherms

After the first hydrogenation cycle, the pressure-composition isotherm of the samples (x=4, 8, 12) were measured at room temperature and are shown in Fig 3.2.8. It can be seen clearly that the absorption plateau pressure decreases from x=4 to 12, however the desorption plateau pressure are essentially at the same pressure. This means that adding (Zr+2Mn) does not change the thermodynamics of dehydrogenation but reduced the hysteresis. Also, the reversible capacity seems to increase with increasing x but it is lower than those measured during the first hydrogenation [49].

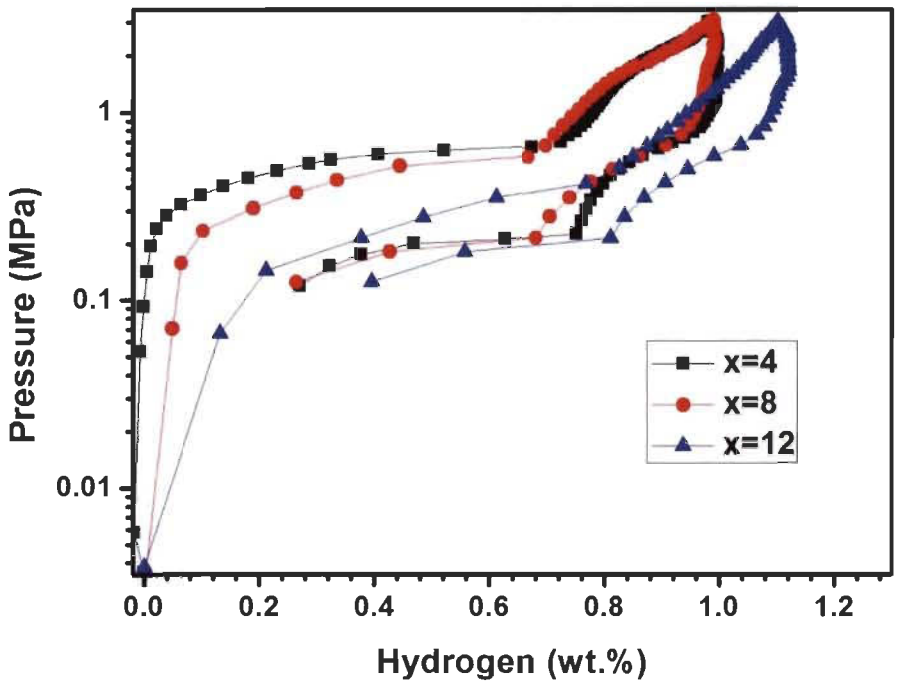

Fig 3.2.8–Pressure-composition isotherms of TiFe+x wt.% (Zr+2Mn) (x= 4, 8, 12) alloys at room temperature. The highest pressure is 3 MPa for the absorption and the lowest pressure is 0.1 MPa for the desorption.

3.2.1.5. Air exposure

The possibility to expose as-cast alloys to the air before first hydrogenation could greatly reduce the synthesis complexity and cost. Therefore, we investigated the effect of air exposure on our as-cast alloys by preparing two identical samples of composition TiFe+12 wt.% (Zr+2Mn). One sample was processed in air, the other one in an argon-filled glove box. The sample labelled Ar was crushed into a glove box and never exposed to the air. Sample labelled Air was crushed and handled in air. The first hydrogenation was measured under an initial hydrogen pressure of 2 MPa at room temperature. Activation curves are shown in Fig 3.2.9. Remarkably, the air exposed sample has the same activation kinetics as the sample handled under argon. These results indicate that the TiFe+12 wt.% (Zr+2Mn) alloy could be handled in air without detrimental effects in the activation behaviour.

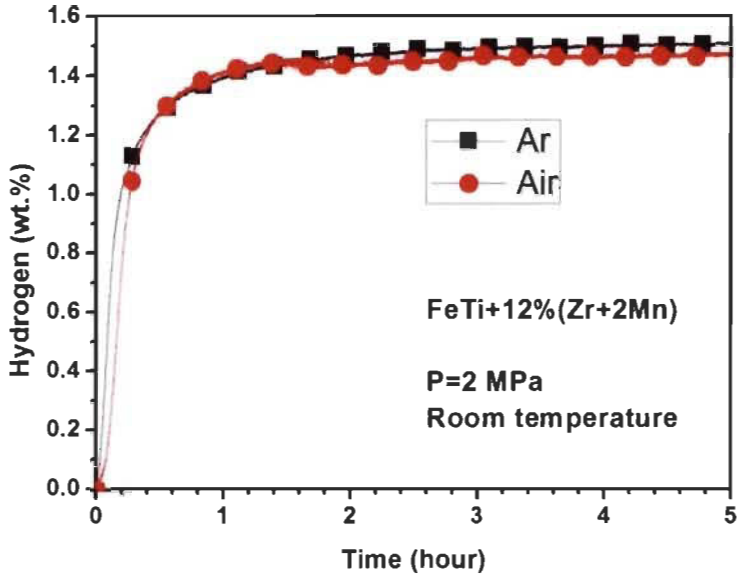

Fig 3.2.9–First hydrogenation of TiFe+12 wt.% (Zr+2Mn) alloys at room temperature under 2 MPa hydrogen pressure.

In order to compare the effect of the air and argon on the reversible capacity of TiFe+12 wt.% (Zr+2Mn) alloy, the pressure composition isotherm at room temperature was measured. Fig 3.2.10 clearly shows that the absorption and desorption plateau pressures are not modified by air exposure. However, the reversible capacity was slightly reduced.

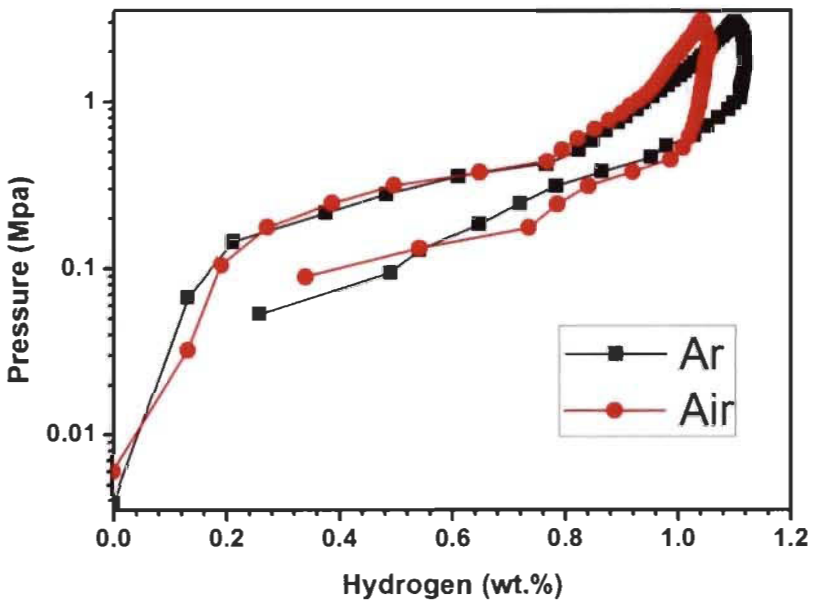

Fig 3.2.10–Pressure-composition isotherms of TiFe+12 wt.% (Zr+2Mn) alloys for a sample handled in air and another one handled in argon protective atmosphere.

3.2.1.6. Improving first hydrogenation kinetics by cold rolling

The first hydrogenation kinetics shown in Fig 3.2.7 indicates that an incubation time is present for x=2 and x=4. In a previous investigation, it was shown that cold rolling is very effective to enhance the first hydrogenation of $LaNi_5$ alloy [45]. This led to the use of cold rolling on the as-cast material to see if there is any first hydrogenation kinetic improvement. Cold rolling was done in air for one and five rolling passes. Fig 3.2.11 shows the first hydrogenation of TiFe+x wt.% (Zr+2Mn) (x=2(a), 4(b), 8(c), 12(d)) alloys in as cast and after cold rolling. For x=8 and x=12 the curves levelled off after two hours. In order to have a better view of the kinetics we only plotted the first two hours. It is seen clearly that cold rolling has a clear beneficial effect only for the x=4 where rolling reduces the incubation time. In the case of x=8 the effect was more limited. Thus cold rolling could reduce incubation time but the main factor to enhance first hydrogenation is by adding (Zr+2Mn) alloy.

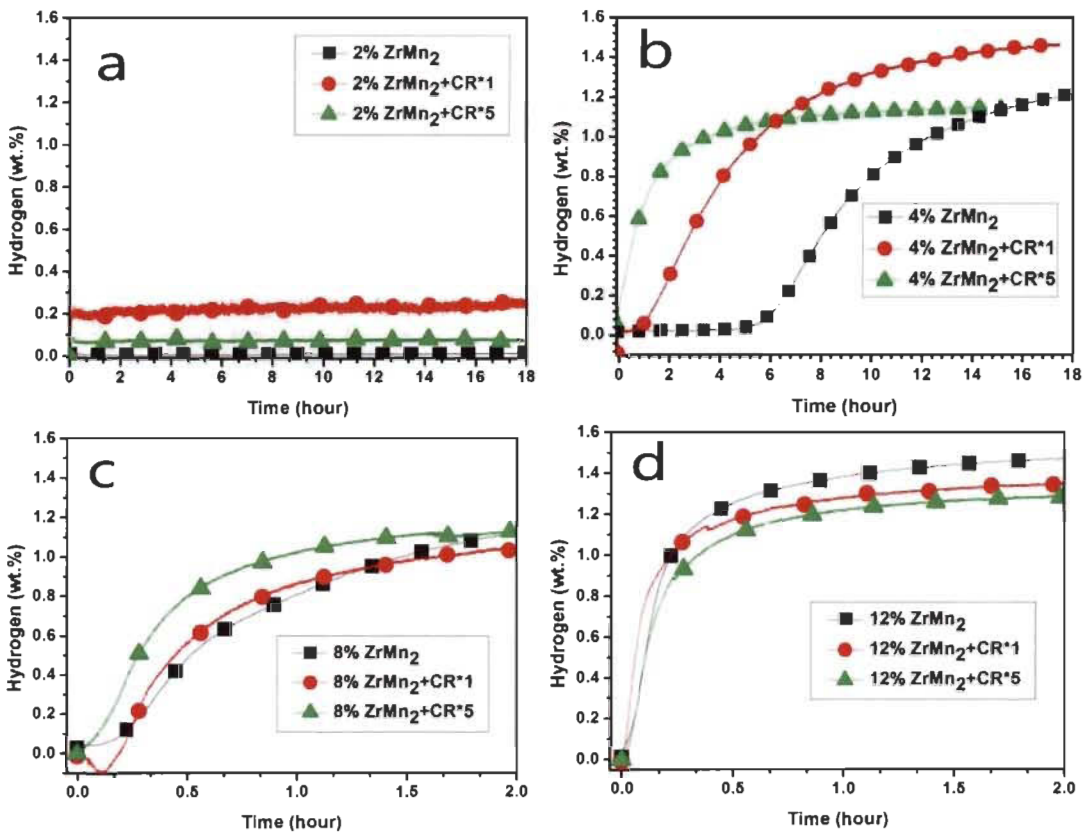

Fig 3.2.11–First hydrogenation of as-cast and cold rolled TiFe+x wt.% (Zr+2Mn) (x=2(a), 4(b), 8(c), 12(d)) alloys. Hydrogenation performed at room temperature under 2 MPa of hydrogen. Hydrogen capacity is given in weight % (hydrogen mass/mass of alloy).

3.2.2. Conclusion

Hydrogenation of TiFe+x wt.% (Zr+2Mn) (x=2, 4, 8, 12) alloys has been investigated. It is found that the as-cast alloys are multiphases with a main phase having the TiFe structure and a zirconium and manganese-rich secondary phase. The amount of secondary phase increases with the amount of (Zr+2Mn) as additive.

The first hydrogenation kinetics and capacities of TiFe+x wt.% (Zr+2Mn) (x=2, 4, 8, 12) alloys increases with the amount of (Zr+2Mn) due to the very fine distribution of the secondary phase. Pressure-composition isotherms also show that increasing x can decrease the absorption plateau pressure. Air exposure was shown to have minimal effect on the hydrogen absorbing properties of TiFe+12 wt.% (Zr+2Mn) alloy. This is important for industrial applications as the need to work under inert atmosphere greatly increase production costs. It is also found that cold rolling has a clear beneficial effect only for the x=4 where rolling reduces the incubation time.

3.3. Microstructure evolution, phase transformation and hydrogenation performance of TiFe alloy doped with x wt.% (Zr+2V)

It was recently reported that the first hydrogenation of TiFe alloy could be improved by adding Zr [49, 71] and V [73]. This indicates that zirconium and vanadium play an important role on improving the first hydrogenation properties of TiFe alloy. The positive effect of zirconium and vanadium leads to the investigation of (Zr+2V) as an additive to TiFe alloy. In this chapter the effects of different (Zr+2V) content on the microstructure, hydrogen storage properties and air resistance of TiFe alloy are reported.

3.3.1. Results and discussion

3.3.1.1. Morphology

Fig 3.3.1 shows backscattered electron micrographs of TiFe+x wt.% (Zr+2V) (x=2, 4, 8, 12) alloys prepared by arc melting. They show different microstructure which includes bright and dark phases. For small amount of (Zr+2V) (x=2), it can be seen that small bright areas increase with incipient dendritic structure. For x=4, the bright areas are larger and the dendritic morphology more apparent. For x=8 the bright areas increase and the dendrites are well developed. When x=12 the bright surface is quite important. Using image J software, the proportion of bright and dark phase areas is measured. These values are plotted in Fig 3.3.2.

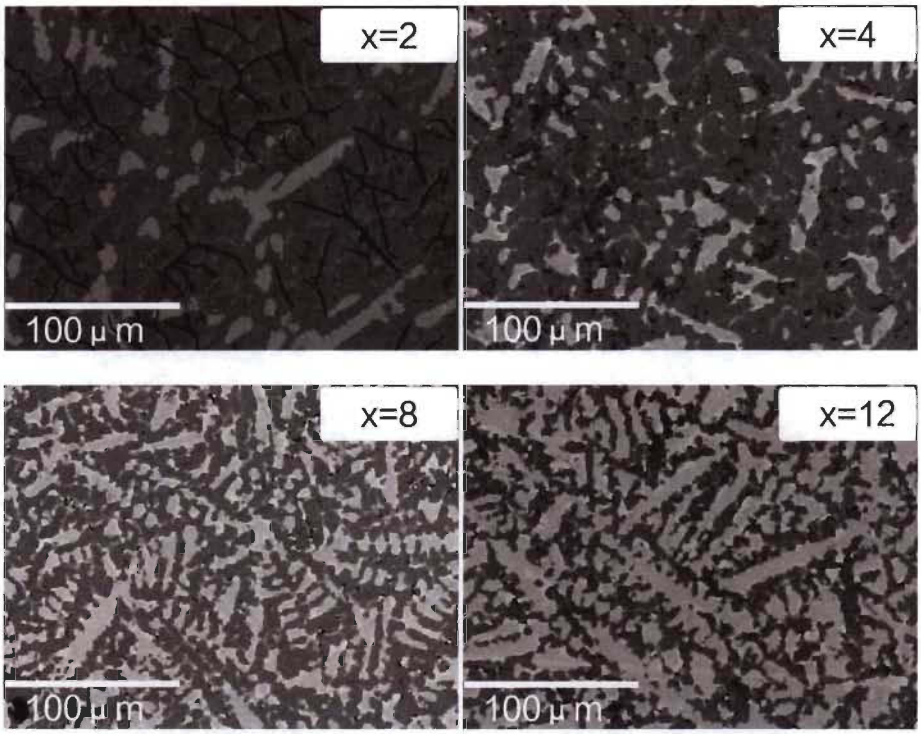

Fig 3.3.1–Backscattered electron micrographs of TiFe+x wt.% (Zr+2V) (x=2, 4, 8, 12) alloys prepared by arc melting.

From Fig 3.3.2 it is seen clearly that the bright phase area increases linearly with x. The fact that the ordinate at the origin is not zero and the slope is not 1 means that the bright phase composition is not pure (Zr+2V) but instead contains Ti and Fe elements. In order to confirm this, the chemical composition of each phase was analyzed by EDX.

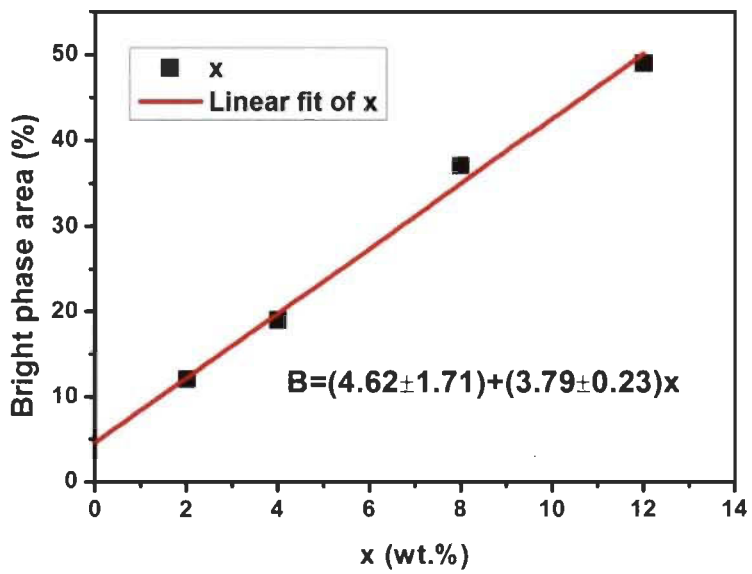

Fig 3.3.2–Relationship between the bright phase area (%) and x (wt.%).

Table 3.3.1 shows the measured bulk atomic composition of each alloy compared to their nominal compositions. It is clear that all alloys have the desired bulk composition.

Table 3.3.1-Nominal bulk and bulk atomic abundance as measured by EDX of TiFe+x wt.% (Zr+2V) (x=2, 4, 8, 12) alloys.

Sample		Ti(Atomic%)	Fe(Atomic%)	Zr(Atomic%)	V(Atomic%)
x=2	Nominal composition	49.2	49.2	0.5	1.0
	Measurement	48.9	49.2	0.7	1.2
x=4	Nominal composition	48.5	48.5	1.0	2.0
	Measurement	48.6	48.2	1.2	2.0
x=8	Nominal composition	47.0	46.6	2.0	4.0
	Measurement	47.5	46.0	2.4	4.1
x=12	Nominal composition	45.8	45.8	2.8	5.6
	Measurement	46.2	44.8	3.4	5.6

Fig 3.3.3 shows a higher magnification backscattered electron micrographs of TiFe+x wt.% (Zr+2V) alloy. A quantitative analysis of the dark phase (point 1) and bright phase (point 2) was performed and the proportions of elements are reported in Table 3.3.2 and 3.3.3, respectively. Analysis of the dark phase (Table 3.3.2) indicates that for x=2, 4, and 8, zirconium is totally absent, the iron abundance is constant while titanium abundance slightly decreases. The decreasing of titanium abundance is due to substitution by vanadium. From the elemental abundances, we could conclude that the

dark phase has a composition Ti_yFeV_{1-y}. However, for x=12 the situation is more complicated. Here, iron abundance is more than 50 atomic % and zirconium is present at a level of 3 atomic %.

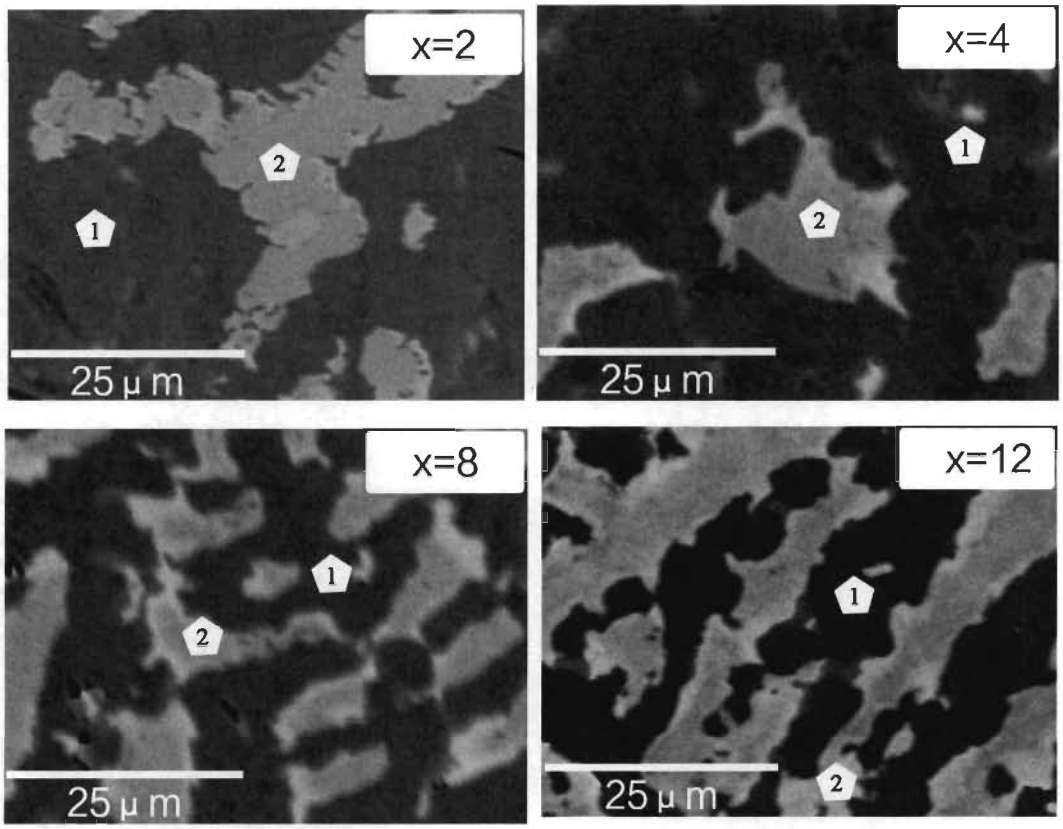

Fig 3.3.3–Backscattered electron micrographs of TiFe+x wt.% (Zr+2V) (x=2, 4, 8 and 12) alloy prepared by arc melting.

Table 3.3.2-Element composition of TiFe+x wt.% (Zr+2V) (x=2, 4, 8, 12) alloys in the dark phase (point 1).

Element (Atomic%)	x=2	x=4	x=8	x=12
Fe	50.0±0.3	49.7±0.3	50.0±0.3	53.7±0.3
Ti	49.4±0.2	48.9±0.2	47.4±0.2	39.2±0.3
V	0.6±0.2	1.4±0.2	2.7±0.2	4.2±0.2
Zr	0.0	0.0	0.0	3.0±0.3

Table 3.3.3-Element composition of TiFe+x wt.% (Zr+2V) (x=2, 4, 8, 12) alloys in the bright phase (point 2).

Element (Atomic%)	x=2	x=4	x=8	x=12
Fe	57.5±0.3	56.4±0.3	52.3±0.3	37.3±0.3
Ti	40.4±0.2	39.5±0.2	40.0±0.2	43.9±0.2
V	1.4±0.1	2.6±0.2	5.0±0.2	9.7±0.2
Zr	0.7±0.2	1.5±0.3	2.7±0.3	9.2±0.3

Inspection of Table 3.3.3 shows that the titanium abundance is constant over the whole range of x values. However, contrary to the dark phase, it is the iron that is substituted by vanadium and zirconium when x increases. In fact the ratio of Zr/V is almost 1/2 which is the ratio of (Zr+2V). It is clear that the chemical composition in the dark and bright phases does not change in the same fashion when x increases.

3.3.1.2. Structure characterization

The XRD patterns of the TiFe+x wt.% (Zr+2V) (x=2, 4, 8, 12) alloys in as-cast state are presented in Fig 3.3.4. It can clearly be seen that all alloys prepared have TiFe phase. However the secondary phase only can be seen for x=8 and 12. Due to the small intensities of these peaks, indexation is difficult. By inspection, these small peaks can match the Fe_2Ti type crystal structure.

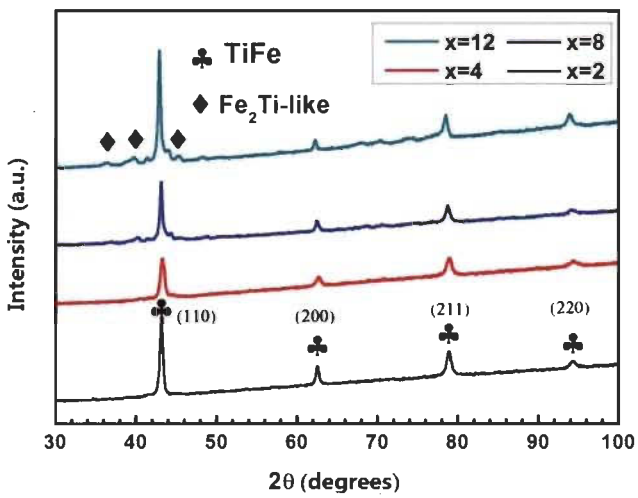

Fig 3.3.4–XRD of TiFe+x wt.% (Zr+2V) (x=2, 4, 8, 12) alloys in as-cast state.

In order to further identify the secondary phase, the synchrotron pattern is shown in Fig 3.3.5. From this figure, it can be seen that TiFe phase is very obvious and shows (100) and (110) lattice plane. In addition, some rings and bright points also can be found at both sides of (110) lattice plane. Actually this suggests the presence of Fe_2Ti-like phase.

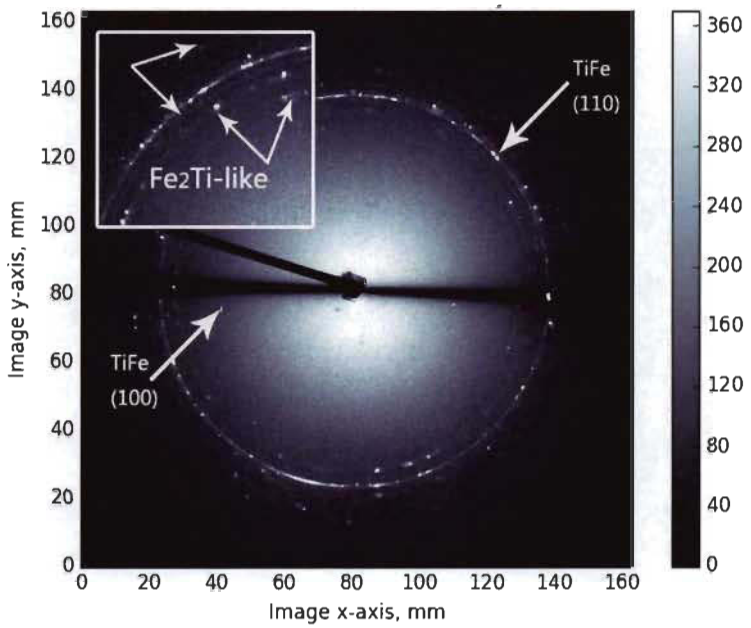

Fig 3.3.5–Synchrotron pattern of TiFe+12 wt.% (Zr+2V) alloy in as-cast state.

Combining XRD and synchrotron, the secondary phase can be speculated Fe_2Ti-like phase. Using Rietveld refinement method, these small peaks could be fitted with a Fe_2Ti phase (Space group: P63/mmc, structure type $MgZn_2$) [74]. This phase was also seen in other Ti-Fe-Zr compounds [75]. Rietveld refinement was performed on all patterns. For the bright phase structure, the chemical composition was fixed as the one determined from EDX measurements. Fig 3.3.6 shows the Rietveld refinement for x=12 alloy. The refinement is good except for a possible small peak at around 41.5°. Despite the smallness of the peaks, the Fe_2Ti-like phase abundance was determined to be 57 wt.% which is very close to the value determined from SEM micrographs. Likewise, the Fe_2Ti-like phase abundance in the x=8 pattern was given by Rietveld refinement to be 39 wt.% which again, is close to the SEM value.

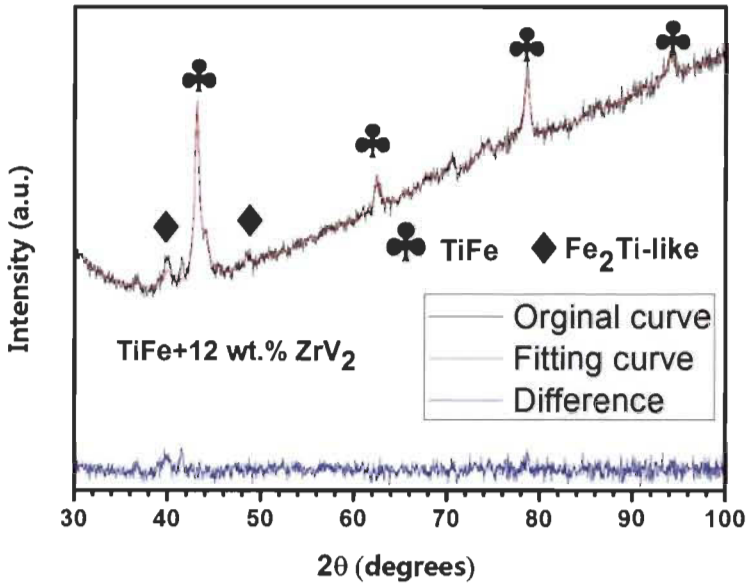

Fig 3.3.6–Refinement results of TiFe+12 wt.% (Zr+2V) alloy by TOPAS software.

Table 3.3.4 shows the lattice parameters *a* and *c* (in Å) and crystallite size (nm) of different phases in as-cast TiFe+x wt.% (Zr+2V) (x=2, 4, 8, 12) alloys as determined by Rietveld analysis. It can be seen that the lattice parameters of TiFe increases with x due to the replacement of big radius zirconium.

Table 3.3.4-Lattice parameters *a* and *c* (in Å) and crystallite size (nm) of different phases in as cast TiFe+x wt.% (Zr+2V) (x=2, 4, 8, 12) alloys as determined by Rietveld analysis.The number in parenthesis is error.

Phase	Parameters	x=2	x=4	x=8	x=12
TiFe	*a*	2.9787(2)	2.9794(4)	2.9815(3)	2.9863(7)
	Crystallite size	19.3(2)	13.5(2)	23.1(4)	13.8(5)
Fe_2Ti-like	*a*			4.911(2)	4.939(3)
	c			7.995(6)	8.030(7)
	Crystallite size			9.0(5)	7.6(5)

Table 3.3.5 shows the mean atomic radius (in Å) of TiFe+x wt.% (Zr+2V) (x=2, 4, 8, 12) alloys in as-cast state. From this table, it can be seen that the mean atomic radius increases with the content of (Zr+2V). This result also agrees with the change of lattice parameter in Table 3.3.4. In fact, the mean radius increased much more than the lattice parameter. The reason is that the atoms are substituting on specific sites.

Table 3.3.5–Mean atomic radius (in Å) of TiFe+x wt.% (Zr+2V) (x=2, 4, 8, 12) alloys in as-cast state.

Element (Atomic%)	x=2	x=4	x=8	x=12
Mean atomic radius	1.35694	1.36232	1.36671	1.36886

3.3.1.3. First hydrogenation

Fig 3.3.7 shows the first hydrogenation of TiFe + x wt.% (Zr+2V) (x=2, 4, 8, 12) alloys measured under an initial hydrogen pressure of 2 MPa at room temperature. It can be seen that x=2 can't absorb any hydrogen even after 25 h. There is around 4.5 h of incubation time for x=4. For x=8 and 12, the alloys show no incubation time and directly absorb hydrogen with fast kinetics. Also, the first hydrogen absorption capacity increases with x and the maximum capacity is around 1.65 wt.% (x=12).

As seen from the SEM investigation and powder diffraction patterns, amount of bright phase increases with x. Therefore, the conclusion is that enhancement of first hydrogenation kinetic is proportional to the amount of bright phase. Furthermore, taking into account that the hydrogen capacity of pure TiFe is 1.86 wt.% and that, for x=12, the amount of TiFe phase is around 50% as determined by SEM and Rietveld refinement, this phase could only contribute to less than 1 wt.% to the hydrogen capacity. This means that the secondary phase Fe_2Ti-like also absorbs hydrogen with a capacity similar to the TiFe phase. Moreover, there is not any change of slope or kink in the absorption curve for x=8 and 12. This means that the dark and bright phases are acting as a single phase during hydrogenation. A possible mechanism

could be that the bright phase acts as a gateway for the hydrogen. Such mechanism was also proposed for a closely related system (Ti-Fe-Zr) [49, 70, 71, 76].

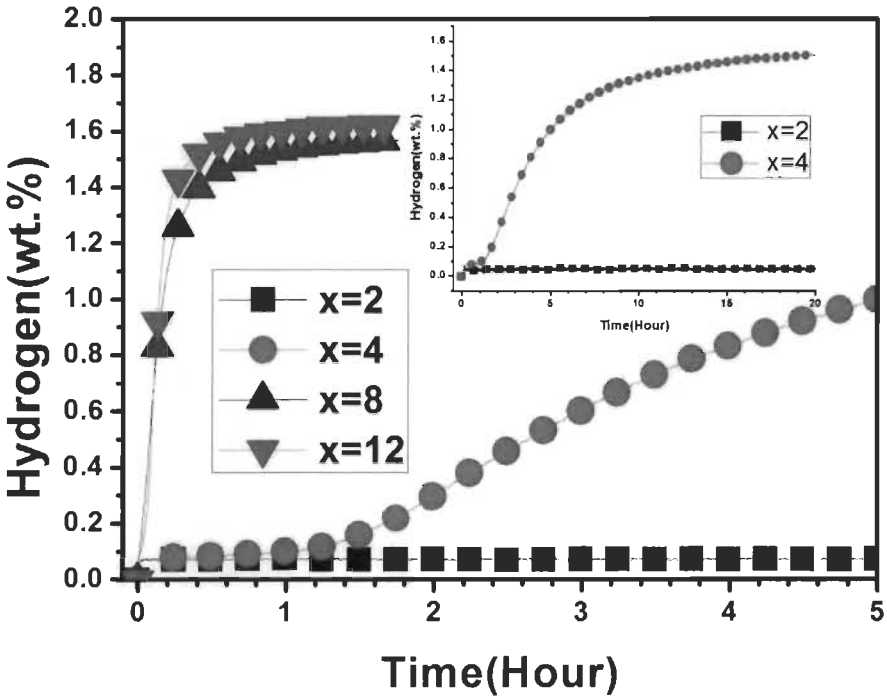

Fig 3.3.7–First hydrogenation kinetics of TiFe+x wt.% (Zr+2V) (x=2, 4, 8, 12) alloys at room temperature under 2 MPa hydrogen pressure.

The curves of first and second hydrogenation of TiFe+12 wt.% (Zr+2V) alloy are compared in Fig 3.3.8. It can be seen clearly that there is an obvious reduction of the capacity in the second hydrogenation. The maximum capacity of second hydrogenation is 0.8 wt.% and the lost capacity is around 0.85 wt.%. In fact it can be found that the amount of TiFe phase is 43% as determined by Rietveld refinement in Fig 3.3.6. In addition the hydrogen capacity of TiFe is 1.86 wt.%. So the contribution of TiFe phase to the total hydrogen capacity is around 0.80 wt.% which agrees with the maximum capacity in the second hydrogenation. This result also proves that the TiFe phase actually acts as the role of reversible absorption and desorption. Further, it can be calculated that the contribution of Fe_2Ti-like phase to the total hydrogen capacity is around 0.85 wt.% (1.65 wt.%-0.80 wt.%). Then the hydrogen capacity of Fe_2Ti-like phase is 1.49 wt.% (0.85 wt% / 0.57).

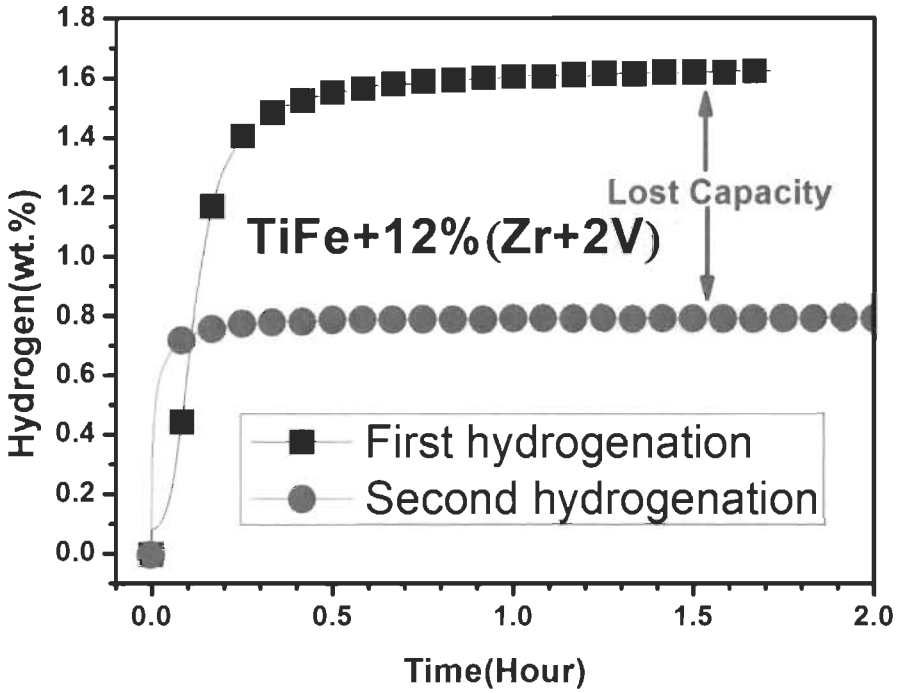

Fig 3.3.8–First and second hydrogenation of TiFe+12 wt.% (Zr+2V) alloy at room temperature under 2 MPa hydrogen pressure.

In order to know the mechanism of the first hydrogenation kinetics, the experimental data of different first hydrogenation curves was analyzed by using the rate limiting step model equation (Nucleation-growth-impingement model (JMA) [16-18], Contracting volume model (CV) [19-21] and Ginstling-Brounshtein model (GB) [22, 23]) are reported in Table 1.3. The left side of the equation is a function of the reaction's completion ratio (α). In these equations, α is the reaction rate ($\alpha = \%H_{abs}/\%H_{max}$), t is reaction time; k is kinetic rate constant. In order to find the correct rate limiting step, the left side of these equations as a function of time is plotted. For this type of plot, the correct rate limiting step will be a linear curve fitted by Origin software. The model with the best fit to the data represents the reaction's rate limiting step.

Fig 3.3.9 shows the plot for the first hydrogenation kinetics of representative x=4 alloy. Linear regressions were performed on each model. As shown in the literature, in order to get a wider range of the reaction fitted and the regressions from 10% to 90% of the reaction's completion (a = 0.1~0.9) are chosen [24]. It can be seen that CV3D,

GB2D and GB3D all show a reasonable fit for x=4 alloy. In order to compare this three models clearly, the adjusted R^2 value for each alloy was shown in Table 3.3.6. It is clear that the adjusted R^2 value of GB3D model shows the maximum value which is closest to 1. So GB3D is the best model for x=4 alloy. From the description of the GB3D model in Table 1.3, it is 3D growth and the growth interface velocity of diffusion decreases with time [77]. For x=8 and 12 alloys GB3D model also gives the best fit (figures are not plotted here), it can be concluded that the first hydrogenation kinetics of three alloys are in accordance with GB3D model.

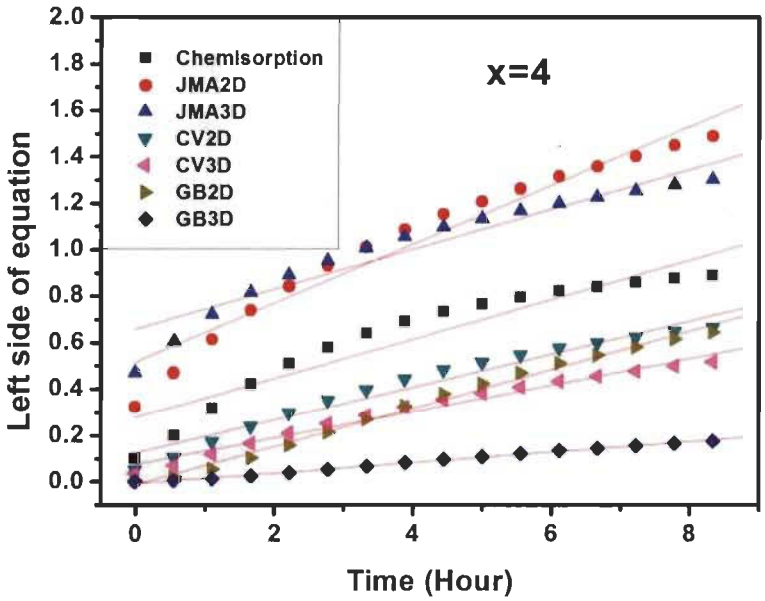

Fig 3.3.9–Representative rate limiting step curves of first hydrogenation of TiFe+4 wt.% (Zr+2V) alloy at room temperature under 2 Mpa hydrogen pressure.

Table 3.3.6–Adjusted R^2 values for all model equations of x=4 sample

Sample	Model	R^2
x=4	Chemisorption	0.89453
	JMA2D	0.95526
	JMA3D	0.92806
	CV2D	0.96051
	CV3D	0.97644
	GB2D	0.99115
	GB3D	0.99570

3.3.1.4. Phase transformation

Fig 3.3.10 shows the synchrotron radiation diffraction pattern of hydrogenated TiFe+12 wt.% (Zr+2V) alloy. It can be seen clearly that $FeTiH_2$ type crystal structure is formed. In previous investigations, it was found that pure TiFe reacting with hydrogen can result in the formation of three kinds of hydrides which include α-phase $FeTiH_x$ ($x<0.06$), β-phase $FeTiH_x$ ($x=1.04$) and γ-phase $FeTiH_x$ ($x=1.93\sim2$) [78-80].

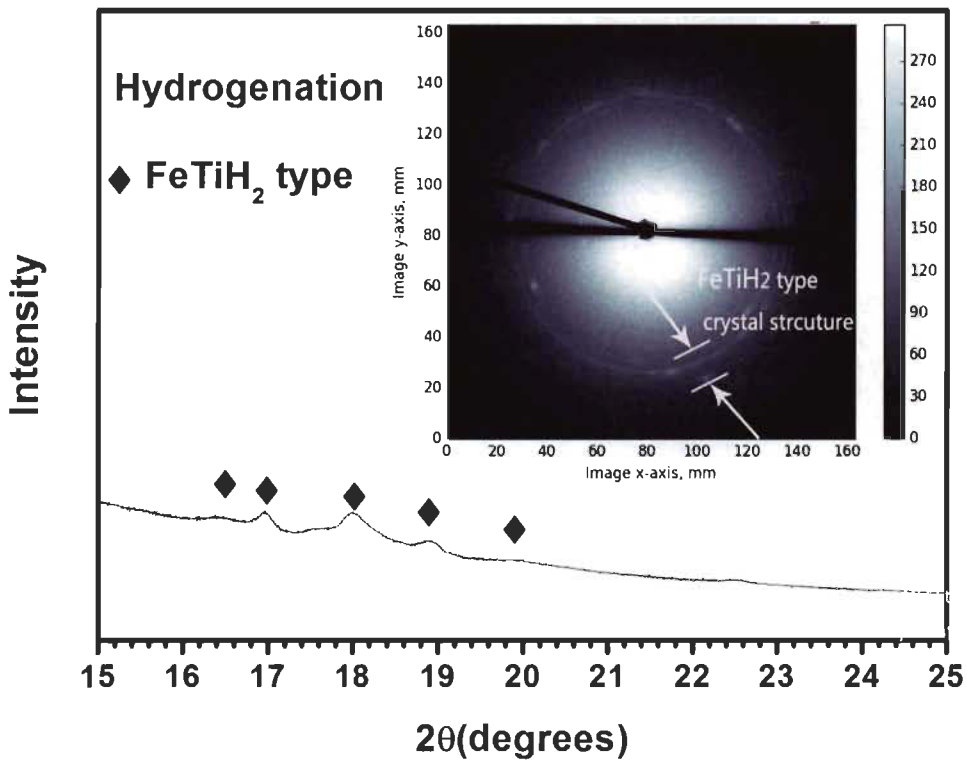

Fig 3.3.10–Synchrotron radiation diffraction pattern of hydrogenated TiFe+12 wt.% (Zr+2V) alloy.

Fig 3.3.11 shows the refinement results for synchrotron radiation diffraction pattern of hydrogenated TiFe+12 wt.% (Zr+2V) alloy using TOPAS software. Actually it can be found that the best refinement is with two different hydrides: namely first hydride ($FeTiH_2$) with space group: Cmmm (65) and orthorhombic crystal system [81] and second hydride with space group: P2/m (10) and monoclinic crystal system. Table 3.3.7 shows the lattice parameters *a*, *b* and *c* (in Å) of these two hydride phases.

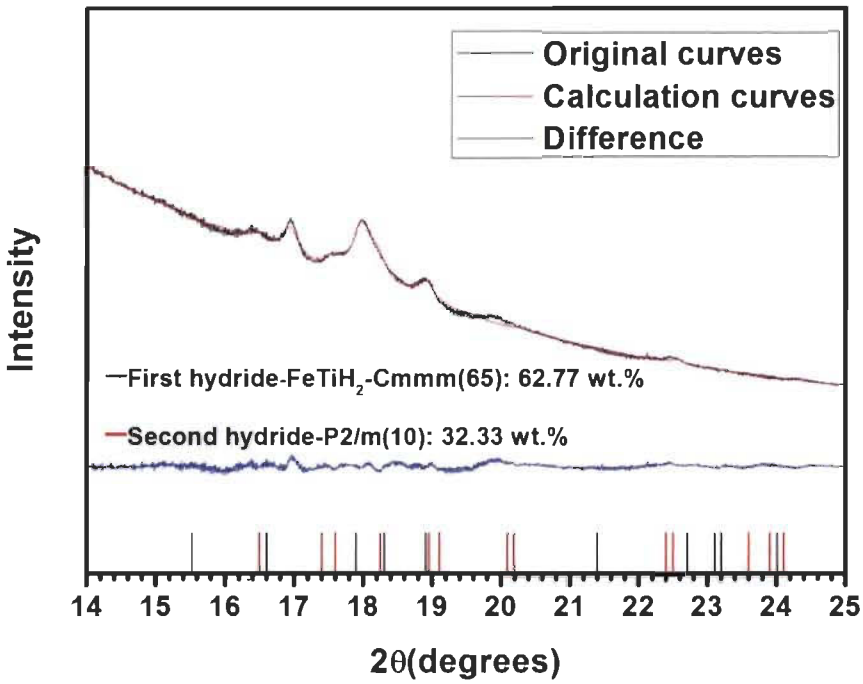

Fig 3.3.11–Refinement results for synchrotron radiation diffraction pattern of hydrogenated TiFe+12 wt.% (Zr+2V) alloy.

Table 3.3.7-Lattice parameters *a*, *b* and *c* (in Å) of different phases in hydrogenated TiFe+12 wt.% (Zr+2V) by Rietveld analysis. The number in parenthesis is error.

Phase	Parameters	x=12
$FeTiH_2$ (Cmmm)	*a*	6.633(7)
	b	6.842(9)
	c	2.974(4)
Second hydride (P2/m)	*a*	4.938(6)
	b	2.882(3)
	c	4.624(5)

The coexistence of two different hydrides is surprising. A possible explanation may be that, upon hydrogenation, the secondary phase experience a decomposition from a Fe_2Ti-type phase to the second hydride phase with space group P2/m. Some evidences of this could be seen in the dehydrogenated pattern shown in Fig 3.3.12. It can be clearly seen that there are two phases: TiFe main phase and second hydride with space group: P2/m. This pattern indicates that the $FeTiH_2$ phase with space group Cmmm

dehydrogenates to give TiFe phase while the second hydride (space group: P2/m), stays hydride. This could also explain the loss of capacity after one cycle of hydrogenation/dehydrogenation. Further investigation is needed in order to confirm this hypothesis.

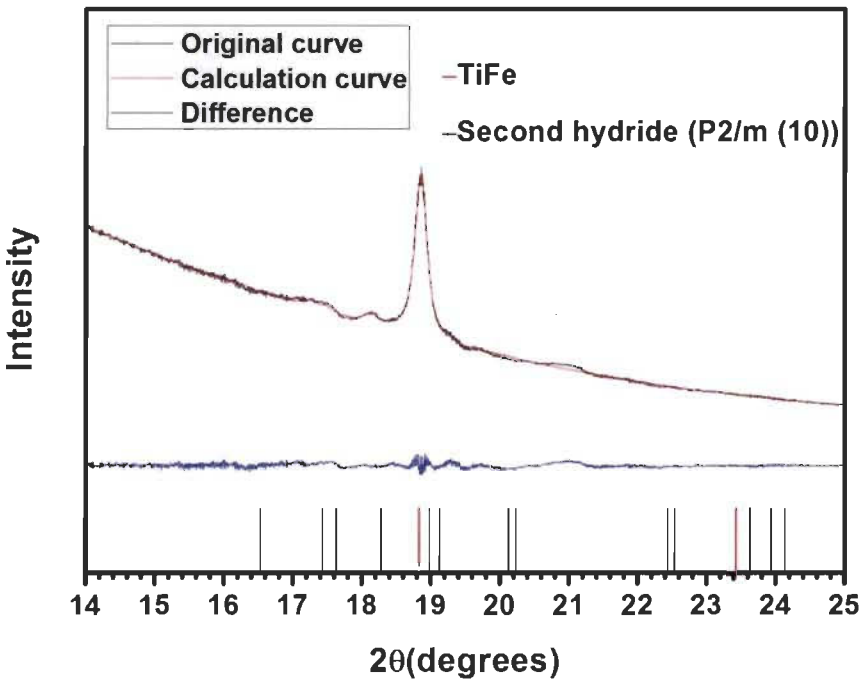

Fig 3.3.12–Refinement results for synchrotron pattern of TiFe+12 wt.% (Zr+2V) alloy for dehydrogenation by TOPAS software.

3.3.1.5. Pressure-composition isotherms

After the first hydrogenation cycle, the pressure-composition isotherm of the samples (x=4, 8, 12) were measured at room temperature in Fig 3.3.13. Prior to the measurement, the samples were kept under vacuum for 1 h at room temperature. It can be seen clearly that the reversible capacity decreases with x. This displays opposite tend compared to the first hydrogenation kinetics curves. Also, the reversible capacity seems to be lower than those measured during the first hydrogenation. A possible reason for the lower reversible capacities might form stable hydrides which can't dehydrogenate after the first hydrogenation [49]. Moreover it can be found that the absorption and desorption plateau pressure decreases from x=4 to x=12. This means that adding (Zr+2V) obviously change the thermodynamics of dehydrogenation.

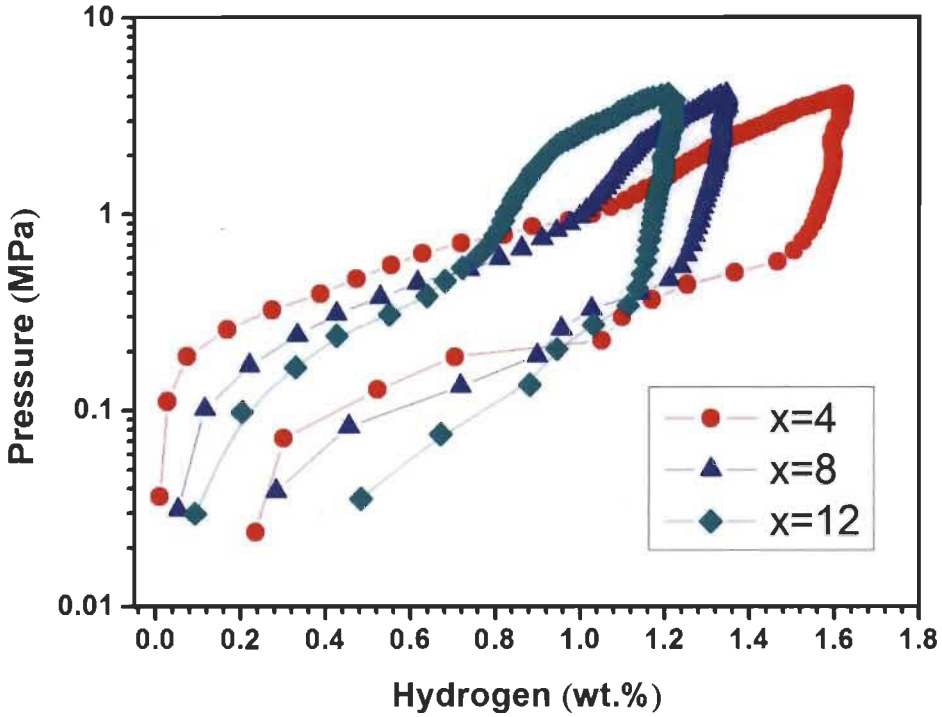

Fig 3.3.13–Pressure-composition isotherm of TiFe+x wt.% (Zr+2V) (x=2, 4, 8, 12) alloys at room temperature.

3.3.1.6. Cycling properties

Fig 3.3.14 shows that the cycling hydrogenation curves of TiFe+12 wt.% (Zr+2V) alloy. It can be seen that the maximum capacity will be cut in half after the first hydrogenation. From the second to fifth hydrogenation, the maximum capacity slightly decreased, but they showed the faster hydrogenation kinetics than the first hydrogenation. As for the reason of the loss of capacity, it has been discussed in 3.3.1.4 section. In this part the rate limiting step of cycling hydrogenation will be studied.

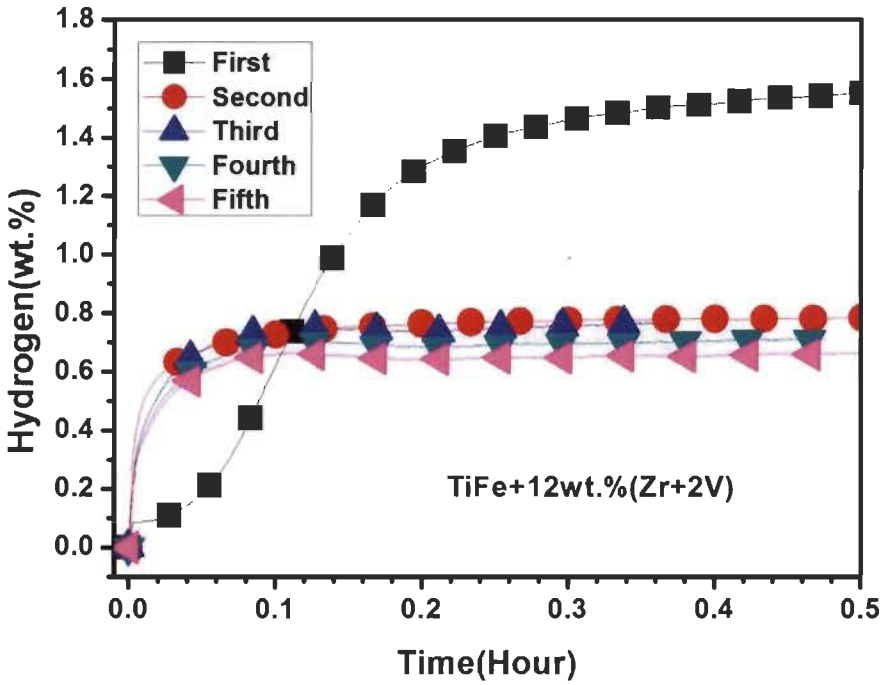

Fig 3.3.14–Cycling hydrogenation of TiFe+12 wt.% (Zr+2V) alloy at room temperature under 2 MPa hydrogen pressure.

According to Table 1.3, the representative rate limiting step of fifth hydrogenation of TiFe+12 wt.% (Zr+2V) alloy is shown in Fig 3.3.15. It can be seen clearly that CV3D, GB2D and GB3D model show a good fit. In order to compare these three models, the adjusted R^2 values of all models are presented in Table 3.3.8. It is easy to see that GB3D presents the R^2 value closest to 1. This means that the kinetic model of fifth hydrogenation of TiFe+12 wt.% (Zr+2V) alloy is also GB3D model. Fig 3.3.16 shows GB3D fitting curves for different hydrogenation cycles. Cycle 2 does not fit as well as cycle 1 but for cycles 3, 4 and 5 we see that the fit is very good. These results indicate that the cycling hydrogenation will not cause the change of kinetic model, even if the maximum capacity reduces with cycle number.

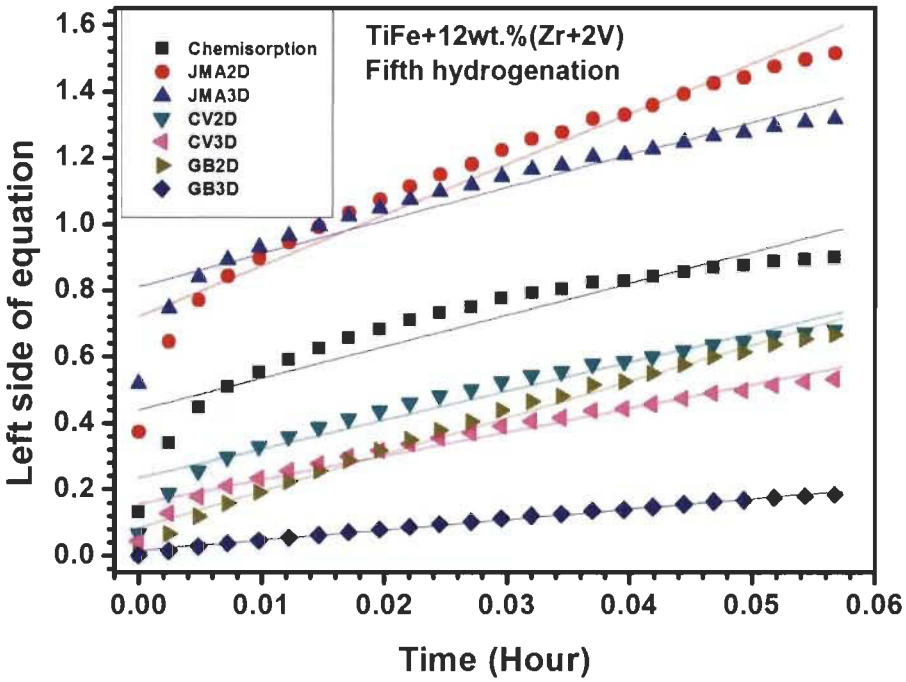

Fig 3.3.15–Representative rate limiting step curves of fifth hydrogenation of TiFe+12 wt.% (Zr+2V) alloy.

Table 3.3.8–Adjusted R^2 values for all model equations of fifth hydrogenation cycle

Sample	Model	R^2
Fifth hydrogenation	Chemisorption	0.85774
	JMA2D	0.94113
	JMA3D	0.91282
	CV2D	0.94164
	CV3D	0.96192
	GB2D	0.98275
	GB3D	0.99221

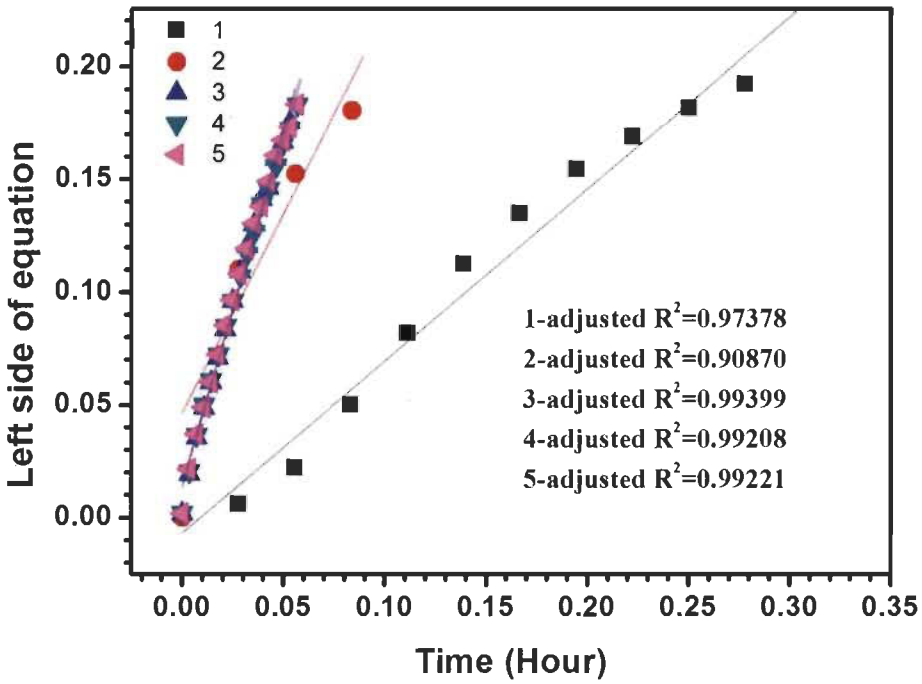

Fig 3.3.16–GB3D fitting curves for different hydrogenation cycles of TiFe+12 wt.% (Zr+2V) alloy.

3.3.1.7. Air exposure

According to Fig 3.3.7, x=12 alloy shows the best first hydrogenation in argon atmosphere. Based on this fact, the x=12 alloy was chosen to investigate the air exposure effect on TiFe+12 wt.% (Zr+2V) alloy. The x=12 alloy was exposed to air for 0.1, 2 and 5 h. The first hydrogenation of TiFe+12 wt.% (Zr+2V) alloy was measured under an initial hydrogen pressure of 2 MPa at room temperature in Fig 3.3.17. It is clearly seen that time=0.1 h alloy does not need the incubation time and absorbs hydrogen. For air exposure time=2 and 5 h the incubation time increases from around 1 to 6.5 h. This means that a long time air exposure can result in a long incubation time. However, compared to pure TiFe alloy, TiFe+12 wt.% (Zr+2V) alloy exhibits an excellent air resistance ability. The above results indicate that TiFe+12 wt.% (Zr+2V) alloy is a good potential material to work in the air for Ti-Fe-Zr system.

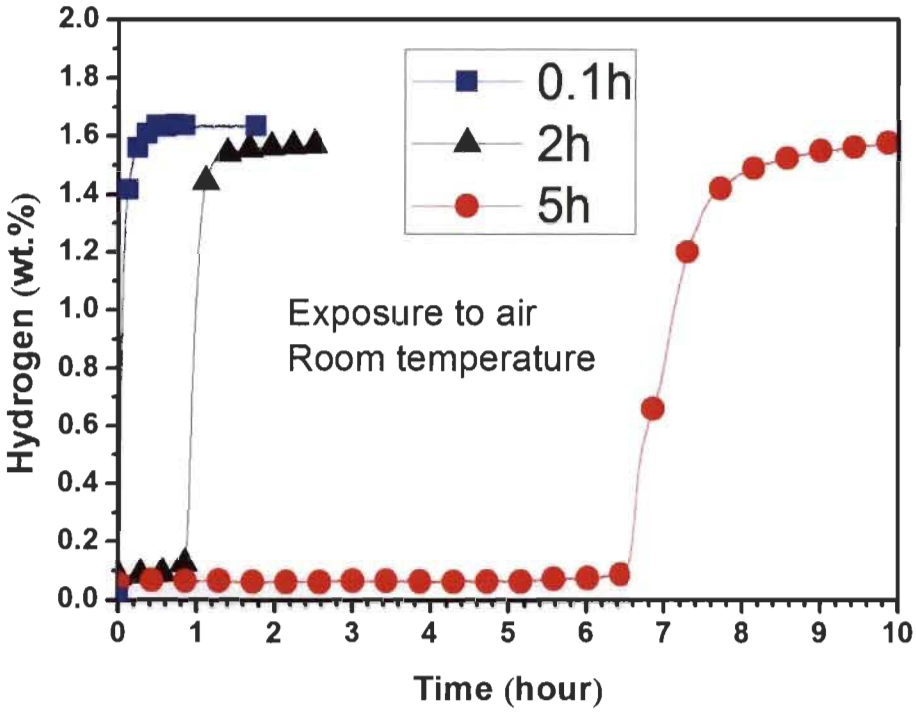

Fig 3.3.17–First hydrogenation kinetics of TiFe+12 wt.% (Zr+2V) alloy handled in air for different time at room temperature.

In order to study the effect of air exposure on the kinetic mechanism of the first hydrogenation, the experimental data of first hydrogenation curves of representative TiFe+12 wt.% (Zr+2V) alloy exposed to air for 0.1 h was analyzed by using the rate limiting step model equation from Table 1.3 in Fig 3.3.18. Actually GB3D model shows the best fit for 0.1 h sample as indicated by the adjusted R^2 values in Table 3.3.9. This means that air exposure won't change the main mechanism of hydrogen absorption. Fig 3.3.19 shows the fitting curves of GB3D models for different air exposure time. For time=2 and 5 h samples, the kinetic model of both samples also agrees with GB3D model. However, the fit for 5 hours is not as good as for the other air expositions. This may means that prolonged air exposure could result in a change of the rate limiting step. Further investigation is needed to clarify this point.

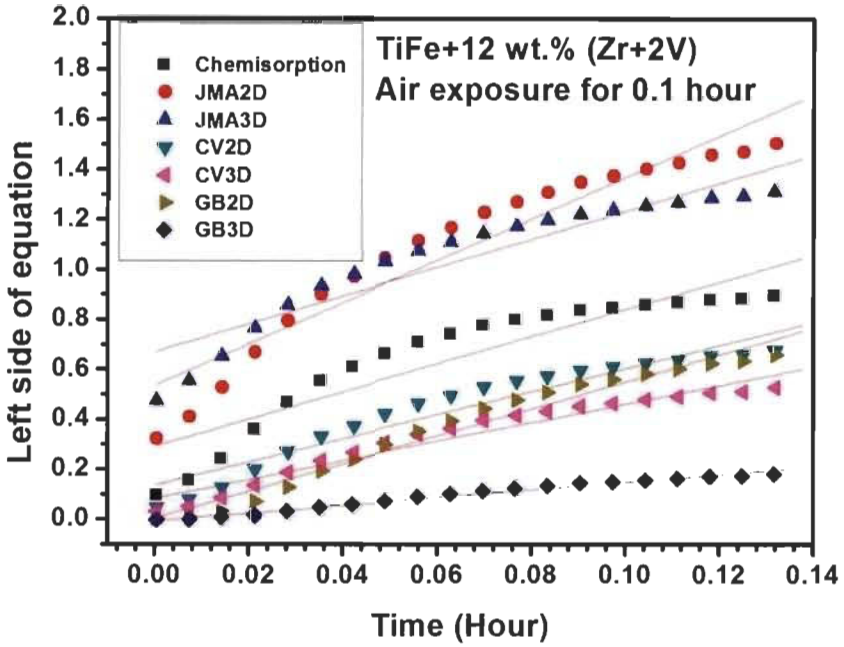

Fig 3.3.18–Representative rate limiting step curves of first hydrogenation of TiFe+12 wt.% (Zr+2V) alloy (exposure to air for 0.1 h).

Table 3.3.9–Adjusted R^2 values for all model equations of 0.1h exposed sample

Sample	Model	R^2
0.1h	Chemisorption	0.84104
	JMA2D	0.91693
	JMA3D	0.88405
	CV2D	0.92137
	CV3D	0.94359
	GB2D	0.96761
	GB3D	0.97886

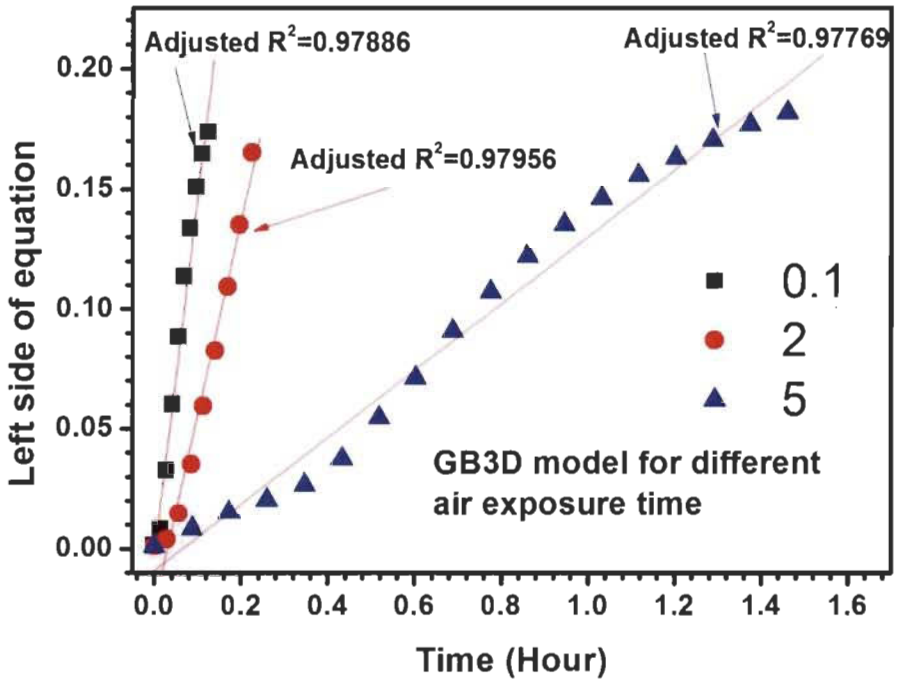

Fig 3.3.19–Fitting curves of all GB3D models for different exposure time (exposure to air for 0.1, 2 and 5 h).

In order to compare the effects of different exposing time on the reversible capacity of TiFe+12 wt.% (Zr+2V) alloy, the pressure-composition isotherm was measured at room temperature and is shown in Fig 3.3.20. It can be found that the absorption plateau pressure were similar for exposure time of 0.1, 2 and 5 h. Also, 0.1 h curve shows the highest reversible capacity among three different exposure times. It suggests that the longer exposing time has a negative effect on reversible capacity. This may be due to the oxide layer forming on the surface of samples.

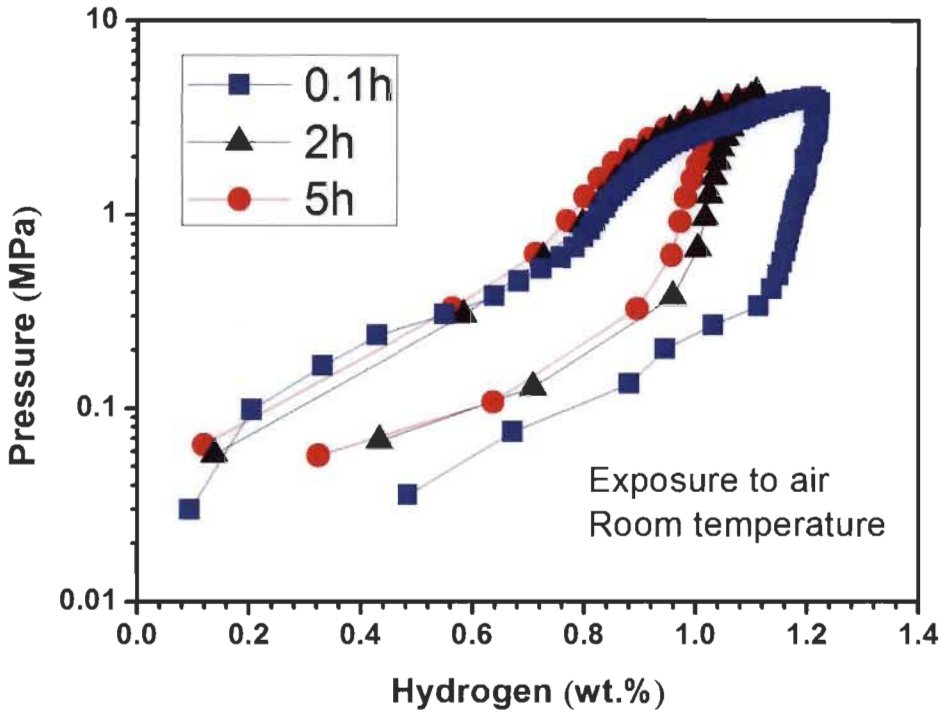

Fig 3.3.20–Pressure-composition isotherm of TiFe+12 wt.% (Zr+2V) alloys at room temperature for different exposure time.

3.3.2. Conclusion

The hydrogen storage properties and microstructure of TiFe+x wt.% (Zr+2V) (x=2, 4, 8, 12) alloys have been investigated. It was found that the as-cast alloys are multiphases with a main phase having the TiFe structure and a zirconium and vanadium-rich secondary phase. The amount of secondary phase increases linearly with the amount of (Zr+2V) as additive.

(1) After the hydrogenation of the TiFe+12 wt.% (Zr+2V) alloy, there are two kinds of hydride phases: first hydride $FeTiH_2$ (space group: Cmmm (65) and orthorhombic crystal system) and second hydride (space group: P2/m (10) and monoclinic crystal system). After dehydrogenation the second hydride phase (space group: P2/m) and TiFe phase are present.

(2) The first hydrogenation kinetics and capacities of TiFe+x wt.% (Zr+2V) (x=2, 4, 8, 12) alloys increases with the amount of (Zr+2V). In addition, the first hydrogenation kinetics of three alloys is in accordance with GB3D model.

(3) From cycling properties it can be found that the loss capacity is around 0.85 wt.% after first hydrogenation. Moreover, the cycling hydrogenation will not cause the

change of kinetic model, even if the maximum capacity slightly reduces with cycle number.

(4) The reversible capacity decreases with the amount of (Zr+2V). In addition when we expose TiFe+12 wt.% (Zr+2V) alloy in air, air exposure will have minimal effect on the hydrogen absorbing properties, first hydrogenation kinetic mechanism and reversible capacity.

4. Effect of mechanical deformation on the microstructure and first hydrogenation kinetics of TiFe-based alloy

4.1. Effect of ball milling on the first hydrogenation properties of TiFe alloy doped with 4 wt.% Zr as additive

Recently, Gosselin et al found that TiFe alloy doped with 4 wt.% zirconium by arc melting can make the first hydrogenation of TiFe alloy occur at room temperature and under 4.5 MPa hydrogen pressure. However the first hydrogenation kinetics is still too slow [70]. It is well known that the presence of defects and nanocrystallinity could improve reaction kinetics and reduce incubation time. Moreover it is well known that ball milling is a fast and efficient way to reduce crystallite size and induce defects in materials. Therefore, the effect of ball milling on the microstructure and hydrogenation properties of TiFe alloy with 4 wt.% zirconium as additive was investigated.

4.1.1. Results and discussion

4.1.1.1. Chemical composition

Fig 4.1.1 shows the measured atomic abundance of TiFe doped with 4 wt.% Zr alloy in the as-cast state. The chemical composition also can be seen in this figure, and prove that the atomic abundances of all elements in as-cast state are very close to the nominal composition (Ti=48.8 at.%, Fe=48.8 at.% and Zr=2.4 at.%).

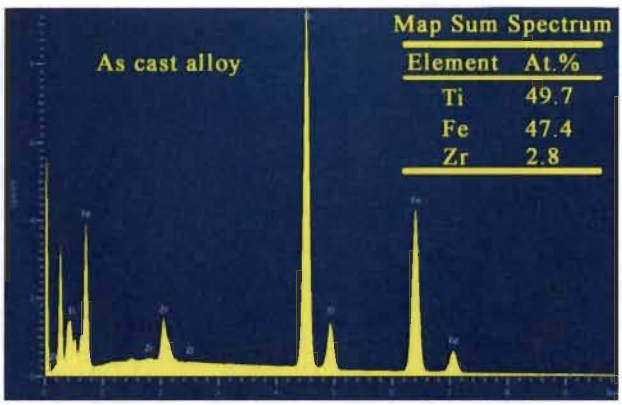

Fig 4.1.1-Measured atomic abundance of TiFe+4 wt.% Zr alloys in as-cast state.

4.1.1.2. Morphology

Fig 4.1.2 shows the SEM micrographs of TiFe doped with 4 wt.% Zr in as cast and different ball milling time (5, 15, 30 and 60 min). First, it can be seen clearly that the as-cast particles have sharp edges due to the mortar and pestle used to obtain powder. After only 5 minutes of milling the particles are much smaller and they have round edges. Further milling mainly produces important agglomerations of smaller particle.

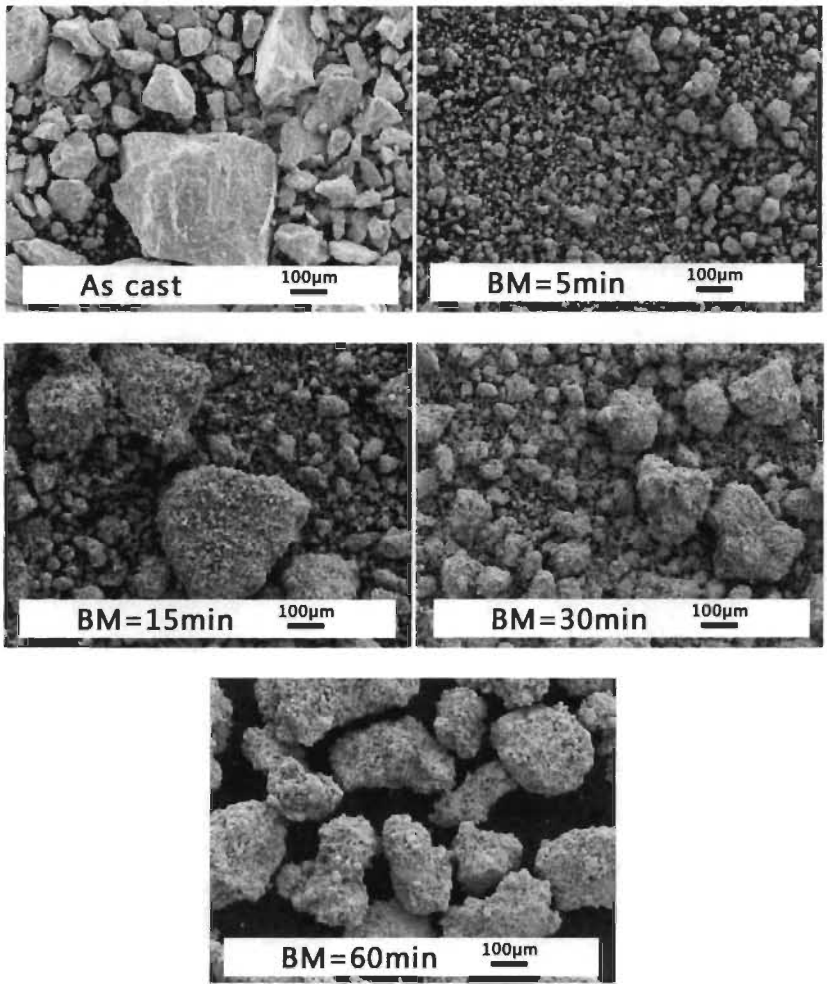

Fig 4.1.2–SEM micrographs of TiFe+4 wt.% Zr alloy taken in 100 magnification for as cast and different ball milling time (5, 15, 30 and 60 min).

Fig 4.1.3 presents the micrographs of TiFe doped with 4 wt.% Zr before and after hydrogenation. Comparing absorption and desorption of as-cast alloy, it can be found that some obvious cracks in the hydrogenated sample (b) due to the volume increase upon hydrogenation. For ball milled samples, it can't be seen obvious changes.

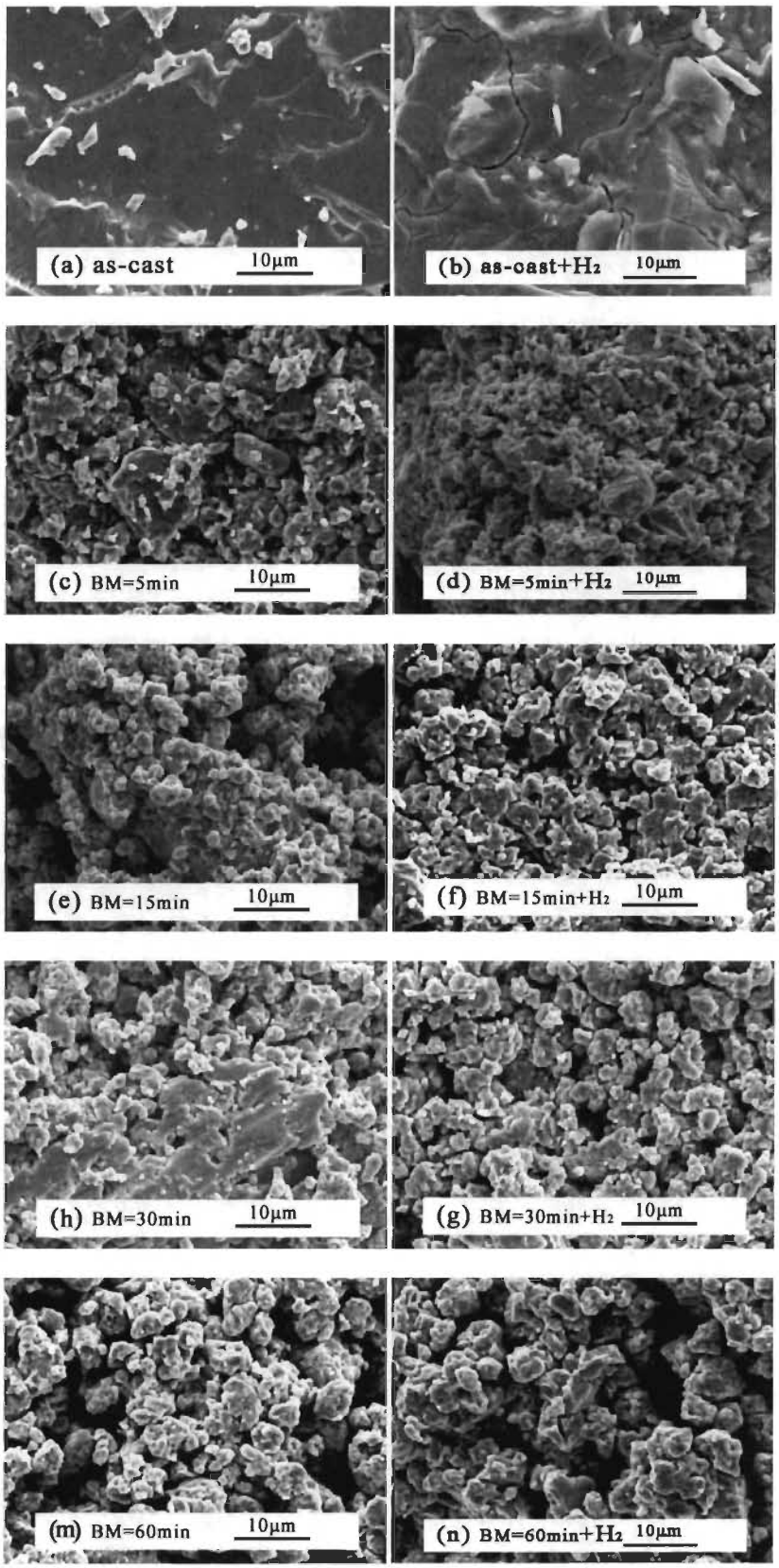

Fig 4.1.3–SEM micrographs of TiFe+4 wt.% Zr alloy taken in 2500 magnification for as cast and different ball milling time (5, 15, 30 and 60 min) before and after hydrogenation.

4.1.1.3. Crystal structure characterization

The XRD patterns of TiFe doped with 4 wt.% Zr alloy for ball-milled samples are presented in Fig 4.1.4. It can be clearly seen that the TiFe Bragg peaks in the patterns of the ball-milled samples are getting broader with milling time. This is an indication of reduction of crystallite size due to ball milling. This could be seen in Table 4.1.1. The small peaks are at around 38~40° in as cast sample are most likely due to the secondary phase. They could no longer be seen in the patterns of ball milled samples because their broadening made them undistinguishable from the background. By inspection, these small peaks match the crystal structure of Fe_2Ti-like ($MgZn_2$ type) [74]. The Ti-Fe phase diagram confirms the possibility of appearance of that phase and the inclusion of zirconium into that phase is possible [71].

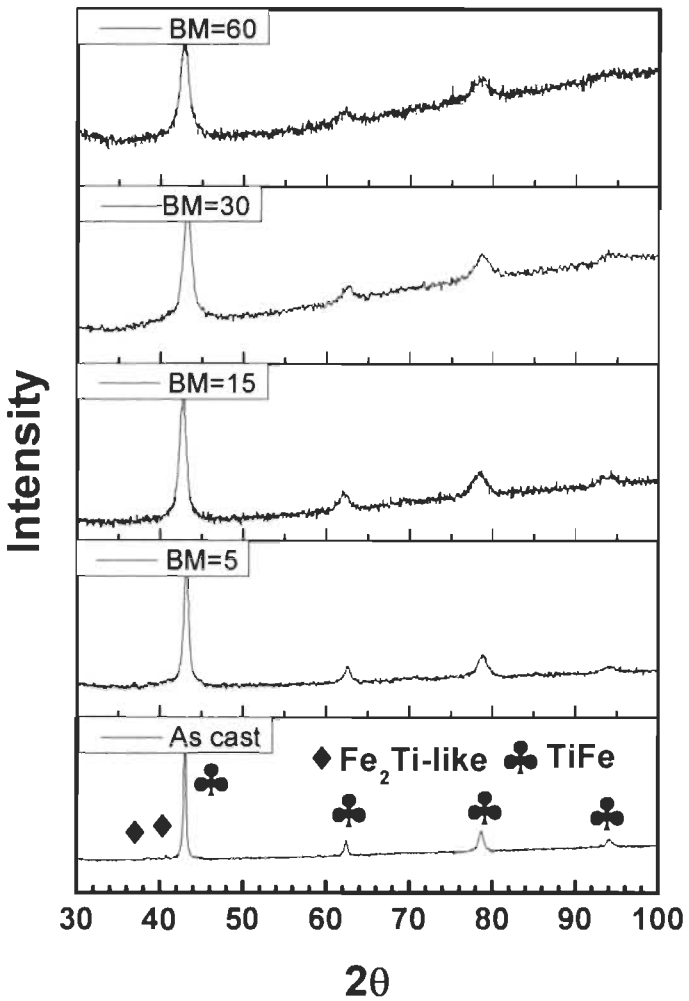

Fig 4.1.4–Powder diffraction patterns of TiFe+4 wt.% Zr alloy for as cast and different ball milling time

Table 4.1.1 shows the lattice parameters and crystallite sizes of all samples. The lattice parameter seems to have an erratic behavior but it should be mentioned that the literature value of the lattice parameter of TiFe varies from a lower boundary of 2.953(2) [82] to a upper boundary of 2.9802(2) Å [83]. In the present case, the lattice parameter is actually higher than the high boundary literature value but is agrees with the value recently published on for TiFe+4 wt.% Zr alloys [84]. This higher value could be explained by the presence of a small amount of Zr in solid solution in the TiFe lattice.

Table 4.1.1–Lattice parameter *a* (in Å) and crystallite size (nm) of TiFe phase of TiFe+4 wt.% Zr alloy in different state as determined by Rietveld analysis. The number in parenthesis is error.

Phase		As-cast	BM5min	BM15min	BM30min	BM60min
TiFe	*A*	2.9816(3)	2.9828(7)	2.9916(12)	2.976(2)	2.992(2)
	Crystallite size	23.2(3)	10.4(3)	8.4(3)	5.6(2)	4.8(2)

4.1.1.3. First hydrogenation

Fig 4.1.5 shows the first hydrogenation process at room temperature and under 4.5 MPa of hydrogen of TiFe alloy doped with 4 wt.% Zr. It can be seen that the as-cast alloy absorbs 1.6 wt.% in 2.5 hours. Ball milling slightly improves the hydrogenation kinetics but capacity decreases with milling time.

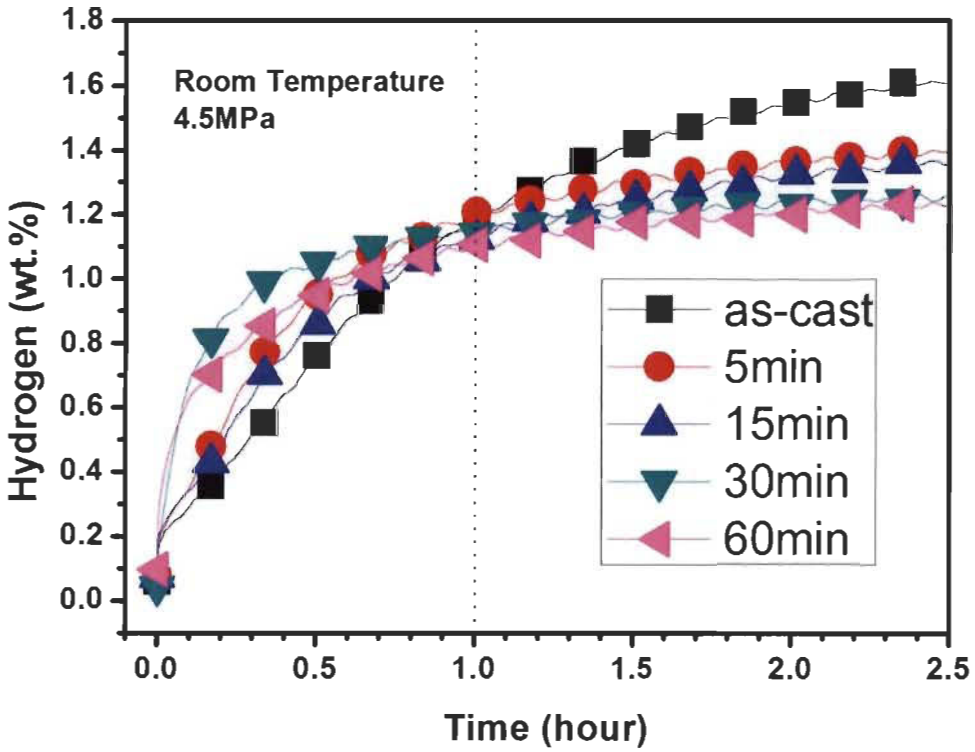

Fig 4.1.5–First hydrogenation of TiFe+4 wt.% Zr alloy at room temperature under 4.5 MPa hydrogen pressure for different states.

The reason why samples with longer ball milling time firstly shows a faster kinetics and lower hydrogen storage capacity has to be discussed. In Table 4.1.1 it can be seen that longer ball milling time is helpful for reducing the crystallite size. With increasing the ball milling time, both the particle size and the crystallite size decrease, leading to a faster diffusion of hydrogen along the particle surfaces and the grain boundaries. In addition, grain boundaries are favourable nucleation sites for the formation of the hydride phase [85]. This may explain the initial fast absorption kinetics of ball-milled samples with longer milling time.

Table 4.1.2 presents the total hydrogen capacity (wt.%) of powders hydrogenated for 5 hours, and the capacity retention (%) for all samples. The capacity retention is defined as the measured capacity over the theoretical capacity of TiFe (1.86 wt.%). It is easy to see that the capacity retention decreases with increasing ball milling times. In their investigation of ball milled magnesium hydride, Hanada et al explained that the decreased crystallite size associated with increasing grain boundary and lattice strains can lead to the decrease in hydrogen storage capacity [86]. This phenomenon

appears to be also present in our sample. Fig 4.1.6 shows the dependence of the total hydrogen capacity and the crystallite size on the ball milling time for the TiFe+4 wt.% Zr alloy. As can be seen, with the longer milling times the crystallite size and the total hydrogen capacity decrease in the same fashion.

Table 4.1.2–Total hydrogen capacity (wt.%) up to 5 hours and capacity retention S_n (%) of TiFe+4 wt.% Zr alloy in different state.

	As-cast	BM5min	BM15min	BM30min	BM60min
Total hydrogen capacity	1.64	1.55	1.51	1.31	1.29
Capacity retention (S_n)	88	83	81	70	69

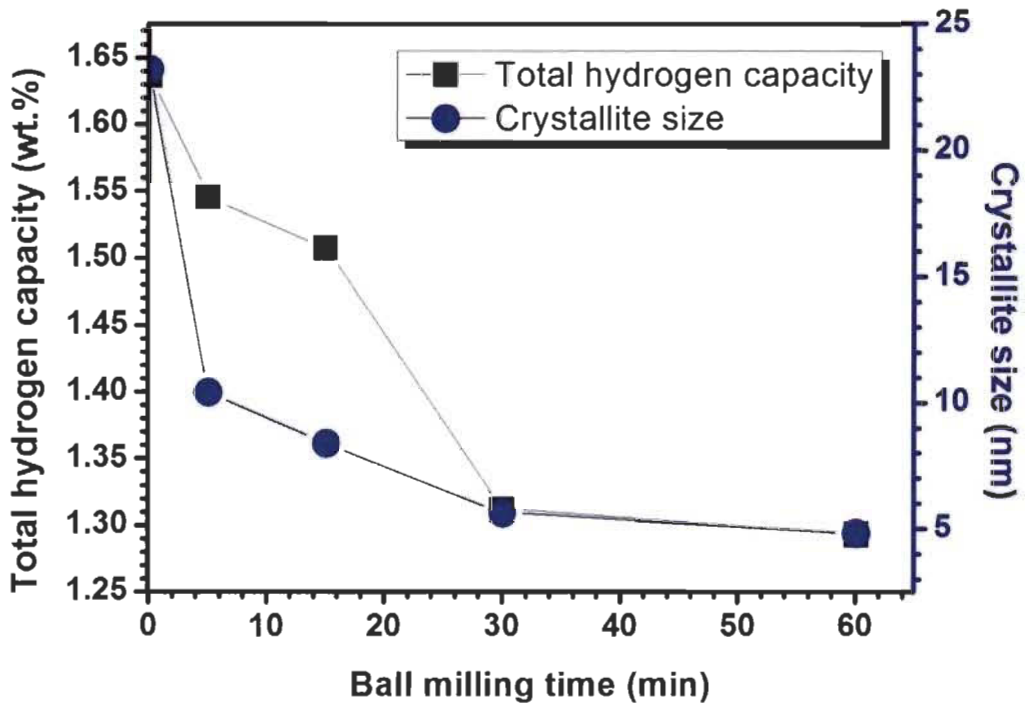

Fig 4.1.6–Relationship of total hydrogen capacity, crystallite size and ball milling time of TiFe+4 wt.% Zr alloy

4.1.1.4. Kinetic models of first hydrogenation

The first hydrogenation curves of different samples were analyzed by using the rate limiting step model equation (Nucleation-growth-impingement model (JMA) [16-18], Contracting volume model (CV) [19-21] and Ginstling-Brounshtein model (GB) [22, 23]) are reported in Table 1.3.

Fig 4.1.7 shows the plot for the first hydrogenation kinetics of representative BM=5 min sample. Linear regressions were performed on each model. As shown in the literature, the regressions are made in a range from 10% to 90% of the reaction's completion (α = 0.1~0.9 [24]). It can be clearly seen that GB3D shows a good fit. In addition, Table 4.1.3 shows the adjusted R^2 values for all rate limiting step model equations. It is clear that GB3D gives the best fit and that this model describes the best rate limiting step for the sample milled for 5 minutes. From the description given in Table 1.3, the GB3D model assumes the 3D growth and the growth interface velocity of diffusion decreases with time [77]. Similar plots were made for the first hydrogenation curves of all samples. The results indicate that the activation kinetics agree with the GB3D model for all of them.

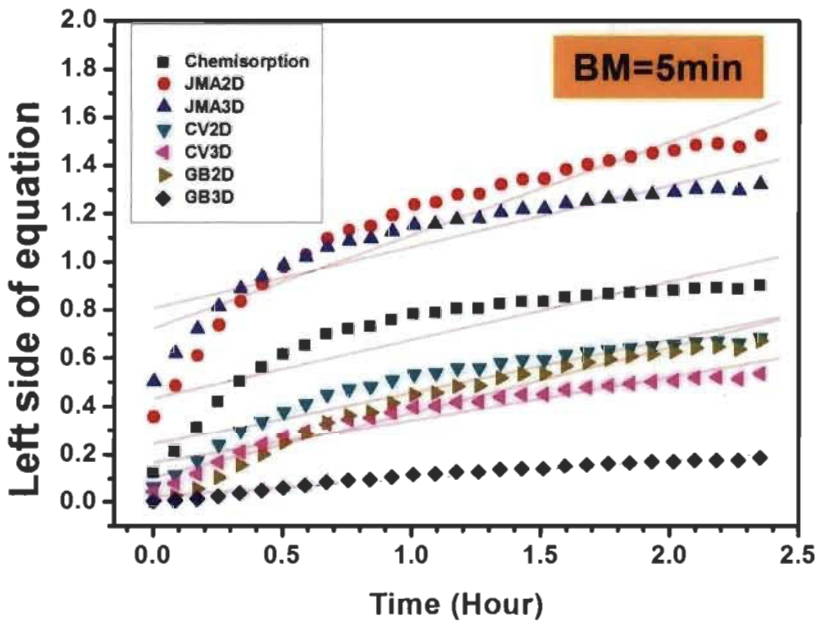

Fig 4.1.7–Rate limiting step curves of first hydrogenation of representative TiFe+4 wt.% Zr alloy milled for 5 minutes at room temperature under 4.5 MPa hydrogen pressure.

Table 4.1.3–Adjusted R^2 values for all model equations of BM=5 min sample

Sample	Model	R2
BM=5 min	Chemisorption	0.75898
	JMA2D	0.86556
	JMA3D	0.82911
	CV2D	0.86245
	CV3D	0.89291
	GB2D	0.92534
	GB3D	0.94649

4.1.2. Conclusion

Hydrogenation properties of mechanochemically processed TiFe with addition of 4 wt.% of Zr has been investigated. The as-cast sample shows TiFe as a main phase and traces of Fe_2Ti-like phase. Results of the first hydrogenation on samples that were processed by ball milling lead to the following conclusions:

(1) Ball milling significantly reduce the particle/crystallite sizes with most of the reduction occurring during the first 15 minutes of milling. In addition, ball milling produced particle agglomeration which increases with milling times.

(2) High energy milling at room temperature improves the initial hydrogenation kinetics of processed powders as compared with the as-cast sample but reduces the H-storage capacity. The faster kinetics is due to the reduction of the crystallite sizes and formation of new grain boundaries. The reduced hydrogen storage capacity may be explained by the formation of grain boundaries that enhance the hydrogen diffusion but do not store hydrogen in their structures.

(3) The first hydrogenation kinetics for all samples agrees well with the GB3D model. The feature of this model is that the 3D growth and the growth interface velocity of diffusion decrease with time.

4.2. Effect of cold rolling and forging on the first hydrogenation properties of TiFe alloy doped with 4 wt.% Zr as additive

In a previous investigation, it has been proved that cold rolling is very effective to enhance activation of $LaNi_5$ alloy [45]. This led to the use cold rolling and another deformation technique forging, on the as-cast material to see if there is any improvement of first hydrogenation.The effect of cold rolling (5, 10 and 15 passes) and forging (5 passes) on the microstructure and hydrogenation properties of TiFe alloy with 4 wt.% zirconium as additive is reported in this chapter.

4.2.1. Results and discussion

4.2.1.1. Morphology

Fig 4.2.1 shows the SEM micrographs before (a, c, e, g, i) and after (b, d, f, h, j) hydrogenation of TiFe+4 wt.% Zr alloy in different states (As-cast, CR5, CR10, CR15 and Forging). For the SEM micrographs before hydrogenation, it can be clearly seen that as-cast (a) and forging (i) samples show big flat particles. Cold rolled samples present more cracks and small particles with increasing the rolling pass. In the case of hydrogenated samples, we can find some obvious cracks from the hydrogenated as-cast (b) and forging (j) samples due to the effect of lattice expansion.

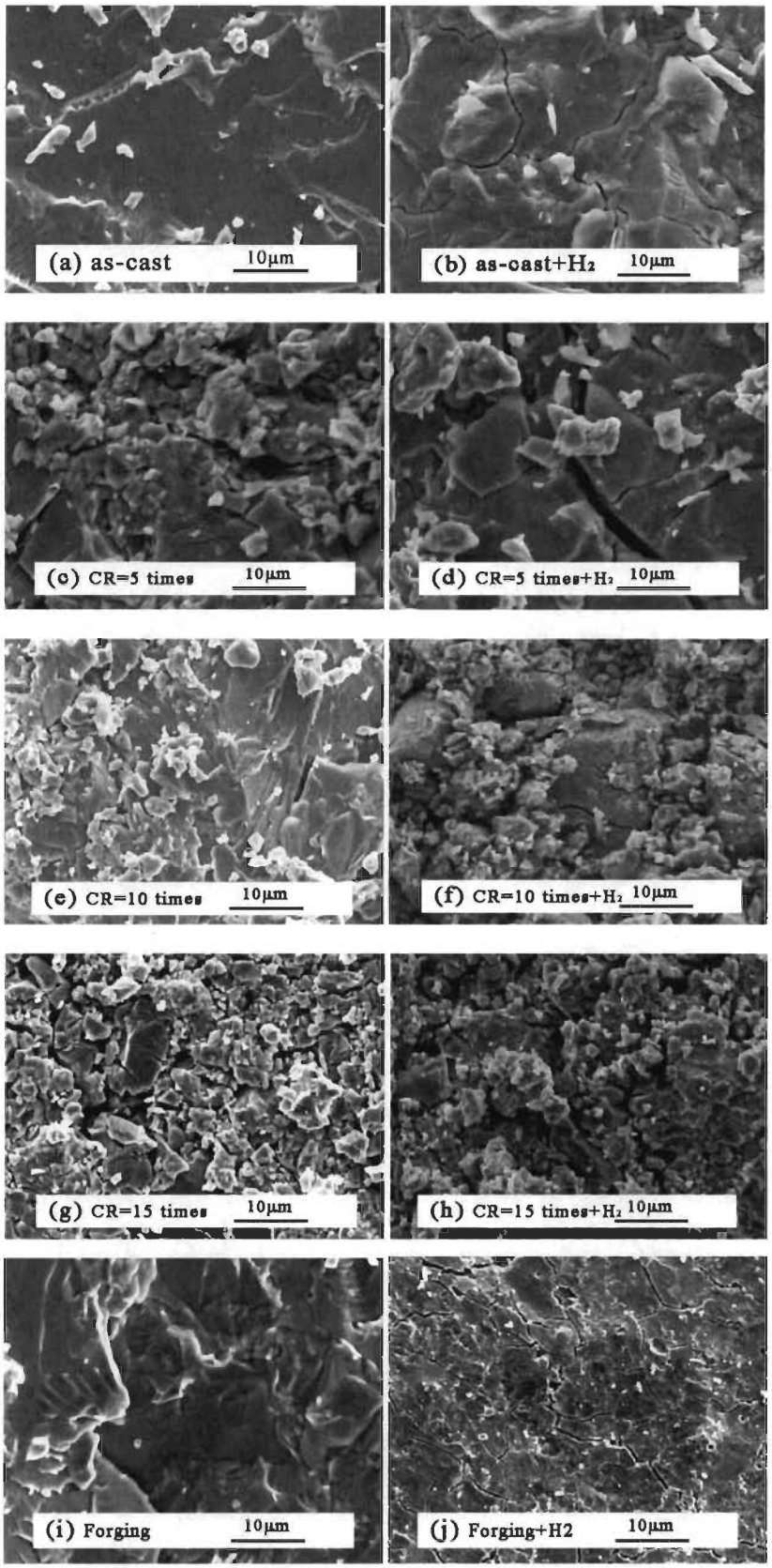

Fig 4.2.1–SEM micrographs of TiFe+4 wt.% Zr alloy for different states (as-cast, CR5, CR10, CR15 and Forging) before and after hydrogenation.

4.2.1.2. Crystal structure characterization

The XRD patterns of TiFe+4 wt.% Zr alloy for different states are presented in Fig 4.2.2. It can be seen clearly that all the samples have TiFe as the main phase. At the same time some small peaks at around 38~45° also can be seen. As it is discussed in chapter 4.1, these small peaks show a same crystal structure of Fe_2Ti-like ($MgZn_2$ type) [74].

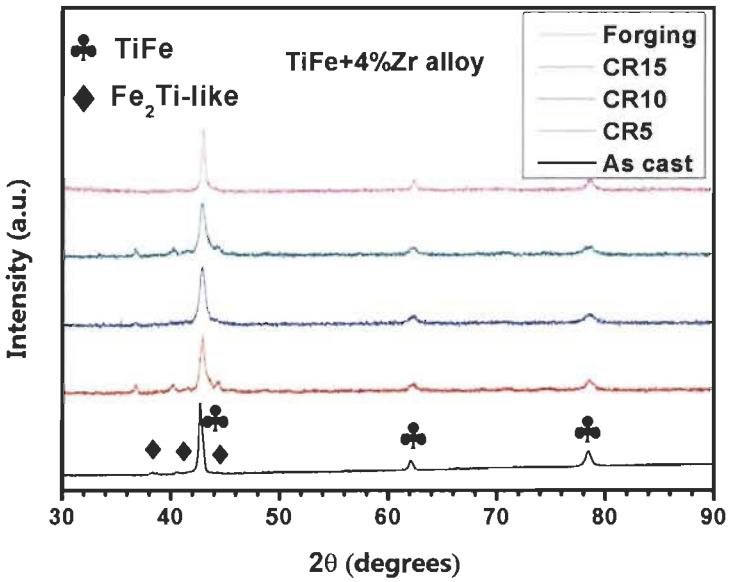

Fig 4.2.2–Powder diffraction patterns of TiFe+4 wt.% Zr alloy for different states.

Table 4.2.1 shows the lattice parameter *a* (in Å) and crystallite size (nm) of TiFe phase as determined by Rietveld's analysis. The crystallite size slightly decreases with rolling pass up to 15 passes. In the case of forging, it is clear that it doesn't have any impact on crystallite size and lattice parameter.

Table 4.2.1-Lattice parameter *a* (in Å) and crystallite size (nm) of TiFe phase for TiFe+4 wt.% Zr alloy in different states as determined by Rietveld analysis. The number in parenthesis is error.

Parameters	As-cast	CR5	CR10	CR15	Forging
A	2.9816(3)	2.9805(6)	2.9813(7)	2.9830(7)	2.9816(4)
Crystallite size	23.2(3)	15.3(3)	11.74(18)	11.9(2)	23.9(6)

4.2.1.3. First hydrogenation

Fig 4.2.3 shows the first hydrogenation at room temperature and under 4.5 MPa of hydrogen of TiFe+4 wt.% Zr alloy for different states. The as-cast sample was handled in argon. Cold rolling and forging were processed in air. Prior to the measurement, the samples were kept under vacuum for 1 h at room temperature. It can be seen that CR5 sample show the fastest initial hydrogenation kinetics among all samples. Further rolling reduced the kinetics and maximum capacity. In the case of forging, the kinetics and capacity are quite similar to the as-cast characteristics.

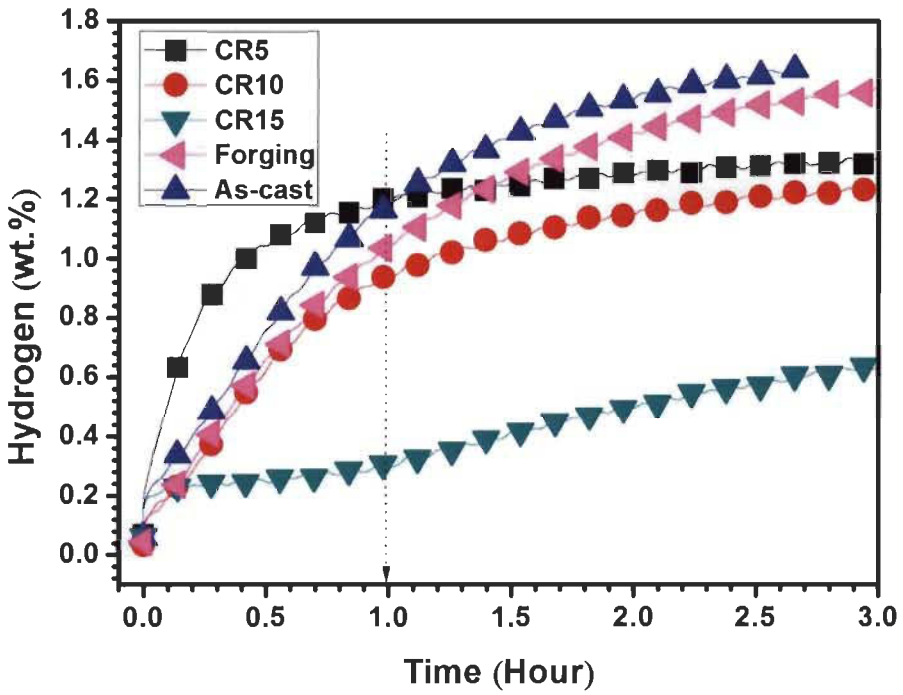

Fig 4.2.3–First hydrogenation at room temperature under 4.5 MPa hydrogen pressure of TiFe+4 wt.% Zr alloy for different states (as cast, cold rolling and forging in Air).

4.2.1.4. Kinetic models of first hydrogenation

Similarly to chapter 4.1, the first hydrogenation curves of TiFe doped with 4 wt.% Zr in different states also are analyzed by using the rate limiting step model equations that are reported in Table 1.3.

Fig 4.2.4 shows the fitting plot for the first hydrogenation kinetics in different states. It is found that CV3D and GB3D show the best fit for each sample. In order to compare this two models clearly, the adjusted R^2 values for each sample is shown in Table 4.2.2.

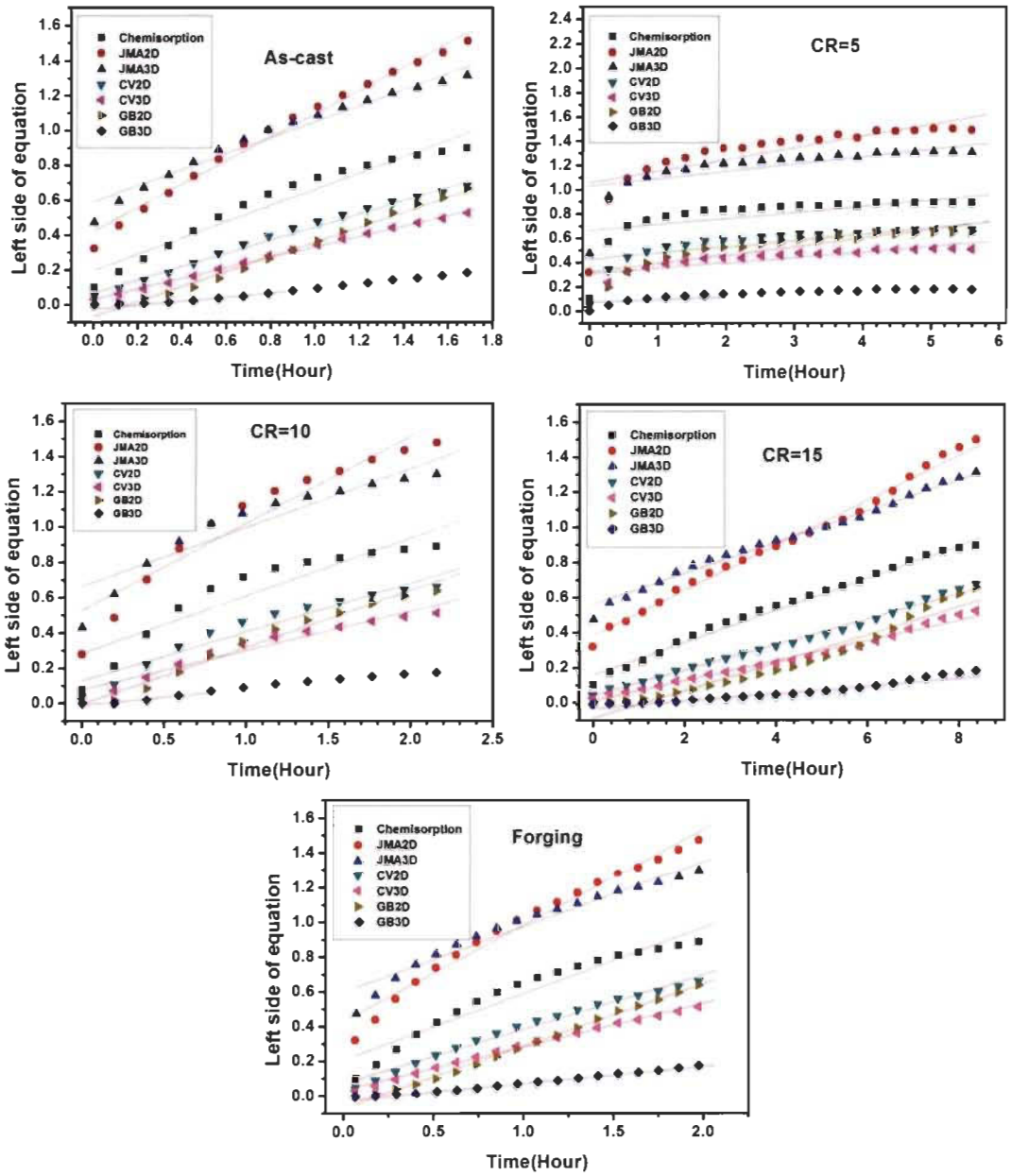

Fig 4.2.4–Rate limiting step curves of first hydrogenation of TiFe+4 wt.% Zr alloy in different states at room temperature under 4.5 MPa hydrogen pressure

Table 4.2.2 shows the best rate limiting step model for all samples. GB3D can show the best fit for all samples except for the as-cast and forged samples where the difference between GB3D and CV3D is small and makes both rate-limiting steps undistinguishable.

Table 4.2.2–The best fit rate limiting step model for all samples

Sample	Model
As cast	CV3D
	GB3D
CR5	GB3D
CR10	GB3D
CR15	GB3D
Forging	CVD
	GB3D

4.2.2. Conclusion

The microstructure and first hydrogenation properties of TiFe+4 wt.% Zr alloy using cold rolling and forging have been investigated. It is found that all samples are made of a main TiFe phase and a minor phase that shows Fe_2Ti-like crystal structure ($MgZn_2$ type). The main results were:

(1) Cold rolling can significantly reduce the particle and crystallite sizes.

(2) As-cast sample shows the maximum hydrogen capacity. Cold-rolled sample with 5 passes shows the fastest hydrogenation kinetics in the first hour of reaction but the total capacity is reduced. The maximum capacity was also lowered by forging.

(3) All samples show a GB3D rate limiting step model. For as-cast and forged samples, they also may show CV3D model.

4.3. Effect of cold rolling and forging on the first hydrogenation performance of TiFe alloy doped with 4 wt.% (Zr+2Mn) as additive

It was shown in chapter 3.2 that TiFe alloy with 4 wt.% (Zr+2Mn) can absorb hydrogen. But the incubation time of first hydrogenation is very long (around 5 hours). This will limit the application of this alloy. As it is shown in chapter 4.2, cold rolling can reduce the crystallite size and improve the initial first hydrogenation kinetics of TiFe doped with 4 wt.% Zr. This led us to investigate the effect of cold rolling on TiFe alloy with 4 wt.% (Zr+2Mn) alloy.

I supervised an undergraduate student to study the effect of ball milling on the first hydrogenation of TiFe+4 wt.% (Zr+2Mn) alloy. A paper about this research was published [87]. In this chapter, the main results of this investigation are presented.

4.3.1. Results and discussion

4.3.1.1. Morphology

Fig 4.3.1 shows the SEM micrographs of TiFe+4 wt.% (Zr+2Mn) in different states (as cast, CR1, CR5 and Forging). These three samples all show a big plate. For CR5 sample it can be seen that the surface of the particle is full of cracks and small grains. This also means that five rolling passes are effective to produce the deformation with lots of defects. For forging sample several cracks are also seen on the surface.

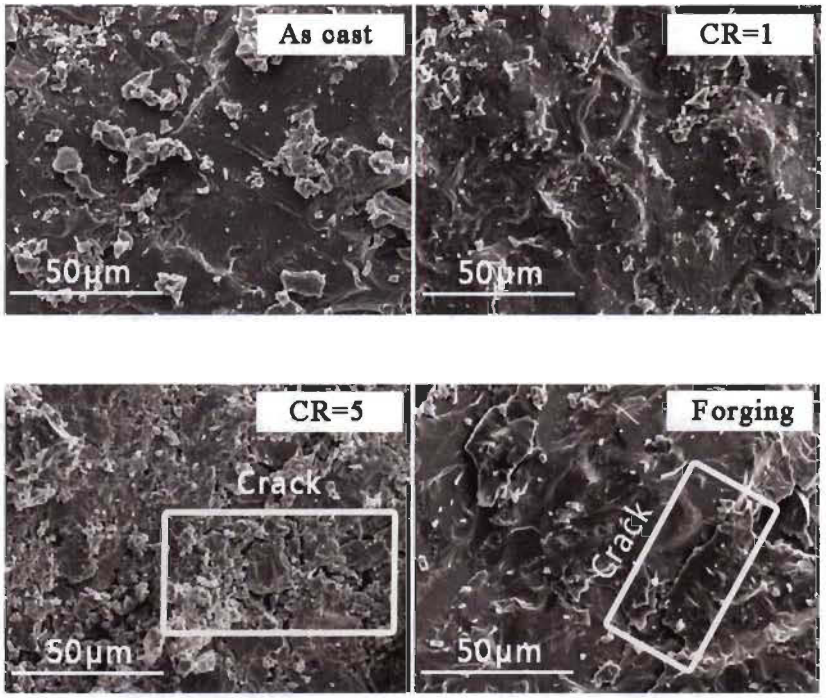

Fig 4.3.1–SEM micrographs of TiFe+4 wt.% (Zr+2Mn) alloy in different states.

4.3.1.2. Crystal structure

The XRD patterns of TiFe+4 wt.% (Zr+2Mn) alloy for different ball milling time are presented in Fig 4.3.2. It can be seen clearly that all samples show a TiFe main phase. For the secondary phase these small peaks could be indexed to a Fe_2Ti-like crystal structure as seen in chapter 4.1 and 4.2.

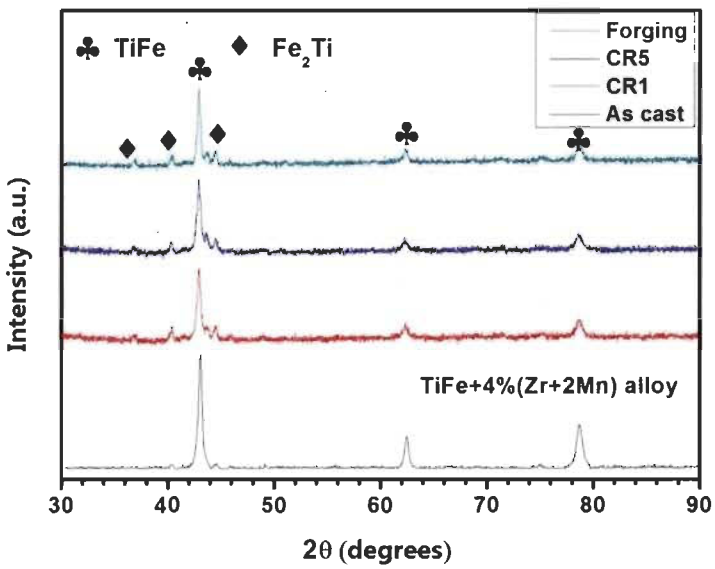

Fig 4.3.2–Powder diffraction patterns of TiFe+4 wt.% (Zr+2Mn) alloy for different states.

Table 4.3.1 shows the lattice parameter *a* (in Å) and crystallite size (nm) of TiFe phase as determined by Rietveld analysis. The crystallite size slightly decreases with rolling. Forging can't reduce the crystallite size.

Table 4.3.1-Lattice parameter (in Å) and crystallite size (nm) of TiFe phase for TiFe+4 wt.% (Zr+2Mn) alloy in different ball milling time as determined by Rietveld analysis. The number in parenthesis is error.

Parameters	As cast	CR1	CR5	Forging
a	2.9799(2)	2.9793(5)	2.9802(6)	2.9785(4)
Crystallite size	19.5(5)	17.7(4)	16.7(4)	26.3(7)

4.3.1.3. First hydrogenation

Fig 4.3.3 shows the first hydrogenation at room temperature and under 2 MPa of hydrogen of TiFe+4 wt.% (Zr+2Mn) alloy in different states. The as-cast sample was crushed in glovebox. Cold-rolled and forged samples were performed in air. Prior to the measurement, the samples were kept under vacuum for 1 h at room temperature. It is seen that within 5 hours as cast and forging samples can't absorb any hydrogen. CR5 sample shows the fastest hydrogenation kinetics among all samples. However this sample only shows a full hydrogenation of 1.0 wt.% hydrogen. CR1 sample shows the highest capacity among all samples: 1.5 wt.%. If the measuring time is prolonged to 18 hours, it can be clearly seen that the as cast sample has an incubation time of about 6 hours. Forging sample still can't be activated until 18 hours.

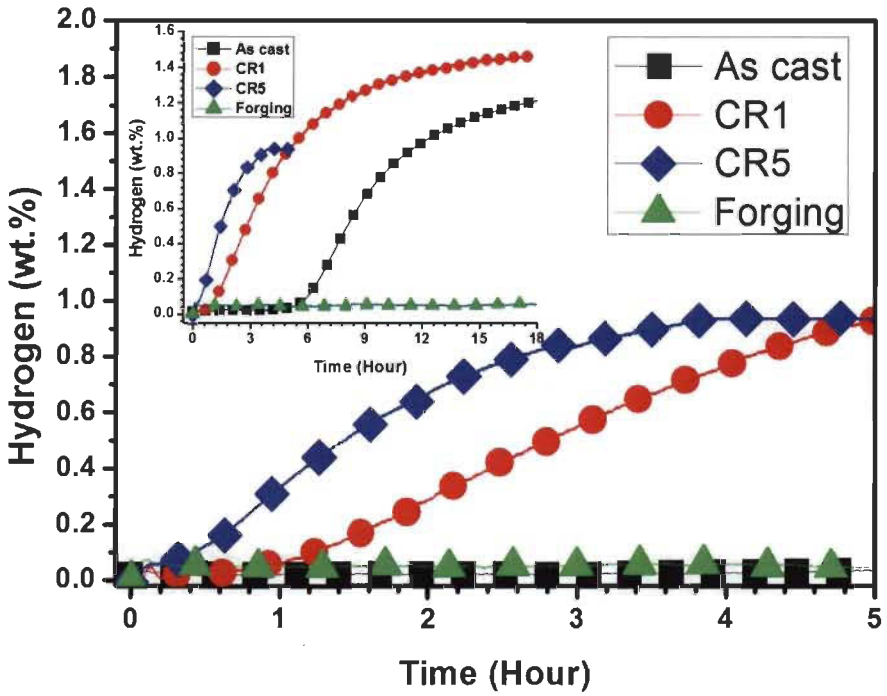

Fig 4.3.3–First hydrogenation of TiFe+4 wt.% (Zr+2Mn) alloyin different state (as-cast in argon, cold rolling and forging in air) at room temperature under 2 MPa hydrogen pressure.

Comparing these hydrogenation curves, it can be found that one rolling pass is a good choice for improving the first hydrogenation performances of TiFe doped with 4 wt.% (Zr+2Mn) alloy due to the relatively fast reaction rate and highest capacity. Because cold rolling is performed in the air, the proportion of oxides increases with the number of rolling passes. The thick oxidation layers can block the diffusion of hydrogen and lower the capacity. Regarding the forged sample, the reason why it doesn't absorb hydrogen is still unclear. Despite having some cracks, this sample is probably denser than the other ones and this may plays a role. Further tests are needed in order to get a true explanation.

4.3.1.4. Rate limiting step of first hydrogenation

The rate limiting step of first hydrogenation for TiFe doped with 4 wt.% (Zr+2Mn) is reported in this section. According to the rate limiting step model equations in Table 1.3, the rate limiting step curves in different states (as cast, cold rolling 1 and 5 pass)

were plotted in Fig 4.3.4. It is clearly seen that CV2D, CV3D, GB2D and GB3D all show good fit for all samples.

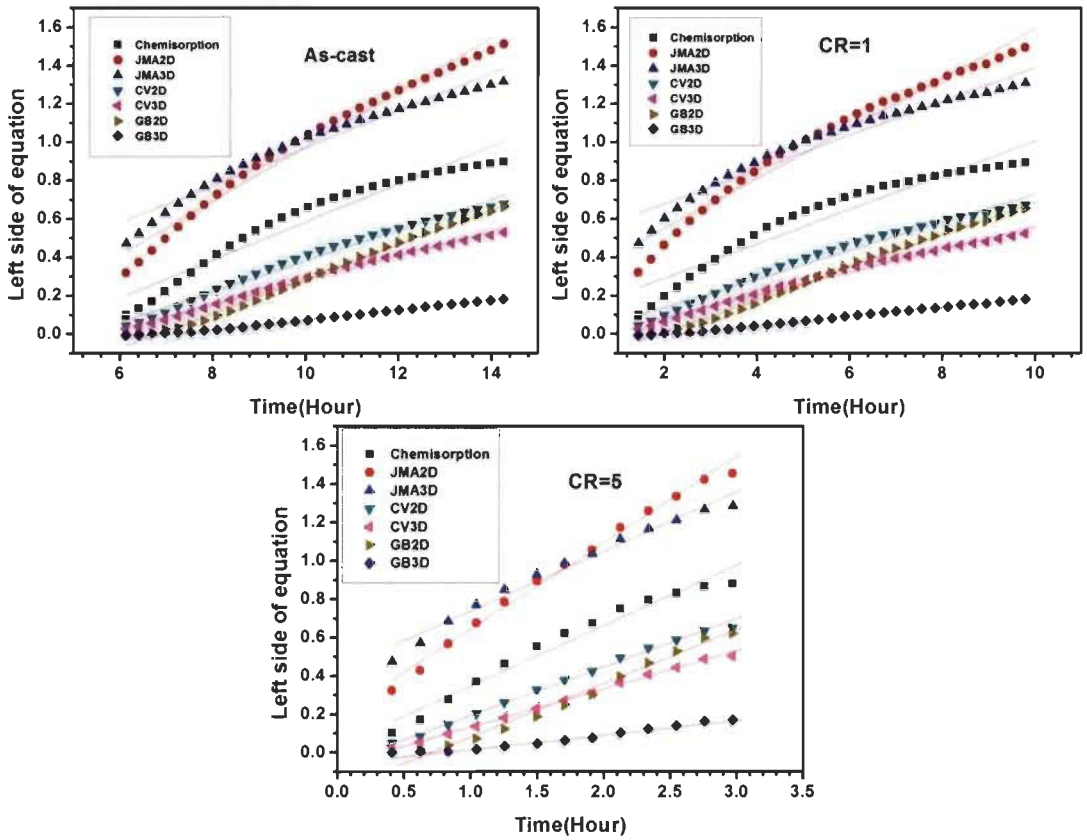

Fig 4.3.4–Rate limiting step curves of first hydrogenation of TiFe+4 wt.% (Zr+2Mn) alloy in different states at room temperature under 2 MPa hydrogen pressure.

The adjusted R^2 values for linear fits of rate limiting step are shown in Table 4.3.2. For each sample, two or three models gives very close adjusted R^2 values, making the clear identification of the rate limiting step difficult. If we just take the highest adjusted R^2 value for each sample then the respective rate limiting steps of as-cast, CR1 and CR5 are respectively GB2D, GB2D and CV3D.

Table 4.3.2–Adjusted R^2 values for all model equations of all samples

Sample	Model	R^2
As cast	Chemisorption	0.94187
	JMA2D	0.98144
	JMA3D	0.96185
	CV2D	0.98654
	CV3D	0.99486
	GB2D	0.99527
	GB3D	0.99176
CR1	Chemisorption	0.92421
	JMA2D	0.97247
	JMA3D	0.95008
	CV2D	0.97769
	CV3D	0.98907
	GB2D	0.99625
	GB3D	0.99609
CR5	Chemisorption	0.96724
	JMA2D	0.99303
	JMA3D	0.98051
	CV2D	0.99545
	CV3D	0.99774
	GB2D	0.98396
	GB3D	0.97487

4.3.2. Conclusion

The microstructure and first hydrogenation performance of TiFe doped with 4 wt.% (Zr+2Mn) alloy subjected to cold rolling and forging have been investigated. Cold rolling can effectively reduce the crystallite size. Cold-rolled sample with 1 pass shows the highest capacity and cold-rolled sample with 5 passes presents the fastest initial hydrogenation kinetics. The forged sample doesn't absorb any hydrogen. The rate limiting step for as cast and 1 cold-rolled pass is GB2D. However, the rate limiting step for cold-roll sample with 5 passes matches with CV3D model.

5. Conclusion and future work

5.1. Conclusion

In this thesis the effect of different additives (Zr, Zr+2Mn and Zr+2V) on the microstructure and hydrogenation properties of TiFe alloy was studied. The result shows that these three additives can improve the first hydrogenation kinetics. Further, the investigation about the effect of mechanical deformation on the first hydrogenation property of TiFe doped with 4 wt.% zirconium and (Zr+2Mn) indicates that ball milling and cold rolling can effectively reduce the crystallite size. Generally speaking, ball milling and cold rolling also are helpful for enhancing the first hydrogenation kinetics.

5.2. Future work

5.2.1. Study the dark and bright phases of TiFe alloy doped with Zr+2Mn/Zr+2V

From chapter 3.2 and 3.3 it can be seen that the dark and bright phases have a significant effect on the microstructure and hydrogenation performances of TiFe doped with (Zr+2Mn) and (Zr+2V). So identifying the dark and bright phases and the mechanism of their absorption and desorption is necessary. One way would be to prepare samples with the dark and bright phase compositions to study their crystal structure and hydrogen storage behaviours.

5.3. Perspective

Besides TiFe-based alloys, Mg-based alloys and complex hydrides are also interesting.

The high absorption and desorption temperature and slow reaction rate are two big problems for the application of Mg-based alloys. Recently Lin et.al reported that $Mg_3LaNi_{0.1}$ alloy can absorbs hydrogen (2.7 wt.%) at 30°C [88]. However the capacity is too low. So lowering the absorption and desorption temperature and keeping the relatively high hydrogen storage capacity need still to be solved. The

addition of other rare earth and transition metals elements may leads to alloys with better capacities at room temperature.

For complex hydrides, metal borohydrides as hydrogen storage materials attract lot of attention due to their high theoretical hydrogen storage capacity. But the high desorption temperature has an important effect on its application. In addition, the mechanism of desorption of borohydrides is still not very clear. Recently researchers also found that some complex hydrides show multi-functionality such as ion conductivity, catalytic, magnetic and optical properties. These properties could help to provide new ideas to extend their applications in the future [89].

SECTION B

Ideal is the beacon. Without ideal, there is no secure direction; without direction, there is no life. ——Leo Tolstory

Articles

1. Lv P, Huot J. Hydrogen storage properties of $Ti_{0.95}FeZr_{0.05}$, $TiFe_{0.95}Zr_{0.05}$ and $TiFeZr_{0.05}$ alloys [J]. International Journal of Hydrogen Energy, 2016, 41(47): 22128-22133.
2. Lv P, Huot J. Hydrogenation improvement of TiFe by adding $ZrMn_2$ [J]. Energy, 2017, 138: 375-382.
3. Lv P, Guzik M, Sarori S, Huot J. Effect of ball milling and cryomilling on the microstructure and first hydrogenation properties of TiFe + 4 wt.% Zr alloy. International Journal of Hydrogen Energy, Submitted.
4. Lv P, Huot J. Microstructure evolution, phase transformation and hydrogenation properties of TiFe alloy doped with (Zr+2V) as additive. Journal of power source. In process.
5. Lv P, Huot J. Effect of cold rolling and forging on the microstructure and first hydrogenation properties of TiFe alloy doped with 4 wt.% Zr as additive. International Journal of Hydrogen Energy. In process.
6. Lv P, Huot J. Microstructure and first hydrogenation properties of TiFe alloy doped with 4 wt.% (Zr+2Mn) by cold rolling and forging. Journal of Alloy and Compounds. In process.
7. Romero G, Lv P, Huot J. Effect of ball milling on the first hydrogenation properties of TiFe alloy doped with 4 wt.% (Zr+2Mn) as additive. Journal of Materials Science. pp 1-7.

Note: My name can be written as LYU PENG and LV PENG.

Article 1

Hydrogen storage properties of $Ti_{0.95}FeZr_{0.05}$, $TiFe_{0.95}Zr_{0.05}$ and $TiFeZr_{0.05}$ alloys

Peng Lv, Jacques Huot*

Hydrogen Research Institute, Université du Québec à Trois-Rivières, 3351 des Forges, Trois-Rivières , G9A 5H7, Canada

Abstract: In this paper, we report the microstructure and hydrogen storage properties of $Ti_{0.95}FeZr_{0.05}$, $TiFe_{0.95}Zr_{0.05}$ and $TiFeZr_{0.05}$ alloys prepared by arc melting. We found that all these alloys are made of a dark TiFe phase with small amount of zirconium and a bright secondary phase which is zirconium rich. At the same time it can be seen that the partial substitution of zirconium for iron, titanium or both can obviously improve the first hydrogenation kinetics of FeTi. First hydrogenation of $Ti_{0.95}FeZr_{0.05}$ alloy proceed faster than for the other two alloys. This is probably due to a finer distribution of the bright secondary phase. Pressure-composition isotherms of $TiFeZr_{0.05}$ and $Ti_{0.95}FeZr_{0.05}$ alloys are similar while the alloy $TiFe_{0.95}Zr_{0.05}$ shows the highest capacity. These results demonstrate that a very slight variation of composition could have an important effect of microstructure and hydrogen storage behaviours.

Keywords: TiFe alloy; Morphology; Activation; Hydrogen storage properties

INTERNATIONAL JOURNAL OF HYDROGEN ENERGY 41 (2016) 22128–22133

Available online at www.sciencedirect.com

ScienceDirect

journal homepage: www.elsevier.com/locate/he

Hydrogen storage properties of $Ti_{0.95}FeZr_{0.05}$, $TiFe_{0.95}Zr_{0.05}$ and $TiFeZr_{0.05}$ alloys

*Peng Lu, Jacques Huot**

Hydrogen Research Institute, Université du Québec à Trois-Rivières, 3351 des Forges, Trois-Rivières, G9A 5H7, Canada

ARTICLE INFO

Article history:
Received 12 June 2016
Received in revised form
11 July 2016
Accepted 12 July 2016
Available online 29 July 2016

Keywords:
TiFe alloy
Morphology
Activation
Hydrogen storage properties

ABSTRACT

In this paper, we report the microstructure and hydrogen storage properties of $Ti_{0.95}FeZr_{0.05}$, $TiFe_{0.95}Zr_{0.05}$ and $TiFeZr_{0.05}$ alloys prepared by arc melting. We found that all these alloys are made of a TiFe phase with small amount of zirconium in solid solution and a secondary phase which is zirconium rich. This special microstructure is actually responsible for the enhanced activation (first hydrogenation) kinetics of these alloys. First hydrogenation of $Ti_{0.95}FeZr_{0.05}$ alloy proceed faster than for the other two alloys. This is probably due to a finer distribution of the bright secondary phase. Pressure-composition isotherms of $TiFeZr_{0.05}$ and $Ti_{0.95}FeZr_{0.05}$ alloys are similar while the alloy $TiFe_{0.95}Zr_{0.05}$ shows the highest capacity. These results demonstrate that a very slight variation of composition could have an important effect of microstructure and hydrogen storage behaviours.

Introduction

TiFe alloy is a promising candidate for solid state hydrogen storage because of its low price, reasonable storage capacity, low operation temperature and good reversibility [1,2]. However, the first hydrogenation (activation) of TiFe alloy is usually difficult [3,4]. For example, in one of the first studies of TiFe, Reilly et al. reported that activation could only be achieved through exposure to high temperature (673 K) and high pressure [5]. Addition of transition metals [6,7] and microstructural modifications [8] have been shown to be two ways to increase the first hydrogenation kinetics for TiFe alloy.

In an early investigation, Shenzhong et al. found that adding a small amount of Mn to TiFe alloy can improve the activation kinetics of FeTi alloy [9]. Later, Nishimiya et al. found that zirconium substitution for titanium in FeTi alloy can lower the equilibrium pressure and narrow the width of the plateau at 293 and 313 K [10]. In addition, increasing the zirconium content can increase the hydrogen capacity. Recently, Jain et al. observed that adding 4 wt.%. zirconium can shorten the incubation time of the first hydrogenation without changing the reversible storage capacity [11]. All of these studies show that some transition metals have a positive effect on the hydrogen storage properties of TiFe alloy.

Zadorozhnyy et al. reported that nanocrystalline TiFe intermetallic compound synthesized by mechanical alloying shows a hydrogen capacity of about 1.4 wt.% at room temperature [12]. Emami et al. found that the first hydrogenation of TiFe processed by ball milling is improved and not sensitive to the air [13]. This study shows clearly that there is a strong relation between the microstructure of TiFe and its activation for hydrogen absorption.

* *Corresponding author.*
E-mail address: jacques.huot@uqtr.ca (J. Huot).
http://dx.doi.org/10.1016/j.ijhydene.2016.07.091

In a previous work, we found that adding 4wt.% zirconium to TiFe alloy can improve the activation kinetics [14]. This investigation, showed that a small amount of zirconium (about 1 at.%) is in solid solution in the main TiFe phase while the abundance of zirconium is much higher in the secondary phase. This raised the question of the localization of zirconium in the TiFe matrix. Does zirconium substitute on the titanium or the iron site or goes in some interstitial site? To answer this question the microstructure and hydrogen storage properties of three closely related compositions: $Ti_{0.95}FeZr_{0.05}$, $TiFe_{0.95}Zr_{0.05}$ and $TiFeZr_{0.05}$ have been investigated.

Experimental

All pure elements Fe(99.9%), Ti(99.9%) and Zr(99.5%) were purchased from Alfa Aesar. The alloys were prepared using arc melting in Ar atmosphere. Each pellet was melted and turned over three times in order to get homogeneity.

The crystal structure was determined by X-ray diffraction (XRD; Bruker D8 Focus; Cu Kα radiation). Lattice parameters were evaluated from Rietveld method using Maud software [15,16]. The percentage of different phases was analysed by image J software [17,18]. The hydrogen storage properties were measured by using a home-made Sieverts-type apparatus. Microstructure and chemical analysis were performed using a JEOL JSM-5500 scanning electron microscopy equipped with an EDX (Energy Dispersive X-Ray) apparatus from Oxford Instruments.

Results and discussion

Morphology

Fig. 1 shows backscattered electron micrographs of $Ti_{0.95}FeZr_{0.05}$, $TiFe_{0.95}Zr_{0.05}$ and $TiFeZr_{0.05}$ alloys prepared by arc melting. Surprisingly, even if the compositions are very similar they have totally different microstructure. All compositions are made of a dark phase which is TiFe phase. As will be demonstrated later, the bright phase is zirconium-rich. The crystal structure of this phase is under investigation and the preliminary results indicates that the structure is probably $MgZn_2$ type (space group P63/mmc). A more complete description of this phase will be the object of a forthcoming paper. In this paper, the TiFe will be called 'dark' phase and the $MgZn_2$ type secondary will be called 'bright phase'. Using image J software, the bright and dark phase areas were computed and the numerical values are reported in Table 1.

From Table 1 we see that the bright phase surface area is much lower in $TiFe_{0.95}Zr_{0.05}$ sample than the other two compositions. It can also be seen that $Ti_{0.95}FeZr_{0.05}$ and $TiFeZr_{0.05}$ alloys have similar ratio of bright and dark phases.

In order to know the chemical composition of the bright and dark phases, EDX measurement was performed on each alloy. First, the bulk atomic abundance was measured and compared to the nominal composition. The numerical values are reported in Table 1. It is clear that the atomic % of all elements are very close to the nominal composition.

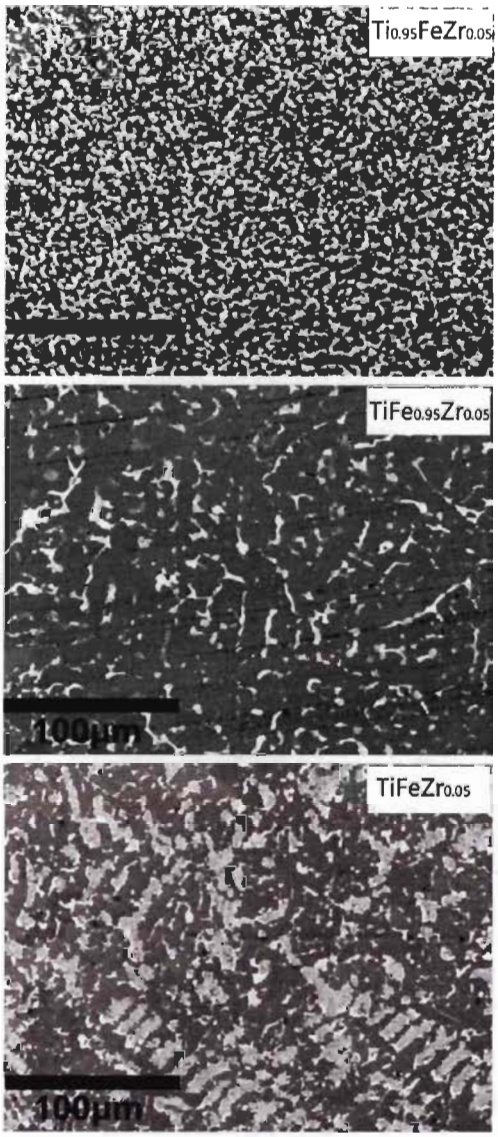

Fig. 1 – Backscattered electron micrographs of $Ti_{0.95}FeZr_{0.05}$, $TiFe_{0.95}Zr_{0.05}$ and $TiFeZr_{0.05}$ alloys prepared by arc melting.

Table 1 Percentage of bright and dark areas for $Ti_{0.95}FeZr_{0.05}$, $TiFe_{0.95}Zr_{0.05}$ and $TiFeZr_{0.05}$ micrographs shown in Fig. 1.

Phase	$Ti_{0.95}FeZr_{0.05}$	$TiFe_{0.95}Zr_{0.05}$	$TiFeZr_{0.05}$
Bright (%)	37	11	31
Dark (%)	63	89	69

Table 2 Bulk atomic abundance and nominal bulk atomic abundance as measured by EDX of $Ti_{0.95}FeZr_{0.05}$, $TiFe_{0.95}Zr_{0.05}$ and $TiFeZr_{0.05}$ alloys.

Sample		Ti(at.%)	Fe(at.%)	Zr(at.%)
$Ti_{0.95}FeZr_{0.05}$	Nominal composition	47.5	50.0	2.5
	Measurement	47.0	50.3	2.7
$TiFe_{0.95}Zr_{0.05}$	Nominal composition	50.0	47.5	2.5
	Measurement	51.3	45.8	2.9
$TiFeZr_{0.05}$	Nominal composition	48.8	48.8	2.4
	Measurement	47.3	49.7	3.1

Second, we measured the atomic composition of the dark and bright phases of each alloy. The microstructure and element mapping of $Ti_{0.95}FeZr_{0.05}$ alloy are shown in Fig. 2. It is clear that zirconium is concentrated in the secondary phase.

The elements distribution of $TiFe_{0.95}Zr_{0.05}$ alloy are presented in Fig. 3. As for the preceding composition, zirconium is mainly located in the bright phase. However, iron is slightly depleted in the bright phase. That is confirmed by the quantitative analysis reported in Table 3.

Fig. 4 shows the micrograph and element mapping of $TiFeZr_{0.05}$. Even if the morphology is different, the distribution seems similar to the $Ti_{0.95}FeZr_{0.05}$ alloy.

For each alloy, a quantitative analysis of the dark phase (point 2) and bright phase (point 1) was performed and reported in Tables 3 and 4 respectively. From Table 3, we see that the dark phase of the three alloys has identical elements abundances. In particular, it should be noted that zirconium abundance is less than 1 at.%.

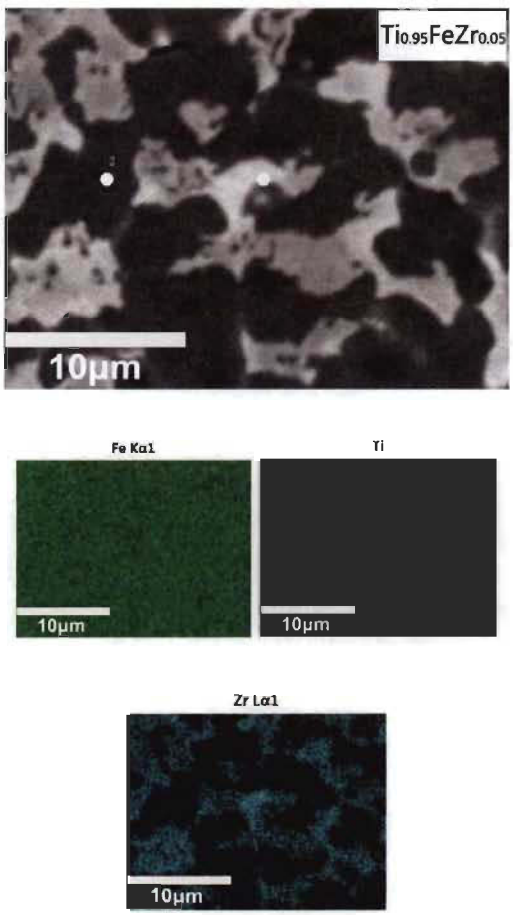

Fig. 2 – Backscattered electron micrograph of $Ti_{0.95}FeZr_{0.05}$ alloy prepared by arc melting with elements mapping.

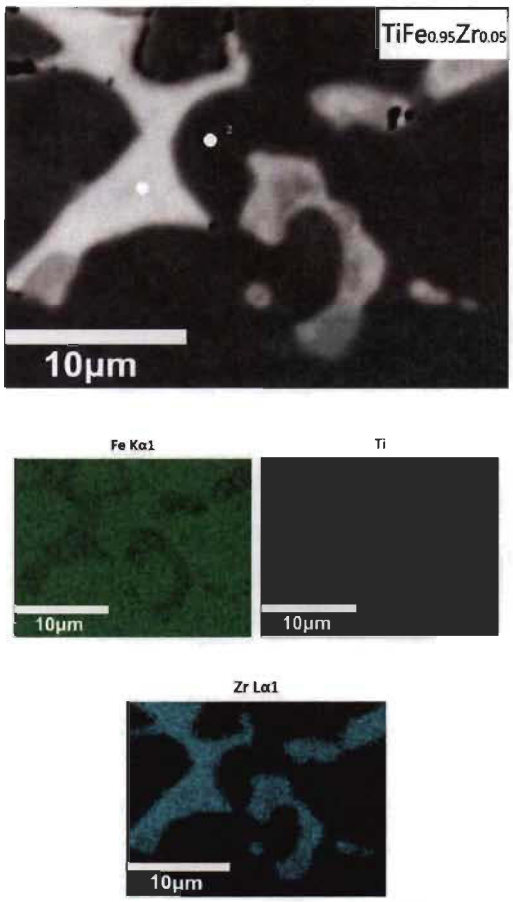

Fig. 3 – Backscattered electron micrograph of $TiFe_{0.95}Zr_{0.05}$ alloy prepared by arc melting with elements mapping.

Table 3 EDX analysis showing the dark phase (point 2) element composition of $Ti_{0.95}FeZr_{0.05}$, $TiFe_{0.95}Zr_{0.05}$ and $TiFeZr_{0.05}$ alloys.

Element	$Ti_{0.95}FeZr_{0.05}$	$TiFe_{0.95}Zr_{0.05}$	$TiFeZr_{0.05}$
Fe(at.%)	48.8	47.9	48.1
Ti(at.%)	50.8	51.5	51.3
Zr(at.%)	0.5	0.6	0.7

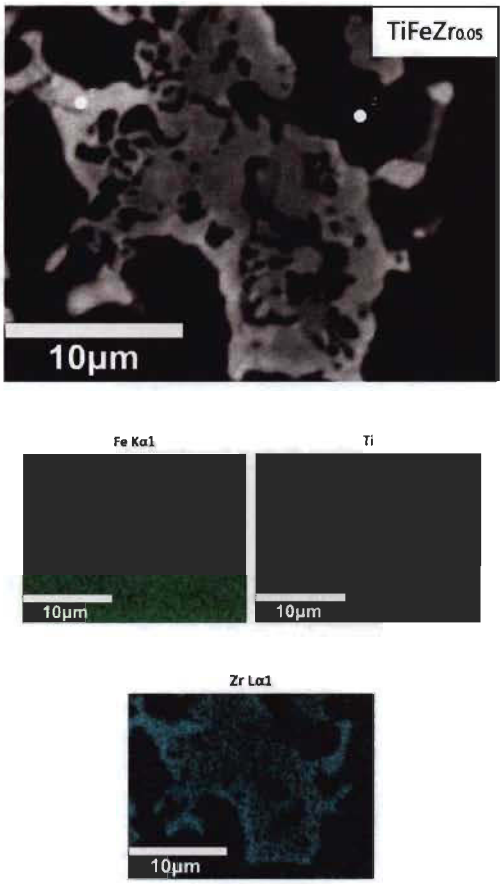

Fig. 4 – Backscattered electron micrograph of $TiFeZr_{0.05}$ alloys prepared by arc melting with elements mapping.

Table 4 EDX analysis showing the bright phase (point 1) element composition of $Ti_{0.95}FeZr_{0.05}$, $TiFe_{0.95}Zr_{0.05}$ and $TiFeZr_{0.05}$ alloys.

Element	$Ti_{0.95}FeZr_{0.05}$	$TiFe_{0.95}Zr_{0.05}$	$TiFeZr_{0.05}$
Fe(at.%)	47.8	36.3	47.4
Ti(at.%)	37.6	44.3	38.5
Zr(at.%)	14.6	19.4	14.0

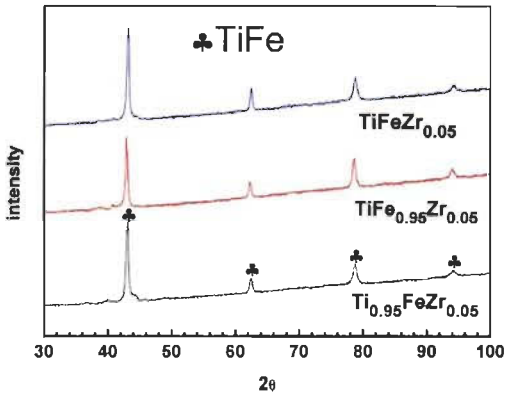

Fig. 5 – The XRD of $Ti_{0.95}FeZr_{0.05}$, $TiFe_{0.95}Zr_{0.05}$ and $TiFeZr_{0.05}$ alloys in as-cast state.

Table 4 indicates that zirconium is predominantly confined into the bright phase but actually, the bright phase is mainly composed of titanium and iron. A closer inspection reveals that the bright phase of $Ti_{0.95}FeZr_{0.05}$ and $TiFeZr_{0.05}$ alloys have almost the same composition. In fact, by comparing Tables 1 and 4 we see that those two alloys also have similar bright phase areas. In the case of $TiFe_{0.95}Zr_{0.05}$ the bright phase has a higher percentage of zirconium than the other two compositions but also a smaller area of bright phase. This agrees very well with the fact that zirconium is essentially found only in the bright phase. As all these compositions have the same amount of zirconium, if the concentration of zirconium is higher, then the area of the bright phase should be smaller. This is confirmed by Tables 1 and 4

Structural characterization

The XRD patterns of $Ti_{0.95}FeZr_{0.05}$, $TiFe_{0.95}Zr_{0.05}$ and $TiFeZr_{0.05}$ alloys in as-cast state are presented in Fig. 5. It can clearly be seen that all alloys prepared show TiFe phase. As the XRD was from a copper target the fluorescence from iron is strong and produces an important background which makes the detection of a secondary phase more difficult. Fluorescence is also the reason for the sloping background of all these patterns. The secondary phase may be associated to small broad peaks at around 37°, 40°, and 44°. These peaks match a crystal structure of $MgZn_2$ type. The relatively small amount of secondary phase and the broadness of the peaks makes the identification hard. A more detailed investigation of this secondary phase is underway.

Table 5 shows the lattice parameters of TiFe phase in as-cast alloys as determined from Rietveld analysis. The lattice

Table 5 Lattice parameter a (in A) of TiFe phase in as cast alloys as determined from Rietveld analysis.

Alloy	$Ti_{0.95}FeZr_{0.05}$	$TiFe_{0.95}Zr_{0.05}$	$TiFeZr_{0.05}$
Lattice parameter	2.9845(7)	2.9804(9)	2.9830(6)

parameters of $Ti_{0.95}FeZr_{0.05}$ and $TiFeZr_{0.05}$ are closer to each other than to $TiFe_{0.95}Zr_{0.05}$ but globally they differ by only 0.1%.

Activation kinetics

Fig. 6 shows the activation kinetics of all compositions as measured at room temperature under 2 MPa of hydrogen. It can be seen that $Ti_{0.95}FeZr_{0.05}$ alloy readily absorbs hydrogen without incubation time. Compositions $TiFe_{0.95}Zr_{0.05}$ and $TiFeZr_{0.05}$ have identical activation curves while $Ti_{0.95}FeZr_{0.05}$ has a faster activation kinetics than the two other alloys. This is somewhat surprising, considering the facts that $Ti_{0.95}FeZr_{0.05}$ and $TiFeZr_{0.05}$ have very similar secondary phase composition and abundance as well as an almost identical lattice parameter of their respective TiFe phase but still have different activation kinetics. The answer to this may be given by Fig. 1. This figure clearly shows that the bright phase distribution is much finer in $Ti_{0.95}FeZr_{0.05}$ alloy than the other two alloys. In addition, it also clearly shows that the fraction of interphase boundaries is higher in $Ti_{0.95}FeZr_{0.05}$ than that in $TiFeZr_{0.05}$. Therefore, under the hypothesis that the bright phase and interphase boundaries act as a gateway for hydrogen. It is natural that the hydrogenation kinetics will be faster for this alloy. This shows that the alloy microstructure plays an important role in the activation kinetics.

Pressure-composition isotherms

After the first hydrogenation cycle, the pressure-composition isotherms were measured at room temperature. The measured isotherms are shown in Fig. 7. The compositions $TiFeZr_{0.05}$ and $Ti_{0.95}FeZr_{0.05}$ present essentially the same curve, the only small difference being that the alloy $TiFeZr_{0.05}$ has a slightly bigger capacity. The alloy $TiFe_{0.95}Zr_{0.05}$ has a higher capacity than the two other alloys and its hydrides are more stable as indicated by the lower plateau pressures. Moreover, this higher capacity is mainly due to the lower plateau pressure (monohydride) while the dihydride capacity is the same for the three alloys.

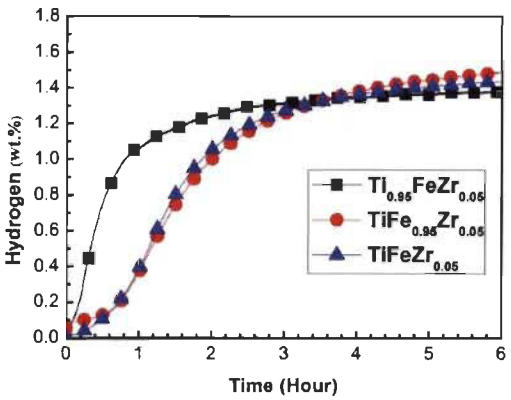

Fig. 6 – The activation behaviour of $Ti_{0.95}FeZr_{0.05}$, $TiFe_{0.95}Zr_{0.05}$ and $TiFeZr_{0.05}$ alloys at room temperature under 2 MPa hydrogen pressure.

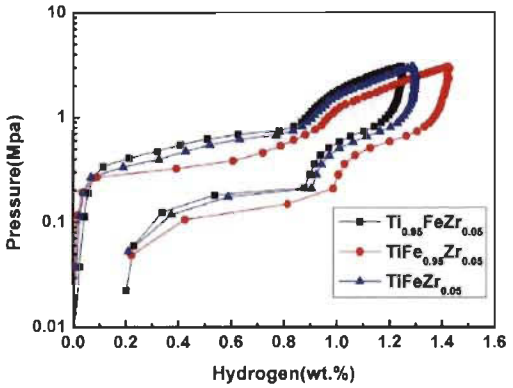

Fig. 7 – Pressure-composition isotherms of $Ti_{0.95}FeZr_{0.05}$, $TiFe_{0.95}Zr_{0.05}$ and $TiFeZr_{0.05}$ alloys at room temperature.

Conclusion

The microstructure, crystal structure, and hydrogenation characteristics of $Ti_{0.95}FeZr_{0.05}$, $TiFe_{0.95}Zr_{0.05}$ and $TiFeZr_{0.05}$ alloys has been investigated. The following observations have been made. Compared to $TiFe_{0.95}Zr_{0.05}$ alloy, $Ti_{0.95}FeZr_{0.05}$ and $TiFeZr_{0.05}$ alloys have similar bright phase compositions and areas and closer lattice parameters. But for all alloys zirconium is mainly located in the bright phase.

(1) $Ti_{0.95}FeZr_{0.05}$ alloy has a faster activation kinetics than the two other alloys due to the very fine distribution of the bright secondary phase.
(2) $TiFeZr_{0.05}$ and $Ti_{0.95}FeZr_{0.05}$ alloys show a similar curve of pressure-composition isotherm, but the former has a slightly bigger capacity. In addition, $TiFe_{0.95}Zr_{0.05}$ alloy shows the highest hydrogen capacity.

Crystallite size of dark and bright phase could also play a role. However, for this particular investigation as the secondary phase was difficult to see by X-ray diffraction a complete discussion about the role of crystallite size is challenging. We are planning to perform neutron and synchrotron experiments in order to have a better characterization of the crystal structure of these alloys. The results of the present investigation show that a very slight variation of composition could have an important effect of microstructure of the alloy and its hydrogen storage behaviours.

Acknowledgements

Peng Lv is thankful to Fonds de recherche du Quebec-Nature et technologies (FRQNT) for fellowship. We would also thank Mrs. A. Lejeune for SEM analysis and C. Gosselin for help in experiment.

REFERENCES

[1] Reilly JJ, Wiswall JRH. Iron titanium manganase alloy hydrogen storage. Google Patents. 1975.

[2] Schober T, Westlake DG. The activation of FeTi for hydrogen storage: a different view. Scr Metall 1981;15:913–8.

[3] Chiang C-H, Chin Z-H, Perng T-P. Hydrogenation of TiFe by high-energy ball milling. J alloys Compd 2000;307:259–65.

[4] Schober T. On the activation of FeTi for hydrogen storage. J Less Common Metals 1983;89:63–70.

[5] Reilly J, Wiswall Jr R. Formation and properties of iron titanium hydride. Inorg Chem 1974;13:218–22.

[6] Lee S-M, Perng T-P. Effect of the second phase on the initiation of hydrogenation of $TiFe_{1-x}M_x$ (M = Cr, Mn) alloys. Int J hydrogen energy 1994;19:259–63.

[7] Miyamura H, Sakai T, Kuriyama N, Tanaka H, Uehara I, Ishikawa H. Hydrogenation and phase structure of Ti–Fe–V alloys. J Alloys Compd 1997;253:232–4.

[8] Edalati K, Matsuda J, Iwaoka H, Toh S, Akiba E, Horita Z. High-pressure torsion of TiFe intermetallics for activation of hydrogen storage at room temperature with heterogeneous nanostructure. Int J Hydrogen Energy 2013;38:4622–7.

[9] Shenzhong Y, Rong Y, Tiesheng H, Shilong Z, Bingzhao C. A study of the activation of FeTi and $Fe_{0.9}TiMn_{0.1}$. Int J Hydrogen Energy 1988;13:433–7.

[10] Nishimiya N, Wada T, Matsumoto A, Tsutsumi K. Hydriding characteristics of zirconium-substituted FeTi. J Alloys Compd 2000;313:53–8.

[11] Jain P, Gosselin C, Huot J. Effect of Zr, Ni and Zr_7Ni_{10} alloy on hydrogen storage characteristics of TiFe alloy. Int J Hydrogen Energy 2015;40:16921–7.

[12] Zadorozhnyy V, Klyamkin S, Zadorozhnyy M, Bermesheva O, Kaloshkin S. Hydrogen storage nanocrystalline TiFe intermetallic compound: synthesis by mechanical alloying and compacting. Int J Hydrogen Energy 2012;37:17131–6.

[13] Emami H, Edalati K, Matsuda J, Akiba E, Horita Z. Hydrogen storage performance of TiFe after processing by ball milling. Acta Mater 2015;88:190–5.

[14] Gosselin C, Huot J. Hydrogenation properties of TiFe doped with zirconium. Materials 2015;8:7864–72.

[15] Lutterotti L, Bortolotti M. Object oriented programming and fast computation techniques in MAUD, a program for powder diffraction analysis written in java. IUCr Compcomm Newsl 2003;1:43–50.

[16] Lutterotti L, Matthies S, Wenk H. MAUD: a friendly Java program for material analysis using diffraction. IUCr Newsl CPD 1999;21.

[17] Abràmoff MD, Magalhães PJ, Ram SJ. Image processing with ImageJ. Biophot Int 2004;11:36–42.

[18] Collins TJ. ImageJ for microscopy. Biotechniques 2007;43:25–30.

Article 2

Hydrogenation improvement of TiFe by adding $ZrMn_2$

PengLv, Jacques Huot*

Hydrogen Research Institute, Université du Québec à Trois-Rivières, 3351 des Forges, Trois-Rivières ,G9A 5H7, Canada

Abstract: In this paper, we report the microstructure and hydrogen storage properties of TiFe+x wt.%$ZrMn_2$ (x=2, 4, 8, 12) alloys prepared by arc melting. Each alloy was made of two phases: a TiFe phase with very small amount of zirconium and manganese, and a second phase which has a higher proportion of zirconium and manganese. We found that the first hydrogenation kinetics increase with x. This is most likely due to the presence of zirconium-rich secondary phase that acts as a gateway for hydrogen to enter the main TiFe phase. Pressure-composition isotherms also show that increasing x decreases the absorption plateau pressure. Moreover, for x=12, air exposure had a minimal impact on hydrogen absorption behaviour. Finally, we found that cold rolling has minimal effect on the activation kinetics of TiFe+x wt.%$ZrMn_2$ (x=4) alloy.

Keywords: TiFe alloy; Activation; Hydrogen storage properties; Air exposure; Cold rolling

Energy 138 (2017) 375–382

Contents lists available at ScienceDirect

Energy

journal homepage: www.elsevier.com/locate/energy

Hydrogenation improvement of TiFe by adding $ZrMn_2$

Peng Lv, Jacques Huot*

Hydrogen Research Institute, Université du Québec à Trois-Rivières, 3351 des Forges, Trois-Rivières, G9A 5H7, Canada

ARTICLE INFO

Article history:
Received 23 December 2016
Received in revised form
28 May 2017
Accepted 11 July 2017
Available online 12 July 2017

Keywords:
TiFe alloy
Activation
Hydrogen storage properties
Air exposure
Cold rolling

ABSTRACT

In this paper, we report the microstructure and hydrogen storage properties of TiFe + x wt.%$ZrMn_2$ (x = 2, 4, 8, 12) alloys prepared by arc melting. Each alloy was made of two phases: a TiFe phase with very small amount of zirconium and manganese, and a second phase which has a higher proportion of zirconium and manganese. We found that the first hydrogenation kinetics increase with x. This is most likely due to the presence of zirconium-rich secondary phase that acts as a gateway for hydrogen to enter the main TiFe phase. Pressure-composition isotherms also show that increasing x decreases the absorption plateau pressure. Moreover, for x = 12, air exposure had a minimal impact on hydrogen absorption behaviour. Finally, we found that cold rolling has minimal effect on the activation kinetics of TiFe + x wt.%$ZrMn_2$ (x = 4) alloy.

1. Introduction

Hydrogen is considered to be a clean energy vector for the future. However, its widespread use depends on ways to store it in a safe, efficient and inexpensive way. Presently the main ways to store hydrogen are gaseous and liquid. Nonetheless these two methods could not be efficiently used for many applications because of the high pressure involved in gaseous storage or the low temperature of liquid hydrogen. An attractive alternative is to use metal hydrides. In metal hydride hydrogen forms a chemical bond with the metal atoms in an alloy. This reaction is schematically shown in Equation (1) where M indicates a metallic atom and Q is the heat of the reaction.

$$M + H_2 \leftrightarrow MH_2 + Q \quad (1)$$

This reaction is reversible under specific temperature and pressure depending on the nature of the alloy. Utilization of metal hydrides is not restricted to hydrogen storage, they could be used for heat storage [1], hydrogen generation [2], or a the negative electrode in Ni-MH batteries [3]. There are many types of metal hydrides, differing by their temperature and pressure of the reaction as well as their hydrogen capacities (mass of hydrogen per mass of alloy). The alloy TiFe is a well-known metal hydride that could store hydrogen near-room temperature and under a few bars of hydrogen [4,5]. However, one problem of TiFe alloy, as well as many other metal hydrides, is that the first hydrogenation (activation) is a slow and difficult process. However, this limits the use of TiFe in practical applications because of the needs of high pressure and temperature for activation which in turns, increases the hydride cost [4,5]. For example, Reilly et al. indicated that, in order to absorb hydrogen, as-cast pure TiFe alloy need to be cycled between around 400 °C and room temperature and exposed to 6.5 MPa of hydrogen [6]. Therefore, there is a real need to find a way to improve the conditions of first hydrogenation of TiFe alloys. Generally, one of the ways to improve the first hydrogenation of TiFe alloy is to add some elements like transition metals and rare-earth metals [7,8]. Another way is by preparing an ultra-fine microstructure. Different methods have been applied to produce such microstructure. They include melt spinning [9,10], ball milling [11,12], cold rolling [13] and high pressure torsion [13,14].

In a previous investigation, we have demonstrated that the first hydrogenation of TiFe alloy could be improved by adding Zr_7Ni_{10} [15], Zr [10,16] and Mn [17]. The good effect of Zr and Mn lead us to investigate the alloy $ZrMn_2$ as an addition to TiFe alloy. In this paper we report the investigation of the effects of different $ZrMn_2$ content on the microstructure, hydrogen storage properties and air resistance of TiFe alloy.

2. Experimental

Fe (99.9%), Ti (99.9%), Zr (99.5%) and Mn (99.5%) were purchased from Alfa Aesar and used without further purification. TiFe + x wt.%

* Corresponding author.
E-mail addresses: penglv928@gmail.com (P. Lv), jacques.huot@uqtr.ca (J. Huot).

http://dx.doi.org/10.1016/j.energy.2017.07.072
0360-5442/

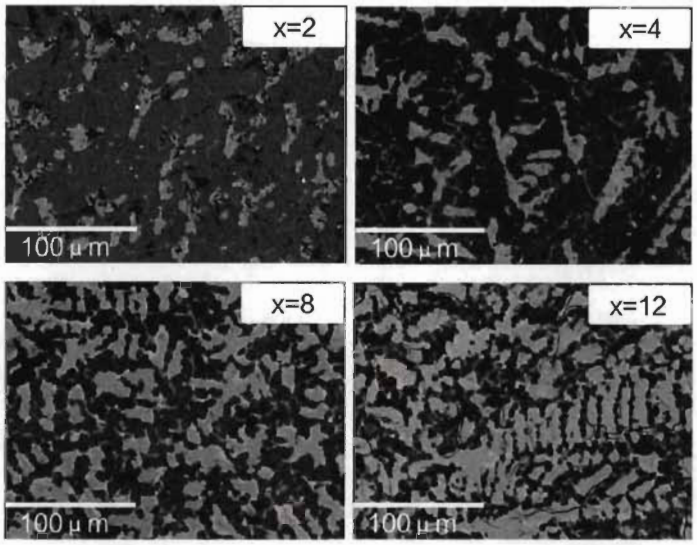

Fig. 1. Backscattered electron micrographs of arc melted TiFe + x wt.%$ZrMn_2$ (x = 2, 4, 8, 12) alloys.

Table 1
Percentage of bright and dark phases area in as-cast TiFe + x wt.%$ZrMn_2$ (x = 2, 4, 8, 12) alloys shown in Fig. 1.

Phase	x = 2	x = 4	x = 8	x = 12
Bright (%)	18	21	38	48
Dark (%)	82	79	62	52

$ZrMn_2$ (x = 2, 4, 8, 12) alloys were prepared by arc melting in argon atmosphere. In order to get homogeneity each pellet was melted and turned over three times. Cold rolling was done in air using a Durston DRM 100 rolling mill.

The crystal structure was determined by X-ray diffraction (XRD; Bruker D8 Focus; Cu Kα radiation). Lattice parameters were evaluated from Rietveld's method using TOPAS software [18,19]. Morphology and chemical analysis were investigated by using a JEOL JSM-5500 scanning electron microscopy equipped with an EDX (Energy Dispersive X-ray) apparatus. The areas of different phases were analyzed by image J software [20,21]. The hydrogen storage properties were measured using a homemade Sieverts-type apparatus. The experimental error on the hydrogen content measured in wt.% (mass of hydrogen over mass of metal) was evaluated as 0.05 wt%.

3. Results and discussion

3.1. Morphology

Fig. 1 shows secondary electron micrographs of TiFe + x wt.% $ZrMn_2$ (x = 2, 4, 8, 12) alloys prepared by arc melting. We can see that these samples exhibit different microstructure which includes bright and dark phases. Using image J software, the proportion of bright and dark phases surfaces are reported in Table 1. From Table 1 and Fig. 1 we see that the bright phase area increases with x, reaching almost 50% for x = 12 wt%$ZrMn_2$.

It is clear from Fig. 1 that all alloys are formed of at least two different phases. Using EDX, the bulk atomic abundance was measured and compared to the nominal composition. The results,

Table 3
EDX analysis of the bright phase (point 1) of TiFe + x wt.%$ZrMn_2$ (x = 2, 4, 8, 12) alloys.

Element (Atomic%)	x = 2	x = 4	x = 8	x = 12
Fe	57.0 ± 0.2	54.5 ± 0.3	53.9 ± 0.3	51.4 ± 0.3
Ti	40.6 ± 0.3	39.7 ± 0.3	39.0 ± 0.2	38.1 ± 0.3
Mn	1.7 ± 0.1	3.3 ± 0.1	4.5 ± 0.2	6.7 ± 0.2
Zr	0.7 ± 0.1	2.4 ± 0.1	2.6 ± 0.1	3.8 ± 0.1

Table 2
Nominal and measured bulk atomic abundance of TiFe + x wt.%$ZrMn_2$ (x = 2, 4, 8, 12) alloys.

Sample		Ti(Atomic%)	Fe(Atomic%)	Zr(Atomic%)	Mn(Atomic%)
x = 2	Nominal composition	49.2	49.2	0.5	1.0
	Measured	48.7	49.6	0.6	1.1
x = 4	Nominal composition	48.5	48.5	1.0	2.0
	Measured	48.8	47.8	1.2	2.1
x = 8	Nominal composition	47.0	46.6	2.0	4.0
	Measured	47.3	49.7	2.4	3.8
x = 12	Nominal composition	45.8	45.8	2.8	5.6
	Measured	45.9	45.4	3.3	5.4

Table 4
EDX analysis of the dark phase (point 2) of TiFe + x wt.%$ZrMn_2$ (x = 2, 4, 8, 12) alloys.

Element (Atomic%)	x = 2	x = 4	x = 8	x = 12
Fe	49.2 ± 0.2	47.7 ± 0.3	46.9 ± 0.2	45.9 ± 0.3
Ti	50.1 ± 0.3	50.5 ± 0.3	50.5 ± 0.3	50.3 ± 0.3
Mn	0.7 ± 0.1	1.5 ± 0.1	2.3 ± 0.1	3.4 ± 0.2
Zr	0.0	0.3 ± 0.1	0.3 ± 0.1	0.5 ± 0.1

shown in Table 2, prove that the atomic abundances of all elements are very close to the nominal composition.

The chemical composition of individual phases was thereafter investigated for each value of x. For each composition an elemental mapping was performed as well as a point analysis. For all compositions, point 1 identify the bright phase and point 2 the dark phase. The quantitative analysis of points 1 and 2 are reported in Tables 3 and 4 respectively.

The microstructure and element mapping of x = 2 are shown in Fig. 2. It shows that iron and titanium are well distributed in both phases. Magnesium is also evenly spread while zirconium is clearly more abundant in the bright phase. This was confirmed by the quantitative analysis of points 1 and 2 reported in Tables 3 and 4. We see that the dark phase (point 2) has a composition very close to TiFe with only a small amount of manganese and effectively no zirconium. Bright phase composition (point 1) indicates that almost all zirconium and manganese are located in the bright phase. However, the bright phase is still mainly formed by iron and titanium.

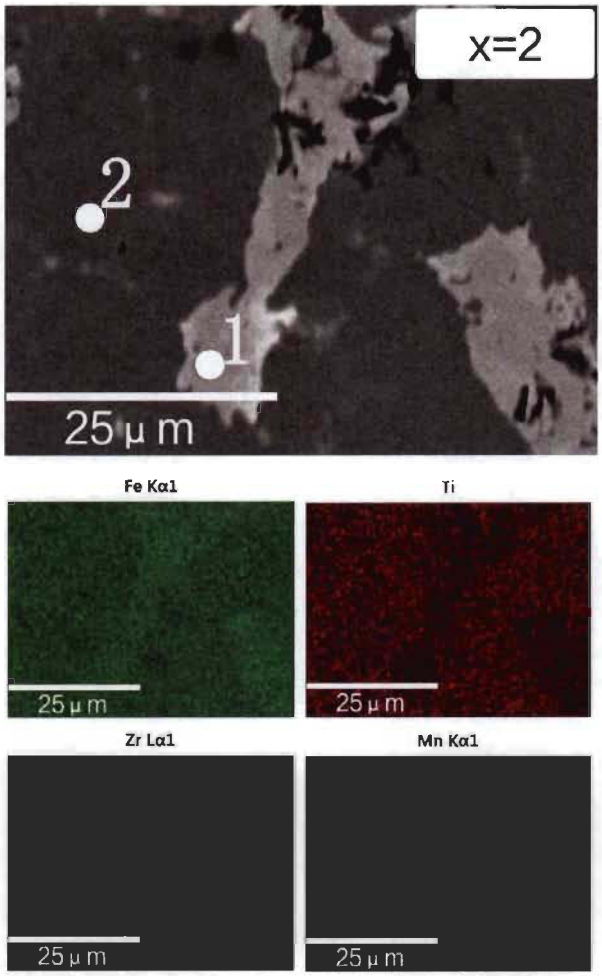

Fig. 2. Backscattered electron micrograph of arc melted TiFe+2 wt%$ZrMn_2$ alloy with EDX mapping and chemical composition at different sites.

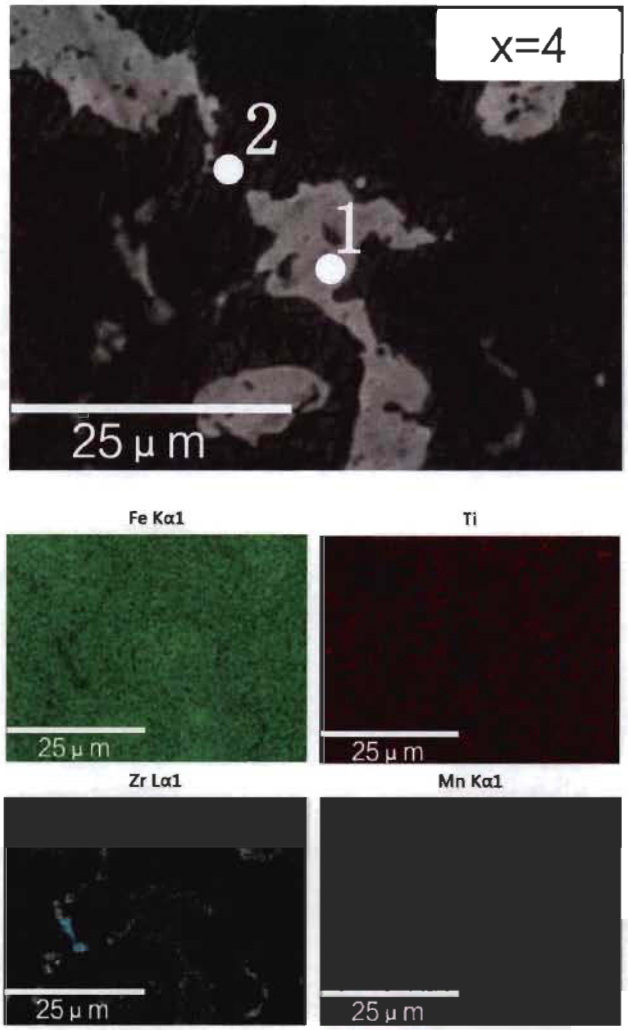

Fig. 3. Backscattered electron micrograph of arc melted TiFe+4 wt%$ZrMn_2$ alloy with EDX mapping and chemical composition at different sites.

Fig. 3 shows the micrograph and element mapping for x = 4. As for the previous composition, we found that manganese, iron and titanium seem to be evenly distributed. However, the point analysis reported in Tables 3 and 4 shows that, compared to x = 2, the dark phase has a slight reduction of iron content accompanied by a small increase on manganese. In the case of the bright phase, iron composition decreased but the main fact is that manganese and zirconium contents increased by about 1.7 wt% for each element.

Fig. 4 presents the micrograph and element mapping for x = 8. The situation is similar to the previous two cases but here the mapping suggests that the zirconium content in the secondary phase is higher. This is confirmed by the point analysis results presented in Tables 3 and 4. On the other hand, in the TiFe phase the iron content slightly decreased and the manganese content increased while the titanium and zirconium contents almost did not change.

Fig. 5 shows the micrograph and element mapping for x = 12. It is clear that the bright phase occupies a much larger area than in the previous compositions. Also, it should be noticed that the zirconium abundance seems to be higher on the edge of the bright areas. In the dark phase, the proportion of titanium and zirconium did not change compared to x = 8 but the amount of manganese increased and the amount of iron decreased in the same proportions.

From Tables 3 and 4, we could now draw general conclusions on the evolution of chemical compositions in the dark and bright phase as x increases. In the case of the dark phase it has an almost

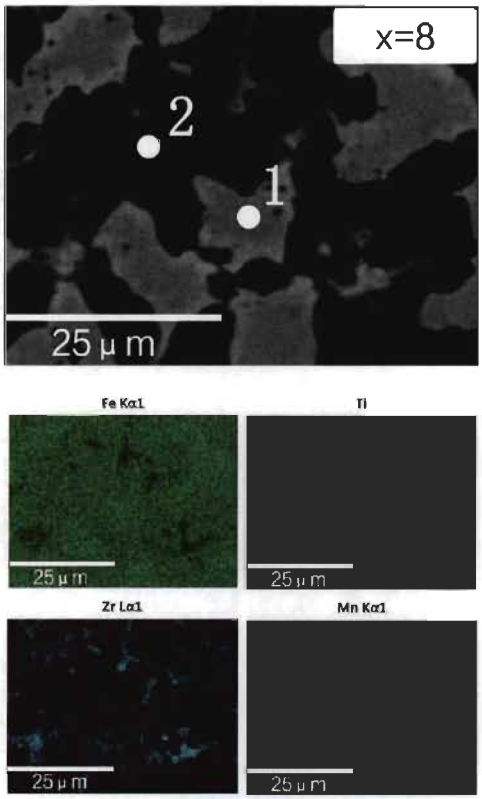

Fig. 4. Backscattered electron micrograph of arc melted TiFe+8 wt%$ZrMn_2$ alloy with EDX mapping and chemical composition at different sites.

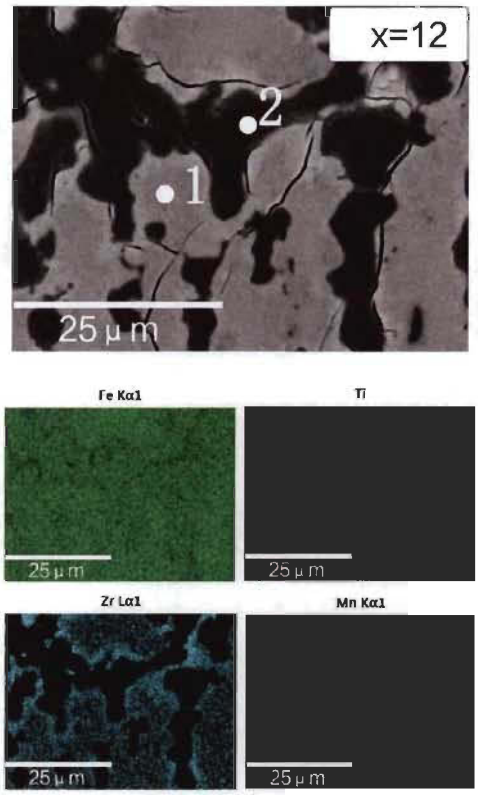

Fig. 5. Backscattered electron micrograph of arc melted TiFe + 12 wt%$ZrMn_2$ alloy with EDX mapping and chemical composition at different sites.

perfect TiFe composition for x = 2 with only a small amount of manganese substituting with iron. When x increases, the titanium proportion stays the same and manganese substitute in greater proportion with iron. Zirconium is present in only small concentration and does not increase with x. The behaviour is different for the secondary phase. When x increases the proportion of titanium and iron decrease but the rate is more important for iron than for titanium. Zirconium and manganese proportion both increases with x but the rate is bigger for manganese. In fact, the proportion of iron plus zirconium and titanium plus manganese are stable when x increases, suggesting that in the bright phase zirconium substitute with iron and manganese substitute with titanium. This means that different substitutions schemes are present in the bright and dark phases.

3.2. Crystal structure characterization

The XRD patterns of the TiFe + x wt.%$ZrMn_2$ (x = 2, 4, 8, 12) alloys in as-cast state are presented in Fig. 6. It can clearly be seen that all alloys prepared show TiFe phase, but there are small peaks at around 37°, 40°, 44° that most probably are associated with the secondary phases seen in the SEM micrographs. As the XRD was

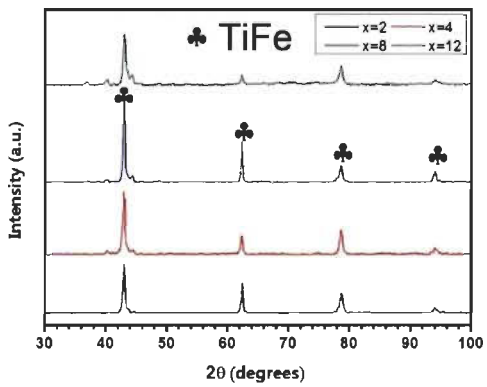

Fig. 6. Powder diffraction patterns of as-cast alloys TiFe + x wt.% $ZrMn_2$ (x = 2, 4, 8, 12).

Table 5
Lattice parameters a (in Å) of TiFe phase in as cast TiFe + x wt.%$ZrMn_2$ (x = 2, 4, 8, 12) alloys as determined by Rietveld analysis. Number in parenthesis is the error on the last significant digit.

Phase	x = 2	x = 4	x = 8	x = 12
Lattice parameter	2.9796 (3)	2.9798 (3)	2.9796 (3)	2.9856 (7)

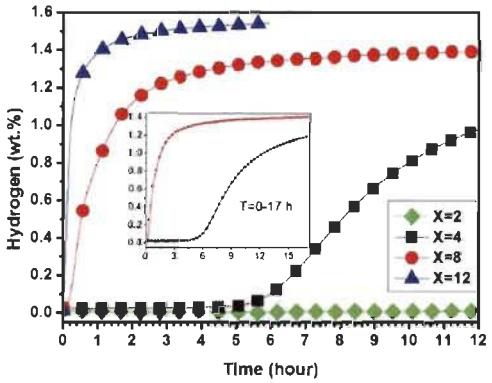

Fig. 7. First hydrogenation curves of TiFe + x wt.% $ZrMn_2$ (x = 2, 4, 8, 12) alloys at room temperature under 3 MPa hydrogen pressure. Hydrogen capacity is given in weight % (hydrogen mass/mass of alloy).

from a copper target, the fluorescence from iron is strong and produces an important background which makes the detection of a secondary phase more difficult. By inspection, we noticed that these peaks match a crystal structure of $MgZn_2$ type. But the relatively small amount of secondary phase and the broadness of the peaks make a definitive identification impossible.

Table 5 shows the lattice parameters (in Å) of TiFe phase in as-cast TiFe + x wt.%$ZrMn_2$ (x = 2, 4, 8, 12) alloys as determined by Rietveld's analysis. It can be seen that the lattice parameter of TiFe phase increase with x.

3.3. First hydrogenation

Fig. 7 shows the first hydrogenation of TiFe + x wt.%$ZrMn_2$ (x = 2, 4, 8, 12) alloys performed under an initial hydrogen pressure of 3 MPa and at room temperature. It can be seen that x = 2 didn't absorb the hydrogen even after 12 h. The incubation time for x = 4 is about 4.5 h. For x = 8 and 12, the alloys show no incubation time and directly absorb hydrogen. The reaction kinetics of the first hydrogenation increases with x. As the composition of TiFe phase does not drastically change when x increases we could safely conclude that activation kinetics is due to the secondary phase. Fig. 1 clearly shows that the bright phase is more abundant and better distributed in the x = 12 alloy than the other three alloys. This indicates that the microstructure plays an important role in the first hydrogenation. In addition, it can be seen that the fraction of interphase boundaries increases with x. Therefore, the bright phase may act as a gateway for the hydrogen.

3.4. Pressure-composition isotherms

After the first hydrogenation cycle, the pressure-composition isotherm of the samples (x = 4, 8, 12) were measured at room temperature and are shown in Fig. 8. Prior to the measurement, the samples were kept under vacuum for 1 h at room temperature. For each curve, the upper part is the absorption process while the lower part is the desorption process. We see that the absorption plateau pressure decreases from x = 4 to 12. However the desorption plateau pressure is essentially at the same pressure. This means that adding $ZrMn_2$ did not change the thermodynamics of dehydrogenation but reduced the hysteresis. Also, the reversible capacity seems to increase with increasing x but it is lower than those measured during the first hydrogenation. A possible reason for the lower reversible capacities might form some mono hydrides which cannot dehydrogenate after the first hydrogenation [22].

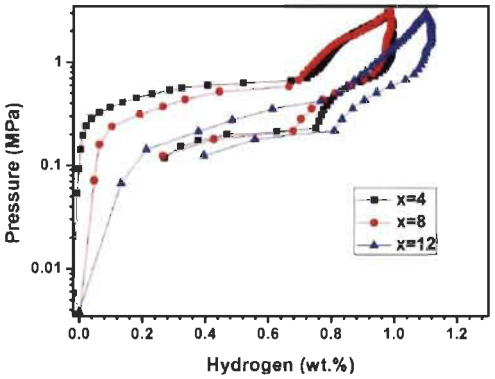

Fig. 8. Pressure-composition isotherms of TiFe + x wt.%$ZrMn_2$ (x = 4, 8, 12) alloys at room temperature. The highest pressure is 3 MPa for the absorption and the lowest pressure is 0.1 MPa for the desorption.

3.5. Air exposure

The possibility to expose as-cast alloys to the air before first hydrogenation could greatly reduce the synthesis complexity and

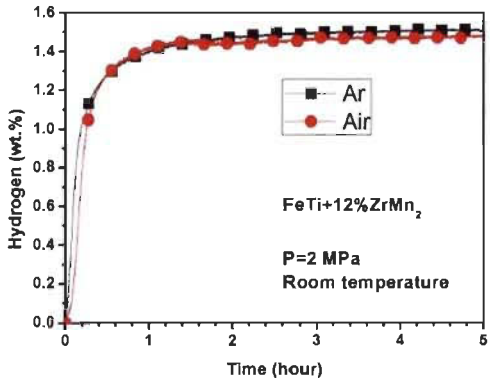

Fig. 9. The first hydrogenation of TiFe + 12 wt%$ZrMn_2$ alloys at room temperature under 2 MPa hydrogen pressure. The sample labelled Ar was crushed into a glove box and never exposed to the air. Sample labelled Air was crushed and handled in air. Hydrogen capacity is given in weight % (hydrogen mass/mass of alloy).

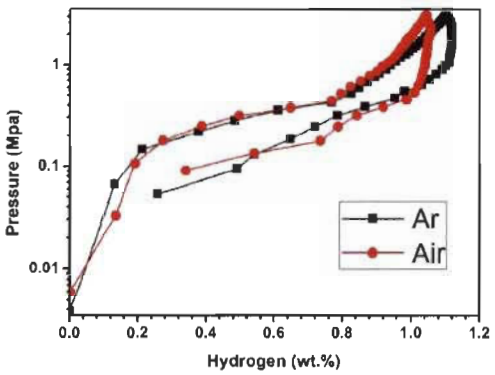

Fig. 10. Pressure-composition isotherms of TiFe + 12 wt%$ZrMn_2$ alloys for a sample handled in air and another one handled in argon protective atmosphere.

cost. Therefore, we investigated the effect of air exposure on our as-cast alloys by preparing two identical samples of composition TiFe + 12 wt%$ZrMn_2$. One sample was processed in air, the other one in an argon-filled glove box. The first hydrogenation was measured under an initial hydrogen pressure of 2 MPa at room temperature. Activation curves are shown in Fig. 9. Remarkably, the air exposed sample has the same activation kinetics as the sample handled under argon. These results indicate that the TiFe + 12 wt%$ZrMn_2$ alloy could be handled in air without detrimental effects in the activation behaviour.

In order to compare the effect of the air and argon on the reversible capacity of TiFe + 12 wt%$ZrMn_2$ alloy, the pressure composition isotherm at room temperature was measured. Fig. 10 clearly shows that the absorption and desorption plateau pressures are not modified by air exposure. However, the reversible capacity was slightly reduced.

3.6. Improving activation by cold rolling

The activation kinetics shown in Fig. 7 indicated that an incubation time is present for x = 2 and x = 4. In a previous investigation, we have shown that cold rolling is very effective to enhance activation of $LaNi_5$ alloy [23]. This led us to use cold rolling on the as-cast material to see if there is any activation kinetic improvement. Cold rolling was done in air for one and five rolling passes. Fig. 11 shows the first hydrogenation of TiFe + x wt.%$ZrMn_2$ (x = 2, 4, 8, 12) alloys in as cast and after cold rolling. For x = 8 and x = 12 the curves levelled off after two hours. In order to have a better view of the kinetics we only plotted the first two hours. We see that cold rolling has clear beneficial effect only for the x = 4 where rolling reduces the incubation time. In the case of x = 8 the effect was more limited. Thus cold rolling could reduce incubation time but the main factor to enhance activation is by adding $ZrMn_2$ alloy.

4. Conclusion

The hydrogenation of TiFe + x wt.%$ZrMn_2$ (x = 2, 4, 8, 12) alloys have been investigated. It was found that the as-cast alloys are multiphases with a main phase having the TiFe structure and a zirconium and manganese-rich secondary phase. The amount of secondary phase increases with the amount of $ZrMn_2$ additive.

The first hydrogenation kinetics and capacities of TiFe + x wt.% $ZrMn_2$ (x = 2, 4, 8, 12) alloys increases with the amount of $ZrMn_2$ due to the very fine distribution of the secondary phase. This secondary phase most probably is acting as a gateway for hydrogen to enter the main TiFe phase and this is why a fine distribution gives fast first hydrogenation. It would be interesting to find the rate-

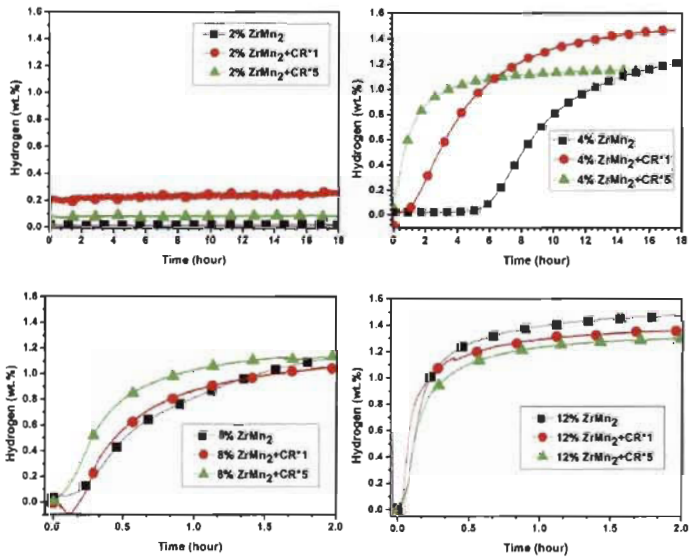

Fig. 11. First hydrogenation of as-cast and cold rolled TiFe + x wt.% $ZrMn_2$ (x = 2, 4, 8, 12) alloys. Hydrogenation performed at room temperature under 2 MPa of hydrogen. Hydrogen capacity is given in weight % (hydrogen mass/mass of alloy).

limiting step of the activation and find the proper kinetic model. However, the problem with activation is that this kinetic only appears on the first hydrogenation. The subsequent hydrogenations have a totally different kinetic curves and thus a different rate-limiting steps. Preliminary investigation leads to a strong contribution of particle size but also to the microstructure distribution within the alloy. A detailed analysis for the activation rate-limiting step is underway.

Air exposure was shown to have minimal effect on the hydrogen absorbing properties of TiFe + 12 wt%$ZrMn_2$ alloy. This is important for industrial applications as the need to work under inert atmosphere greatly increase production costs. We also found that cold rolling has minimal effect on the first hydrogenation. This leads to the conclusion that alloy composition and microstructure have a much bigger impact on the activation behaviour than mechanical treatment.

Acknowledgements

Peng Lv is thankful to Fonds de recherche du Quebec-Nature et technologies (FRQNT) for a PBEEE fellowship. We would also thank Mrs. A. Lejeune for SEM analysis, C. Gosselin and ZH. Zhang for help in the experiment.

References

[1] Paskevicius M, Sheppard D, Williamson K, Buckley C. Metal hydride thermal heat storage prototype for concentrating solar thermal power. Energy 2015;88:469–77.
[2] Liu Y, Wang X, Liu H, Dong Z, Cao G, Yan M. Hydrogen generation from Mg–LiBH 4 hydrolysis improved by AlCl 3 addition. Energy 2014;68:548–54.
[3] Kang J, Yan F, Zhang P, Du C. Comparison of comprehensive properties of Ni-MH (nickel-metal hydride) and Li-ion (lithium-ion) batteries in terms of energy efficiency. Energy 2014;70:618–25.
[4] Schober T, Westlake D. The activation of FeTi for hydrogen storage: a different view. Scr Metall 1981;15:913–8.
[5] Khatamian D, Weatherly G, Manchester F. Some effects of activation for hydrogen absorption in FeTi powder. Acta Metall 1983;31:1771–80.
[6] Reilly JJ, Wiswall RH. Formation and properties of iron titanium hydride. Inorg Chem 1974;13:218–22.
[7] Mitrokhin S, Verbetsky V, Kajumov R, Cunmao H, Yufen Z. Hydrogen sorption peculiarities in FeTi-type Ti Fe V Mn alloys. J Alloy. Compd 1993;199:155–60.
[8] Lee S-M, Perng T-P. Effect of the second phase on the initiation of hydrogenation of TiFe1 − xMx (M= Cr, Mn) alloys. Int J hydrogen energy 1994;19:259–63.
[9] Lv P, Wang Z, Zhou H, Deng J, Yao Q, Zhang H. Effect of Co substitution for La on hydrogen storage properties and thermal stabilities of amorphous Mg60Ni30La10 − xCox (x= 0, 2 and 4) alloys prepared by melt spinning. Mater Sci Technol 2014;30:176–82.
[10] Lv P, Huot J. Hydrogen storage properties of Ti 0.95 FeZr 0.05, TiFe 0.95 Zr 0.05 and TiFeZr 0.05 alloys. Int J Hydrogen Energy 2016;41:22128–33.
[11] Dewa MDK, Wiryolukito S, Suwarno H. Hydrogen absorption capacity of Fe-Ti-Al alloy prepared by high energy ball milling. Energy Procedia 2015;68:318–25.
[12] Chiang C-H, Chin Z-H, Perng T-P. Hydrogenation of TiFe by high-energy ball milling. J Alloy. Compd 2000;307:259–65.
[13] Edalati K, Matsuda J, Yanagida A, Akiba E, Horita Z. Activation of TiFe for hydrogen storage by plastic deformation using groove rolling and high-pressure torsion: similarities and differences. Int J hydrogen energy 2014;39:15589–94.
[14] Edalati K, Matsuda J, Iwaoka H, Toh S, Akiba E, Horita Z. High-pressure torsion of TiFe intermetallics for activation of hydrogen storage at room temperature with heterogeneous nanostructure. Int J Hydrogen Energy 2013;38:4622–7.
[15] Jain P, Gosselin C, Huot J. Effect of Zr, Ni and Zr 7 Ni 10 alloy on hydrogen storage characteristics of TiFe alloy. Int J Hydrogen Energy 2015;40:16921–7.
[16] Gosselin C, Huot J. Hydrogenation properties of TiFe doped with zirconium. Materials 2015;8:7864–72.
[17] Miller H, Murray J, Laury E, Reinhardt J, Goudy A. The hydriding and dehydriding kinetics of FeTi and Fe0. 9TiMn0. 1. J Alloy. Compd 1995;231:670–4.
[18] Coelho AA. Topas-academic. A computer programme for rietveld analysis. 2004.
[19] Bruker A. TOPAS V3: general profile and structure analysis software for powder diffraction data. Karlsruhe, Germany: User's Manual, Bruker AXS; 2005.
[20] Collins T. ImageJ for microscopy. BioTechniques 2007;43:S25–30. http://dx doi org/102144/000112517.
[21] Abràmoff MD, Magalhães PJ, Ram SJ. Image processing with ImageJ. Biophot Int 2004;11:36–42.
[22] Nishimiya N, Wada T, Matsumoto A, Tsutsumi K. Hydriding characteristics of zirconium-substituted FeTi. J Alloy. Compd 2000;313:53–8.
[23] Tousignant M, Huot J. Hydrogen sorption enhancement in cold rolled LaNi 5. J Alloy. Compd 2014;595:22–7.

Article 3

Effect of ball milling and cryomiling on the microstructure and first hydrogenation properties of TiFe alloy doped with 4 wt.% Zr as additive

Peng Lv1, Matylda N. Guzik[2], Sabrina Sarori[2], Jacques Huot[1*]

1.Hydrogen Research Institute, Université du Québec à Trois-Rivières, 3351 des Forges, Trois-Rivières , G9A 5H7, Canada

2.Department of Technology Systems, University of Oslo, Forskningsparken Gaustadalleen 210349 Oslo, Postboks 702027 KJELLER

Abstract: In this paper, we report the microstructure and first hydrogenation properties of TiFe doped with 4 wt.% Zr additive using ball milling and cryomilling techniques. First, as-cast sample shows a TiFe main phase and Fe_2Ti-like ($MgZn_2$ type) secondary phase. Secondly, ball milling and cryomilling significantly reduced the particle and crystallite sizes but most of the reduction occurred during the first 15 minutes of milling. In addition the agglomeration of ball-milled samples increases with milling time. Thirdly, cryomilled sample didn't absorb any hydrogen. Ball milling can improve the initial kinetics compared with as-cast sample but the capacity was reduced. The increased kinetics is due to the reduction of crystallite size with ball milling time. And the loss of capacity may be due to the change of thermodynamics upon milling. Finally, the first hydrogenation kinetics of all samples (without cryomilled sample) agrees with GB3D model. The feature of this model is that 3D growth and the growth interface velocity of diffusion decreases with time.

Keywords: TiFe alloy; First hydrogenation kinetics; Kinetic model; Ball milling; Cryomilling

Effect of ball milling and cryomilling on the microstructure and first hydrogenation properties of TiFe + 4 wt.% Zr alloy

Peng Lv[1], Matylda N. Guzik[2], Sabrina Sarori[2], Jacques Huot[1*]

1. Hydrogen Research Institute, Université du Québec à Trois-Rivières, 3351 des Forges, Trois-Rivières, G9A 5H7, Canada

2. Department of Technology Systems, University of Oslo, P.O. Box 70, 2027 Kjeller, Norway

Email: Peng Lv (peng.lv@uqtr.ca), Matylda N. Guzik (m.n.guzik@its.uio.no), Sabrina Sarori (sabrina.sartori@its.uio.no), Jacques Huot (jacques.huot@uqtr.ca)

Abstract: In this paper, we report the microstructure and first hydrogenation properties of TiFe cast with 4 wt.% of Zr after processing by ball milling and cryomilling. It was found that ball milling and cryomilling significantly reduced the particle/crystallite sizes with most of the reduction occurring during the first 15 minutes of milling. While the cryomilled sample didn't absorb any hydrogen, ball milling improved the initial kinetics of processed powders compared with the as-cast sample. However it alsoreduced the hydrogen storage capacity. The observed increased kinetics was likely caused by the reduction of crystallite sizes with longer ball milling times. However, the longer ball milling times might also be the reason of the capacity loss due to formation of new grain boundaries. Faster kinetics was not due to a change in the rate-limiting step, as all kinetics curves were fitted with the 3D growth, diffusion controlled with decreasing interface velocity model.

Keywords: TiFe alloy; First hydrogenation kinetics; Rate limiting step; Ball milling; Cryomilling

1. Introduction

The TiFe alloy is a good material for solid state hydrogen storage due to its low plateau pressure at room temperature and relatively low price [1-7]. However, one of its disadvantages is rather slow first hydrogenation kinetics [8-11]. Reilly et al. reported that pure TiFe sample had to be exposed to high temperatures (around 400 °C) and high hydrogen pressures (6.5 MPa) before being able to absorb/desorb hydrogen at normal conditions [12]. Thus, one way to reduce the cost of this alloy is to make its first hydrogenation possible at room temperature and under low hydrogen pressure.

Doping is an effective way to improve the hydrogenation properties of the TiFe alloy. Kumar et al. found that the first hydrogenation of TiFe sample doped with 3.1 wt.% of vanadium occurred at 54°C. However the hydrogen storage capacity slightly decreased [13]. Later, Jain et al. showed that the first hydrogenation of the TiFe alloy was possible without any prior heat treatment just by adding zirconium [14]. Recently, Lv and Huot found that $Ti_{0.95}FeZr_{0.05}$, $TiFe_{0.95}Zr_{0.05}$ and $TiFeZr_{0.05}$ alloys showed totally different microstructures and the first hydrogenation properties. The first hydrogenation (also called activation) of these alloys were performed at room temperature and under 2 MPa of hydrogen gas [3].

Mechanical milling is also an effective method to improve the first hydrogenation properties of the TiFe alloy. It is well known that presence of defects and nanocrystallites could enhance the reaction kinetic and reduce incubation time. Moreover, it has been shown that mechanical milling is a fast and efficient way to reduce crystallite sizes and induce defects in materials [1, 7, 15, 16]. Chiang et al. investigated the hydrogenation properties of TiFe alloy processed under the reactive hydrogen atmosphere. They found that milled TiFe powder absorbed hydrogen without any prior heat treatment [17]. Emami et al. used ball milling technique to synthesize the nanocrystalline TiFe metallic compound. Their study showed clearly that ball milling reduced the particle sizes of obtained powders and facilitated the first hydrogenation reaction [1].

Recently, Gosselin et al. found that the first hydrogenation of the TiFe alloy doped with 4 wt.% of zirconium occurred at room temperature and under 4.5 MPa of hydrogen gas. However, the hydrogen absorption process was still too slow [18]. In order to improve the kinetic of the first hydrogenation, we tested the efficiency of ball milling and cryomilling on the TiFe alloy with addition of 4 wt.% of zirconium. The hypothesis was that ball milling or cryomilling will introduce defects that will help the hydrogenation kinetics. However, ball milling could also destroy/change the microstructure of this two phase alloy and may end up being detrimental.

2. Materials and methods

Fe (99.9%), Ti (99.9%) and Zr (99.5%) were purchased from Alfa Aesar and used without further purification. TiFe + 4 wt.% Zr was prepared by arc melting in argon atmosphere. All samples were synthesized by mixing the three elements with a proper ratio and melting them together. In order to improve the sample homogeneity, each pellet was turned over and re-melted three times. Ball milling was performed on as-cast alloys using hardened stainless-steel balls, with a ball to powder (BTP) weight ratio of 10:1. Loading of the crucible was done in an argon-filled glovebox. Ball milling was performed for 5, 15, 30 and 60 minutes (simplified samples notation: BM5, BM15, BM30 and BM60, respectively) with a SPEX 8000M apparatus at the milling velocity of 1060 rpm. Powders handling and milling were done in argon. Cryomilling (simplified sample notation: CM15) was performed in a hardened steel vial using a Retsch CryoMill at liquid nitrogen temperatures, with a BTP ratio of 20:1. The milling was carried out continuously for 15 minutes, at the impact frequency of 30 Hz (1800 rpm). For cryomilling, powders handling and milling were done in air.

The crystal structure was determined by powder X-ray diffraction (PXD) using a Bruker D8 Focus diffractometer (λ = Cu Kα). Lattice parameters were calculated by Rietveld refinements using the TOPAS software [19, 20]. Microstructural and chemical analysis of powders were carried on with a JEOL JSM-5500 scanning electron microscope (SEM) equipped with an energy dispersive X-ray spectrometer

(EDS). The hydrogen storage properties were measured using a home-made Sieverts-type apparatus.

3. Results and discussion

3.1. Morphology

Fig. 1 shows the SEM micrographs of the as-cast, ball milled and cryomilled samples of TiFe + 4 wt.% Zr alloy. The as-cast particles have sharp edges, resulting from the grinding procedure performed using a mortar and a pestle. After only 5 minutes of ball milling, the particles are much smaller and are characterised by round edges. Further milling resulted in agglomerations of smaller particles. Cryomilling produced a much finer powder without the agglomeration seen in the room temperature milling.

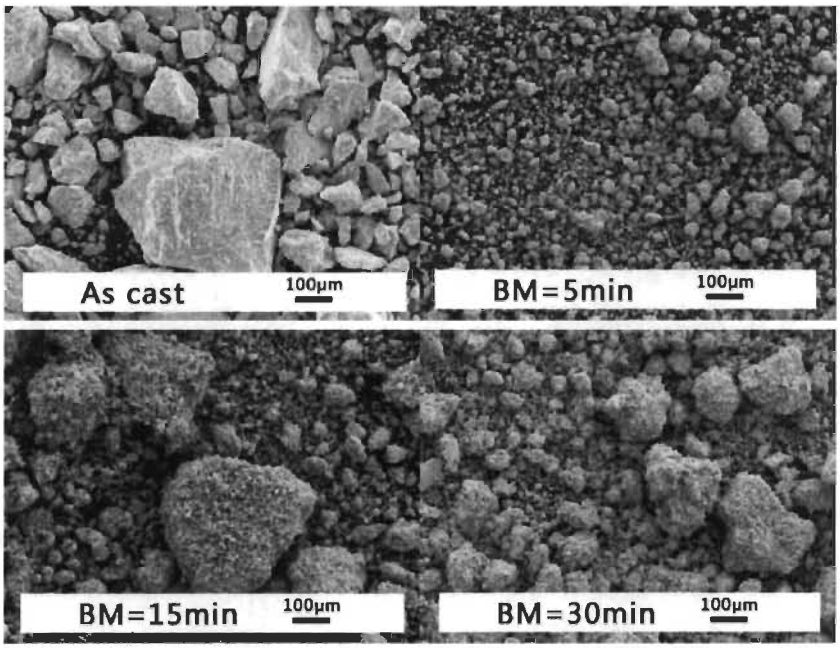

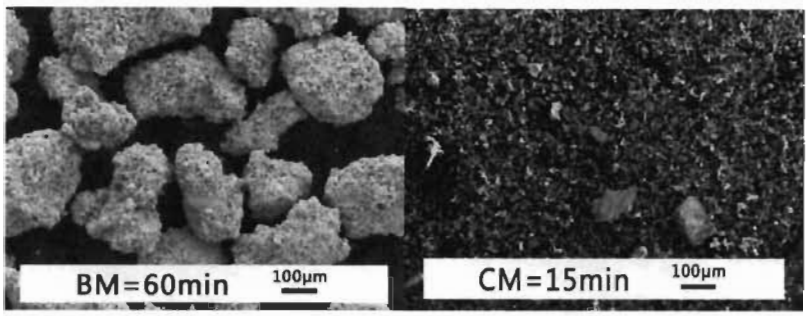

Fig. 1. SEM micrographs of TiFe + 4 wt.% Zr alloy in the as-cast, cryomilled (CM) and ball milled (BM5, BM15, BM30 and BM60 min) states.

3.2. Phase analysis and microstructure

The PXD patterns for ball milled and cryomilled samples of the TiFe + 4 wt.% Zr alloy are presented in Fig. 2. It can be clearly seen that the TiFe Bragg peaks of the ball milled powders are getting broader with longer milling times. This is an indication of the crystallite size reduction due to mechanical processing of the materials. The low-intensity peaks at around 38~46° 2θ in the diffraction pattern of the as-cast sample are due to the secondary phase (Fe_2Ti with $MgZn_2$-type structure) [21]. They are no longer observed in the PXD data of the ball milled samples because the peaks broadening due to reduction of crystallite size makes them indistinguishable from the background.

Table 1 shows the calculated lattice parameters and crystallite sizes for all samples. The lattice parameter seems to have an erratic behavior but it should be mentioned that the literature value of the lattice parameter of TiFe varies from a lower boundary of 2.953(2) Å [22] to a upper boundary of 2.9802(2) Å [23]. In the present case, the lattice parameter is actually higher than the high boundary literature value but is agrees with the value recently published on for TiFe+4 wt.% Zr alloys [24]. The observed minor expansion of the unit cell can be explained by the presence of a small amount of Zr in solid solution in the TiFe lattice. Table 1 indicates that the crystallite size is reduced with prolonged milling. Results also show that 15 minutes of cryomilling leads to formation of bigger crystallites than milling for the same time at room temperature. This can be explained by the fact that the milling conditions

(milling atmosphere, milling speed, BTP ratio, balls sizes, etc) were totally different in both experiments.

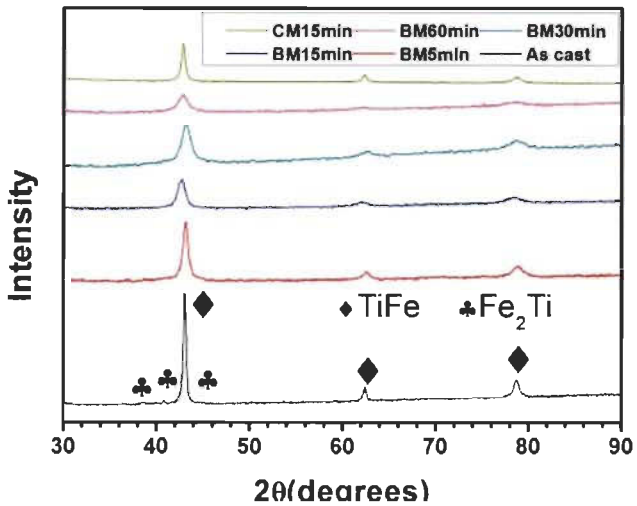

Fig. 2. Powder diffraction patterns of TiFe + 4 wt.% Zr alloy in the as-cast. cyromilled (CM) and ball milled (BM) states.

Table 1–Lattice parameter *a* (in Å) and crystallite size (nm) of TiFe phase of TiFe+4 wt.% Zr alloy in different state as determined by Rietveld analysis. The number in parenthesis is the error on the last significant digit.

	As-cast	BM5min	BM15min	BM30min	BM60min	CM15min
a	2.9816(3)	2.9828(7)	2.992(1)	2.976(2)	2.992(2)	2.9772(5)
Crystallite size	23.2(3)	10.4(3)	8.4(3)	5.6(2)	4.8(2)	14.9(4)

3.3. First hydrogenation

Fig. 3 shows the first hydrogenation process at room temperature and under 4.5 MPa of hydrogen. The as-cast alloy absorbed 1.6 wt.% of H_2 in 2.5 hours. Ball milling slightly improved the hydrogenation kinetics of the reaction but the capacity decreased with milling times. Even more drastic effect is seen for the cryomilled sample that didn't absorb any hydrogen. This may be explained by the fact that the experiment was carried out in air and resulted in the formation of oxide(s) layer on

146 the surface of particles. Due to that, crymilling as short as15 minutes, made the alloy
147 totally inert toward hydrogen.
148

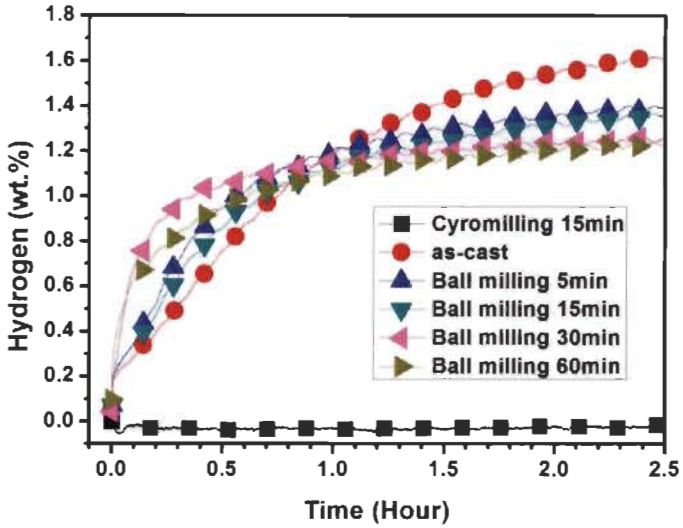

149

150 Fig. 3. First hydrogenation at room temperature and under 4.5 MPa hydrogen of the
151 TiFe + 4 wt.% Zr alloy at different states.
152

153 Why samples with longer ball milling times show faster kinetics but lower hydrogen
154 storage capacity should also be explained. In Fig. 1 and Table 1 it can be seen that
155 longer milling time at room temperature effectively reduce the crystallite/particle
156 sizes. This leads to a faster diffusion of hydrogen along the particle surfaces and the
157 newly formed grain boundaries. In addition, the latter are favourable nucleation sites
158 for the formation of the hydride phase [25]. This may explain the initial fast
159 absorption kinetics of the ball-milled samples.
160 Table 2 presents the total hydrogen capacity (wt.%) of powders hydrogenated for 5
161 hours, and the capacity retention (%) for all samples. The capacity retention is
162 defined as the measured capacity over the theoretical capacity of TiFe (1.86 wt.%). It
163 is easy to see that the capacity retention decreases with increasing ball milling times.
164 In their investigation of ball milled magnesium hydride, Hanada et al explained that
165 the decreased crystallite size associated with increasing grain boundary and lattice
166 strains can lead to the decrease in hydrogen storage capacity [26]. This phenomenon

appears to be also present in our sample. Figure 4 shows the dependence of the total hydrogen capacity and the crystallite size on the ball milling time for the TiFe + 4 wt.% Zr alloy. As can be seen, with the longer milling times the crystallite size and the total hydrogen capacity decrease in the same fashion.

Table 2–Total hydrogen capacity (wt.%) after 5 hours of hydrogenation and capacity retention S_n (%) for the as-cast and mechanochemically processed TiFe + 4 wt.% Zr alloys.

	As-cast	BM5min	BM15min	BM30min	BM60min
Total hydrogen capacity	1.64	1.55	1.51	1.31	1.29
Capacity retention (S_n)	88	83	81	70	69

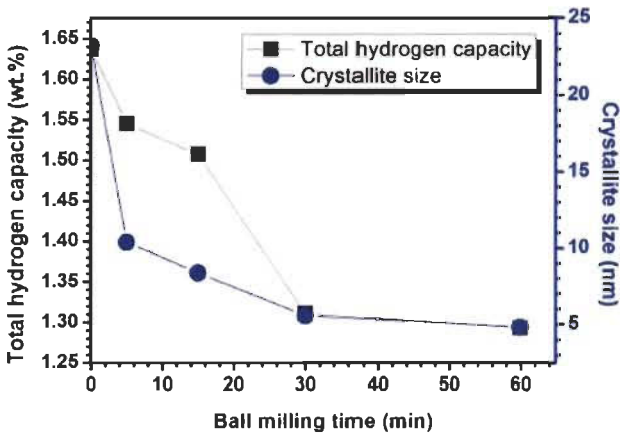

Fig. 4. Total hydrogen capacity and crystallite size vs. milling time for ball milled TiFe + 4 wt.% Zr alloy.

3.4. Rate limiting step models of first hydrogenation

The first hydrogenation curves were analyzed by comparison with different rate limiting step models shown in Table 3. For all models, the left side of the equations is a function of the reaction's completion ratio, where α is the reaction's completion rate

185 (α=%H_{abs}/%H_{max}), t is reaction time, and k is kinetic rate constant. In order to find the
186 correct rate limiting step, the left side of these equations was plotted as a function of
187 time. From this type of plot, the correct rate limiting step is a linear curve.
188
189 Table 3. Rate limiting step model equations [27, 28].
190

Model name	Model equation where α is %H_{abs}/%H_{max}	Model description
Chemisorption	α=kt	Surface controlled
JMA2D	$[-\ln(1-\alpha)]^{1/2}$=kt	2D growth of existing nuclei with constant interface velocity
JMA3D	$[-\ln(1-\alpha)]^{1/3}$=kt	3D growth of existing nuclei with constant interface velocity
CV2D	$1-(1-\alpha)^{1/2}$=kt	2D growth of with constant interface velocity
CV3D	$1-(1-\alpha)^{1/3}$=kt	3D growth of with constant interface velocity
GB2D	$(1-\alpha)\ln(1-\alpha)+\alpha$=kt	2D growth, diffusion controlled with decreasing interface velocity
GB3D	$1-(2\alpha/3)-(1-\alpha)^{2/3}$=kt	3D growth, diffusion controlled with decreasing interface velocity

191
192 As a representative, Fig. 5 shows the plot of the first hydrogenation kinetic for the
193 alloy milled 5 minutes (BM5). Linear regressions were performed on each model. As

194 indicated in the literature, the regressions are made in a range from 10% to 90% of
195 the reaction's completion (α = 0.1~0.9 [27]). It can be clearly seen that GB3D shows
196 a good fit. In addition, Table 4 shows the adjusted R^2 values for all rate limiting step
197 model equations. For GB3D this value is 0.946 and indicates a very linear curve. This
198 means that the GB3D model describes the best rate limiting step for the sample
199 milled for 5 minutes. From the description given in Table 3, the GB3D model
200 assumes the 3D growth and the growth interface velocity of diffusion decreases with
201 time [29]. Similar plots were made for the first hydrogenation curves of all samples.
202 The results indicate that the activation kinetics agree with the GB3D model for all of
203 them.
204

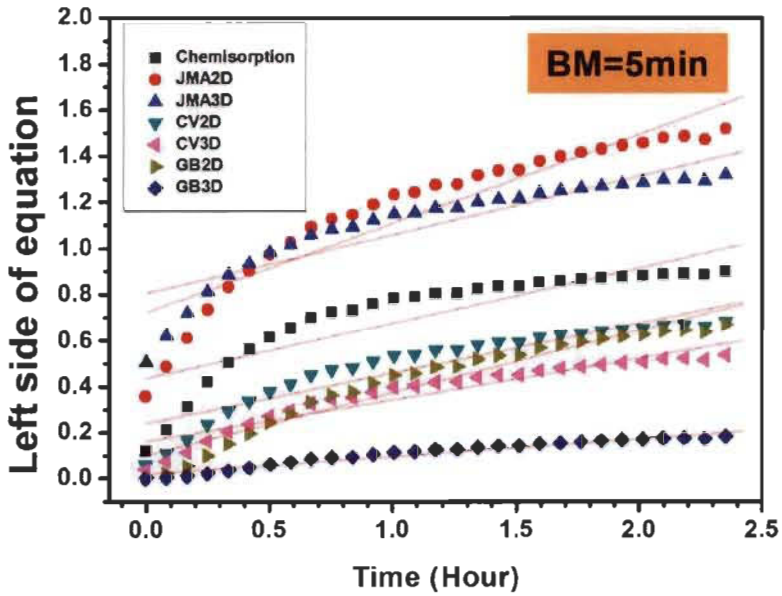

205
206 Fig. 5. Rate limiting step curves of first hydrogenation for the BM5 sample.
207
208
209
210
211
212
213
214
215
216

217 Table 4. Adjusted R^2 values for all model equations for the BM5 sample.
218

Sample	Model	R^2
BM=5 min	Chemisorption	0.759
	JMA2D	0.866
	JMA3D	0.829
	CV2D	0.862
	CV3D	0.893
	GB2D	0.925
	GB3D	0.946

219
220

221 **4. Conclusion**

222 Hydrogenation properties of mechanochemically processed TiFe with addition of 4
223 wt.% of Zr has been investigated. The as-cast sample shows TiFe as a main phase and
224 traces of Fe_2Ti-like phase. Results of the first hydrogenation on samples that were
225 processed by ball milling and cryomilling lead to the following conclusions:
226 (1) Ball milling and cryomilling significantly reduce the particle/crystallite sizes with
227 most of the reduction occurring during the first 15 minutes of milling. In addition,ball
228 milling produced particle agglomeration which increases with milling times.
229 (2) High energy milling at room temperature improves the initial hydrogenation
230 kinetics of processed powders as compared with the as-cast sample but reduces the
231 H-storage capacity. The faster kinetics is due to the reduction of the crystallite sizes
232 and formation of new grain boundaries. The reduced hydrogen storage capacity may
233 be explained by the formation of grain boundaries that enhance the hydrogen
234 diffusion but do not store hydrogen in their structures.
235 (3) Cryomilled sample does not absorb any hydrogen. This is probably due to the
236 formation of the oxide layer(s) on particles surface, as experiment were carried in air.
237 (4) The first hydrogenation kinetics for all samples agrees well with the GB3D model.
238 The feature of this model is that the 3D growth and the growth interface velocity of
239 diffusion decrease with time.
240

Acknowledgements

Peng Lv is thankful to Fonds de recherche du Quebec-Nature et technologies (FRQNT) for a PBEEE fellowship. We would also thank Mrs. A. Lejeune for SEM analysis and Dr. Jingjing Liu and Dr. Abhishek Patel for helpful discussion.

References

[1] H. Emami, K. Edalati, J. Matsuda, E. Akiba, Z. Horita, Hydrogen storage performance of TiFe after processing by ball milling, Acta Materialia, 88 (2015) 190-195.

[2] S. Lanyin, L. Fangjie, B. Deyou, An advanced TiFe series hydrogen storage material with high hydrogen capacity and easily activated properties, International journal of hydrogen energy, 15 (1990) 259-262.

[3] P. Lv, J. Huot, Hydrogen storage properties of Ti 0.95 FeZr 0.05, TiFe 0.95 Zr 0.05 and TiFeZr 0.05 alloys, International Journal of Hydrogen Energy, 41 (2016) 22128-22133.

[4] P. Lv, J. Huot, Hydrogenation improvement of TiFe by adding ZrMn2, Energy, 138 (2017) 375-382.

[5] L.E.R. Vega, D.R. Leiva, R.M. Leal Neto, W.B. Silva, R.A. Silva, T.T. Ishikawa, C.S. Kiminami, W.J. Botta, Mechanical activation of TiFe for hydrogen storage by cold rolling under inert atmosphere, International Journal of Hydrogen Energy, 43 (2018) 2913-2918.

[6] J. Yin, Q. Li, H. Leng, Advances in Improvement of Hydrogen Storage Properties of TiFe-based Alloys, Materials Review, 24 (2016) 141-147.

[7] V. Zadorozhnyy, S. Klyamkin, M. Zadorozhnyy, O. Bermesheva, S. Kaloshkin, Hydrogen storage nanocrystalline TiFe intermetallic compound: Synthesis by mechanical alloying and compacting, International Journal of Hydrogen Energy, 37 (2012) 17131-17136.

[8] T. Schober, D. Westlake, The activation of FeTi for hydrogen storage: a different view, Scripta Metallurgica, 15 (1981) 913-918.

[9] D. Khatamian, G. Weatherly, F. Manchester, Some effects of activation for hydrogen absorption in FeTi powder, Acta Metallurgica, 31 (1983) 1771-1780.

[10] K. Edalati, J. Matsuda, A. Yanagida, E. Akiba, Z. Horita, Activation of TiFe for hydrogen storage by plastic deformation using groove rolling and high-pressure torsion: Similarities and differences, international journal of hydrogen energy, 39 (2014) 15589-15594.

[11] K. Edalati, J. Matsuda, H. Iwaoka, S. Toh, E. Akiba, Z. Horita, High-pressure torsion of TiFe intermetallics for activation of hydrogen storage at room temperature with heterogeneous nanostructure, International Journal of Hydrogen Energy, 38 (2013) 4622-4627.

[12] J. Reilly, R. Wiswall Jr, Formation and properties of iron titanium hydride, Inorganic Chemistry, 13 (1974) 218-222.

[13] S. Kumar, G. Tiwari, S. Sonak, U. Jain, N. Krishnamurthy, High performance FeTi–3.1 mass% V alloy for on board hydrogen storage solution, Energy, 75 (2014) 520-524.

[14] P. Jain, C. Gosselin, J. Huot, Effect of Zr, Ni and Zr 7 Ni 10 alloy on hydrogen storage characteristics of TiFe alloy, International Journal of Hydrogen Energy, 40 (2015) 16921-16927.

[15] M. Abe, T. Kuji, Hydrogen absorption of TiFe alloy synthesized by ball milling and post-annealing, Journal of Alloys and Compounds, 446-447 (2007) 200-203.

[16] V.Y. Zadorozhnyy, G.S. Milovzorov, S.N. Klyamkin, M.Y. Zadorozhnyy, D.V. Strugova, M.V. Gorshenkov, S.D. Kaloshkin, Preparation and hydrogen storage properties of nanocrystalline TiFe synthesized by mechanical alloying, Progress in Natural Science: Materials International, 27 (2017) 149-155.

[17] C.-H. Chiang, Z.-H. Chin, T.-P. Perng, Hydrogenation of TiFe by high-energy ball milling, Journal of alloys and compounds, 307 (2000) 259-265.

[18] C. Gosselin, J. Huot, Hydrogenation Properties of TiFe Doped with Zirconium, Materials, 8 (2015) 7864-7872.

298 [19] A.A. Coelho, Topas-Academic, A Computer Programme for Rietveld Analysis,
299 (2004).
300 [20] A. Bruker, TOPAS V3: General profile and structure analysis software for
301 powder diffraction data, User's Manual, Bruker AXS, Karlsruhe, Germany, (2005).
302 [21] S.M. Lee, T.P. Perng, Effects of boron and carbon on the hydrogenation
303 properties of TiFe and Ti1.1Fe, International Journal of Hydrogen Energy, 25 (2000)
304 831-836.
305 [22] O. Toma, M. Dzevenko, A. Oliynyk, Y. Lomnytska, The Ti-Fe-P system: phase
306 equilibria and crystal structure of phases, Open Chemistry, 11 (2013) 1518-1526.
307 [23] L. Romaka, V. Romaka, Y. Stadnyk, N. Melnychenko, On the formation of
308 ternary phases in the Ti–Fe–Sn ternary system at 773 K, Chemistry of metals and
309 alloys, (2013) 12-19.
310 [24] A.K. Patel, P. Sharma, J. Huot, Effect of annealing on microstructure and
311 hydrogenation properties of TiFe+ X wt% Zr (X= 4, 8), International Journal of
312 Hydrogen Energy, 43 (2018) 6238-6243.
313 [25] J. Gubicza, 8 - Relationship between microstructure and hydrogen storage
314 properties of nanomaterials, in: Defect Structure in Nanomaterials, Woodhead
315 Publishing, 2012, pp. 301-332.
316 [26] N. Hanada, T. Ichikawa, S.-I. Orimo, H. Fujii, Correlation between hydrogen
317 storage properties and structural characteristics in mechanically milled magnesium
318 hydride MgH2, Journal of Alloys and Compounds, 366 (2004) 269-273.
319 [27] J. Lang, M. Eagles, M.S. Conradi, J. Huot, Hydrogenation rate limiting step,
320 diffusion and thermal conductivity in cold rolled magnesium hydride, Journal of
321 Alloys and Compounds, 583 (2014) 116-120.
322 [28] Y. Pang, Q. Li, A review on kinetic models and corresponding analysis methods
323 for hydrogen storage materials, International Journal of Hydrogen Energy, 41 (2016)
324 18072-18087.

325 [29] G. Barkhordarian, T. Klassen, R. Bormann, Kinetic investigation of the effect of
326 milling time on the hydrogen sorption reaction of magnesium catalyzed with different
327 Nb 2 O 5 contents, Journal of Alloys and Compounds, 407 (2006) 249-255.
328

REFERENCES

[1] https://en.wikipedia.org/wiki/Hydrogen_fuel#Energy.

[2] Rinkesh. https://www.conserve-energy-future.com/advantages_disadvantages_hydrogenenergy.php.

[3] Winter CJ. Hydrogen energy — Abundant, efficient, clean: A debate over the energy-system-of-change. International Journal of Hydrogen Energy. 2009;34:S1-S52.

[4] https://frontierenergy.com/overview/.

[5] U.S. Department of Energy's Office of Energy Efficiency and Renewable Energy. https://www.energy.gov/eere/fuelcells/hydrogen-storage.

[6] Niaz S, Manzoor T, Pandith AH. Hydrogen storage: Materials, methods and perspectives. Renewable and Sustainable Energy Reviews. 2015;50:457-69.

[7] Srinivasan SS, Demirocak DE. Metal Hydrides used for Hydrogen Storage. In: Chen YP, Bashir S, Liu JL, editors. Nanostructured Materials for Next-Generation Energy Storage and Conversion: Hydrogen Production, Storage, and Utilization. Berlin, Heidelberg: Springer Berlin Heidelberg; 2017. p. 225-55.

[8] Reilly Jr JJ, Wiswall Jr RH. Reaction of hydrogen with alloys of magnesium and nickel and the formation of Mg2NiH4. Inorganic chemistry. 1968;7:2254-6.

[9] Zaluska A, Zaluski L, Ström-Olsen J. Synergy of hydrogen sorption in ball-milled hydrides of Mg and Mg 2 Ni. Journal of Alloys and Compounds. 1999;289:197-206.

[10] Zaluski L, Zaluska A, Ström-Olsen J. Hydrogen absorption in nanocrystalline Mg2Ni formed by mechanical alloying. Journal of Alloys and Compounds. 1995;217:245-9.

[11] Reilly J, Wiswall Jr R. Formation and properties of iron titanium hydride. Inorganic Chemistry. 1974;13:218-22.

[12] Reilly J, Wiswall Jr R. Iron titanium manganase alloy hydrogen storage. 1975.

[13] Bloch J, Mintz MH. Kinetics and mechanisms of metal hydrides formation—a review. Journal of Alloys and Compounds. 1997;253:529-41.

[14] Chou KC, Xu K. A new model for hydriding and dehydriding reactions in intermetallics. Intermetallics. 2007;15:767-77.

[15] Schweppe F, Martin M, Fromm E. Model on hydride formation describing surface control, diffusion control and transition regions. Journal of alloys and compounds. 1997;261:254-8.

[16] Avrami M. Kinetics of phase change. I General theory. The Journal of Chemical Physics. 1939;7:1103-12.

[17] Avrami M. Kinetics of phase change. II transformation - time relations for random distribution of nuclei. The Journal of Chemical Physics. 1940;8:212-24.

[18] Avrami M. Granulation, phase change, and microstructure kinetics of phase change. III. The Journal of chemical physics. 1941;9:177-84.

[19] Carstensen J. Stability of solids and solid dosage forms. Journal of pharmaceutical sciences. 1974;63:1-14.

[20] Koga N, Criado J. Influence of the particle size distribution on the CRTA curves for the solid-state reactions of interface shrinkage type. Journal of thermal analysis. 1997;49:1477-84.

[21] Koga N, Criado JM. Kinetic Analyses of Solid - State Reactions with a Particle - Size Distribution. Journal of the American Ceramic Society. 1998;81:2901-9.

[22] Crank J. The mathematics of diffusion: Oxford university press; 1979.

[23] Ginstling A, Brounshtein B. Concerning the diffusion kinetics of reactions in spherical particles. J Appl Chem USSR. 1950;23:1327-38.

[24] Lang J, Eagles M, Conradi MS, Huot J. Hydrogenation rate limiting step, diffusion and thermal conductivity in cold rolled magnesium hydride. Journal of Alloys and Compounds. 2014;583:116-20.

[25] Pang Y, Li Q. A review on kinetic models and corresponding analysis methods for hydrogen storage materials. International Journal of Hydrogen Energy. 2016;41:18072-87.

[26] Fang S, Zhou Z, Zhang J, Yao M, Feng F, Northwood DO. The application of mathematical models to the calculation of selected hydrogen storage properties (formation enthalpy and hysteresis) of AB2-type alloys. International Journal of Hydrogen Energy. 2000;25:143-9.

[27] Züttel A. Materials for hydrogen storage. Materials today. 2003;6:24-33.

[28] Züttel A. Hydrogen storage methods. Naturwissenschaften. 2004;91:157-72.

[29] Majzoub EH, Rönnebro ECE. Methodology of materials discovery in complex metal hydrides using experimental and computational tools. Materials Science and Engineering: R: Reports. 2012;73:15-26.

[30] Shenzhong Y, Rong Y, Tiesheng H, Shilong Z, Bingzhao C. A study of the activation of FeTi and Fe0.9 TiMn0.1. International Journal of Hydrogen Energy. 1988;13:433-7.

[31] Schober T, Westlake D. The activation of FeTi for hydrogen storage: a different view. Scripta Metallurgica. 1981;15:913-8.

[32] Khatamian D, Weatherly G, Manchester F. Some effects of activation for hydrogen absorption in FeTi powder. Acta Metallurgica. 1983;31:1771-80.

[33] Mitrokhin S, Verbetsky V, Kajumov R, Cunmao H, Yufen Z. Hydrogen sorption peculiarities in FeTi-type Ti-Fe-V-Mn alloys. Journal of alloys and compounds. 1993;199:155-60.

[34] Leng H, Yu Z, Yin J, Li Q, Wu Z, Chou K-C. Effects of Ce on the hydrogen storage properties of TiFe0.9Mn0.1 alloy. International Journal of Hydrogen Energy. 2017.

[35] Lee SM, Perng TP. Effect of the second phase on the initiation of hydrogenation of TiFe1− xMx (M= Cr, Mn) alloys. International journal of hydrogen energy. 1994;19:259-63.

[36] Lee SM, Perng TP, Juang HK, Chen SY, Chen WY, Hsu SE. Microstructures and hydrogenation properties of TiFel−xMχ alloys. Journal of Alloys and Compounds. 1992;187:49-57.

[37] Kumar S, Tiwari GP, Sonak S, Jain U, Krishnamurthy N. High performance FeTi – 3.1 mass % V alloy for on board hydrogen storage solution. Energy. 2014;75:520-4.

[38] Lv P, Wang Z, Zhou H, Deng J, Yao Q, Zhang H. Effect of Co substitution for La on hydrogen storage properties and thermal stabilities of amorphous Mg60Ni30La10− xCox (x= 0, 2 and 4) alloys prepared by melt spinning. Materials Science and Technology. 2014;30:176-82.

[39] Abe M, Kuji T. Hydrogen absorption of TiFe alloy synthesized by ball milling and post-annealing. Journal of Alloys and Compounds. 2007;446-447:200-3.

[40] Emami H, Edalati K, Matsuda J, Akiba E, Horita Z. Hydrogen storage performance of TiFe after processing by ball milling. Acta Materialia. 2015;88:190-5.

[41] Zadorozhnyy V, Klyamkin S, Zadorozhnyy M, Bermesheva O, Kaloshkin S. Hydrogen storage nanocrystalline TiFe intermetallic compound: Synthesis by mechanical alloying and compacting. International Journal of Hydrogen Energy. 2012;37:17131-6.

[42] Zadorozhnyy VY, Klyamkin SN, Yu. Zadorozhnyy M, Gorshenkov MV, Kaloshkin SD. Mechanical alloying of nanocrystalline intermetallic compound TiFe doped with sulfur and magnesium. Journal of Alloys and Compounds. 2014;615:S569-S72.

[43] Zadorozhnyy VY, Klyamkin SN, Zadorozhnyy MY, Bermesheva OV, Kaloshkin SD. Mechanical alloying of nanocrystalline intermetallic compound TiFe doped by aluminum and chromium. Journal of Alloys and Compounds. 2014;586:S56-S60.

[44] Zadorozhnyy VY, Milovzorov GS, Klyamkin SN, Zadorozhnyy MY, Strugova DV, Gorshenkov MV, et al. Preparation and hydrogen storage properties of nanocrystalline TiFe synthesized by mechanical alloying. Progress in Natural Science: Materials International. 2017;27:149-55.

[45] Tousignant M, Huot J. Hydrogen sorption enhancement in cold rolled LaNi 5. Journal of Alloys and Compounds. 2014;595:22-7.

[46] Edalati K, Matsuda J, Yanagida A, Akiba E, Horita Z. Activation of TiFe for hydrogen storage by plastic deformation using groove rolling and high-pressure torsion: Similarities and differences. international journal of hydrogen energy. 2014;39:15589-94.

[47] Edalati K, Matsuda J, Iwaoka H, Toh S, Akiba E, Horita Z. High-pressure torsion of TiFe intermetallics for activation of hydrogen storage at room temperature with heterogeneous nanostructure. International Journal of Hydrogen Energy. 2013;38:4622-7.

[48] Nishimiya N, Wada T, Matsumoto A, Tsutsumi K. Hydriding characteristics of zirconium-substituted FeTi. Journal of alloys and compounds. 2000;313:53-8.

[49] Jain P, Gosselin C, Huot J. Effect of Zr, Ni and Zr 7 Ni 10 alloy on hydrogen storage characteristics of TiFe alloy. International Journal of Hydrogen Energy. 2015;40:16921-7.

[50] Emami H, Edalati K, Matsuda J, Akiba E, Horita Z. Hydrogen storage performance of TiFe after processing by ball milling. Acta Materialia. 2015;88:190-5.

[51] W. Cao.
http://www.understandingnano.com/nanomaterial-synthesis-ball-milling.html.

[52] Huot J. Nanocrystalline metal hydrides obtained by severe plastic deformations. Metals. 2012;2:22-40.

[53] Coelho AA. Topas-Academic. A Computer Programme for Rietveld Analysis. 2004.

[54] Bruker A. TOPAS V3: General profile and structure analysis software for powder diffraction data. User's Manual, Bruker AXS, Karlsruhe, Germany. 2005.

[55] Toby BH. EXPGUI, a graphical user interface for GSAS. Journal of applied crystallography. 2001;34:210-3.

[56] Larson AC, Von Dreele RB. GSAS: generalized structure analysis system. Document LAUR. 1994:86-748.

[57] Larson A, Von Dreele R. GSAS General Structure Analysis System, Report LAUR 86-748. Los Alamos National Laboratory, Los Alamos, NM. 1986.

[58] Collins T. ImageJ for Microscopy. BioTechniques, 43. S25-S30 http://dx doi org/102144/000112517. 2007.

[59] Abràmoff MD, Magalhães PJ, Ram SJ. Image processing with ImageJ. Biophotonics international. 2004;11:36-42.

[60] Broom DP. Hydrogen storage materials: the characterisation of their storage properties: Springer Science & Business Media; 2011.

[61] Dutrow BL, Clark CM.

https://serc.carleton.edu/research_education/geochemsheets/techniques/XRD.html.

[62]

https://www.sheffield.ac.uk/materials/centresandfacilities/x-ray-diffraction/whatxrd.

[63] IIT GUWAHATI. http://nptel.ac.in/courses/115103030/3. 2016.

[64] https://commons.wikimedia.org/wiki/File:Bragg_diffraction.png.

[65] https://en.wikipedia.org/wiki/Synchrotron.

[66] Online Digital Education Connection.

http://www.odec.ca/projects/2005/shar5a0/public_html/how_does_a_synchrotron_work.htm.

[67] https://en.wikipedia.org/wiki/Scanning_electron_microscope.

[68] Swapp S.

https://serc.carleton.edu/research_education/geochemsheets/techniques/SEM.html.

[69] Australian Microscopy & Microanalysis Research Facility.

http://www.ammrf.org.au/myscope/sem/practice/principles/layout.php#term.

[70] Gosselin C, Huot J. Hydrogenation Properties of TiFe Doped with Zirconium. Materials. 2015;8:7864-72.

[71] Lv P, Huot J. Hydrogen storage properties of Ti 0.95 FeZr 0.05, TiFe 0.95 Zr 0.05 and TiFeZr 0.05 alloys. International Journal of Hydrogen Energy. 2016;41:22128-33.

[72] Miller H, Murray J, Laury E, Reinhardt J, Goudy A. The hydriding and dehydriding kinetics of FeTi and Fe0. 9TiMn0. 1. Journal of alloys and compounds. 1995;231:670-4.

[73] Guéguen A, Latroche M. Influence of the addition of vanadium on the hydrogenation properties of the compounds TiFe0.9Vx and TiFe0.8Mn0.1Vx (x=0, 0.05 and 0.1). Journal of Alloys and Compounds. 2011;509:5562-6.

[74] Lee SM, Perng TP. Effects of boron and carbon on the hydrogenation properties of TiFe and Ti1.1Fe. International Journal of Hydrogen Energy. 2000;25:831-6.

[75] Raghavan V. Fe-Ti-Zr (Iron-Titanium-Zirconium). Journal of phase equilibria and diffusion. 2009;30:109-.

[76] Gosselin C, Santos D, Huot J. First hydrogenation enhancement in TiFe alloys for hydrogen storage. Journal of Physics D: Applied Physics. 2017;50:375303.

[77] Barkhordarian G, Klassen T, Bormann R. Kinetic investigation of the effect of milling time on the hydrogen sorption reaction of magnesium catalyzed with different Nb 2 O 5 contents. Journal of Alloys and Compounds. 2006;407:249-55.

[78] Endo N, Saitoh H, Machida A, Katayama Y. Formation of BCC TiFe hydride under high hydrogen pressure. International Journal of Hydrogen Energy. 2013;38:6726-9.

[79] Kinaci A, Aydinol M. Ab initio investigation of FeTi–H system. International journal of hydrogen energy. 2007;32:2466-74.

[80] Reidinger F, Lynch JF, Reilly J. An X-ray diffraction examination of the FeTi-H2 system. Journal of Physics F: Metal Physics. 1982;12:L49.

[81] Schefer J, Fischer P, Hälg W, Stucki F, Schlapbach L, Andresen A. Structural phase transitions of FeTi-deuterides. Materials Research Bulletin. 1979;14:1281-94.

[82] Toma O, Dzevenko M, Oliynyk A, Lomnytska Y. The Ti-Fe-P system: phase equilibria and crystal structure of phases. Open Chemistry. 2013;11:1518-26.

[83] Romaka L, Romaka V, Stadnyk Y, Melnychenko N. On the formation of ternary phases in the Ti–Fe–Sn ternary system at 773 K. Chemistry of metals and alloys. 2013:12-9.

[84] Patel AK, Sharma P, Huot J. Effect of annealing on microstructure and hydrogenation properties of TiFe+ X wt% Zr (X= 4, 8). International Journal of Hydrogen Energy. 2018;43:6238-43.

[85] Gubicza J. 8 - Relationship between microstructure and hydrogen storage properties of nanomaterials. Defect Structure in Nanomaterials: Woodhead Publishing; 2012. p. 301-32.

[86] Hanada N, Ichikawa T, Orimo S-I, Fujii H. Correlation between hydrogen storage properties and structural characteristics in mechanically milled magnesium hydride MgH2. Journal of Alloys and Compounds. 2004;366:269-73.

[87] Romero G, Lv P, Huot J. Effect of ball milling on the first hydrogenation of TiFe alloy doped with 4 wt% (Zr + 2Mn) additive. Journal of Materials Science. 2018.

[88] Lin HJ, Ouyang LZ, Wang H, Liu JW, Zhu M. Phase transition and hydrogen storage properties of melt-spun Mg3LaNi0.1 alloy. International Journal of Hydrogen Energy. 2012;37:1145-50.

[89] Ley MB, Jepsen LH, Lee YS, Cho YW, Von Colbe JMB, Dornheim M, et al. Complex hydrides for hydrogen storage–new perspectives. Materials Today. 2014;17:122-8.